Realization of a Humanoid Robot based on Muscular Skeletal Structure and Reflex-based Control

ARNE HITZMANN

SEPTEMBER 2021

Realization of a Humanoid Robot based on Muscular Skeletal Structure and Reflex-based Control

A dissertation submitted to
THE GRADUATE SCHOOL OF ENGINEERING SCIENCE
OSAKA UNIVERSITY
in partial fulfillment of the requirements for the degree of
DOCTOR OF PHILOSOPHY IN ENGINEERING

BY
ARNE HITZMANN
SEPTEMBER 2021

Abstract

Understanding humanoid manipulation attracted scientists as well as engineers for centuries. Scientists identify the importance of low-level local control for the system to achieve more complex tasks like manipulation. However, the specific mechanisms and their traversal from unconscious to conscious behavior are still in active research for humanoid manipulation. Current technology, however, does not allow to probe into a body's peripheral nerves to gather ground truth data. Robotic experiments and, to a limited degree, simulation allowed researchers to understand the underlying principles governing and scaffolding the higher competencies in biological entities. In this thesis, we started with the development of a complex manipulator based on the human upper body. This platform was then used to experiment with different approaches which aimed to create complex motor skills. The development and initial results using learning-based approaches to create motor skills then lead us to investigate and develop components representing the lowest control layer in a musculoskeletal system. This work will introduce these initial efforts to create an experimentation platform, leading to the development of bio-inspired sensors augmenting each pneumatic artificial muscle. We will discuss two different iterations of such sensors and their characteristics. We will then investigate the particular behavior of antagonistic muscle pairs. Based on our preliminary work, we will show via an experiment that feedback available in biological systems is sufficient to create low complexity control schemes. Properties like compliance can emerge via the trivial forwarding of feedback into functional blocks. The results presented in this work should be considered as an interface of theoretical models, including simulations and the real-world deployment of such strategies to improve humanoid manipulation, as well as understand the underlying principles that allow adaptable behavior to emerge from the system rather than specific controllers.

Tabel of Contents

Chapter 1

Introduction

Biological muscle control allows humans to learn highly flexible and adaptive motor skills [11]. In automation, researchers and engineers were highly successful in creating machines that can be used to fulfill complex tasks with high precision. However, these systems were first designed to operate in a highly controlled production environment, unaware of changes around them and unable to cope with other situations as they were programmed for [52]. Therefore, humans were not able to cooperate with them. For the purpose of automized production, these limitations were easily accepted and externally accounted for by placing the robots in zones human workers are not allowed to enter while the robots are working. In the recent past, the technology evolved to the degree that automation also reaches the fields where robots have to cooperate with their human coworkers or move from their well-controlled production lines into the uncertain environment of people's homes in the form of mobile systems that can fulfill several different tasks. Using the same techniques as they were used in the highly controlled setting in manufacturing, however, requires great control efforts so that these precise machines can interact with the everchanging world outside of the factories' production lines. Through the inspiration from nature, researchers realized that an alternative way of approaching the world's uncertainties is to create structures that can mitigate those imprecisions through their non-rigid morphology [34]. This field of soft robotics is gathering more traction recently as more tasks are identified that can be solved with a much lower control effort as it would have been possible using conventional rigid robots. Another aspect of soft robotics is the focus on the compliance of systems and how this can be utilized for coping with the world's uncertainties. Besides creating compliance through complex control with conventional robots, another approach actively researched is the use of replications of biological muscles and the usage of those to actuate structures that are inspired by morphologies found in nature. These systems can become highly complex but required less complicated control schemas to achieve compliance and adaptability. However, precise control of complex musculoskeletal systems is still subject to active research as achieving precision with such systems can increase the control effort dramatically. In this work, this disadvantage was addressed

and based on the control architecture that can be found in vertebrates. A bottom-up approach was followed to investigate possibilities to decrease the complexity of precise control through multi-leveled behavior of less complex control schemas. Figure 1.1 illustrates two parts of the human nervous system.

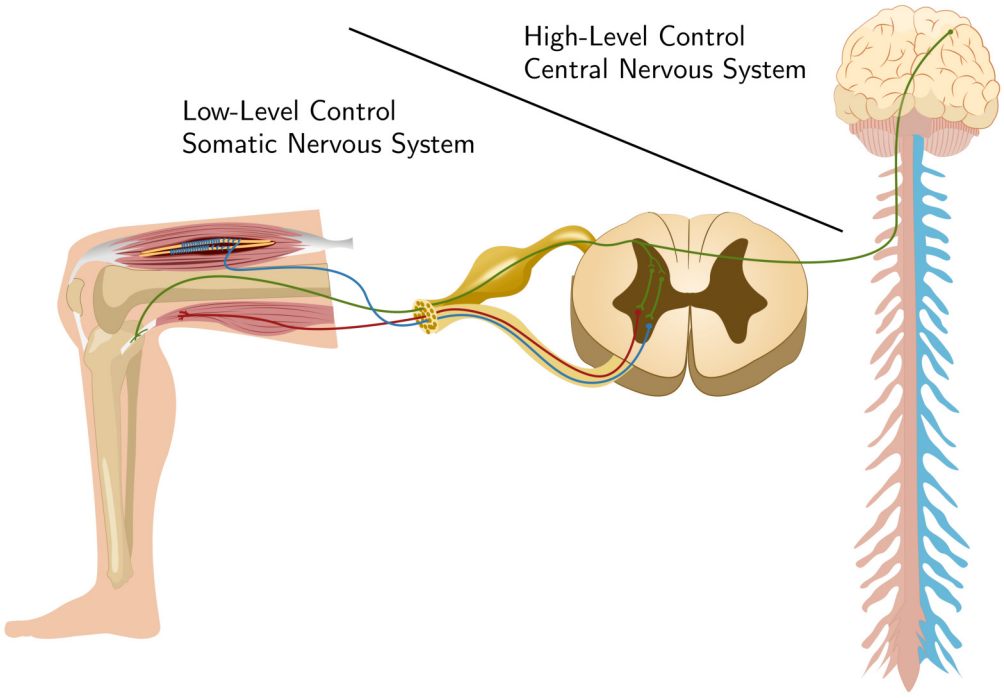

Figure 1.1: This image illustrates the regions of the nervous system that are responsible for the lower and higher levels of biological motor control.

The central nervous system is where conscious behavior originates. The somatic nervous system is the part of the peripheral nervous system that relays the motor commands from the central nervous system to the muscle's motor pathways, resulting in the muscle's actual contraction [39]. This hierarchical structure absolves the central nervous system from the detailed task of controlling the contraction of every single muscle. Based on this biological insight, the goal for this work was set to investigate and realize a system based on the model of the human central and somatic nervous system that subdivides the task of controlling a musculoskeletal system and allows the central decision-based control to be less complex through the usage of motor-unit like control of actuator pairs which has a low complexity reflex-like structure.

This thesis consists of six chapters. In the following chapter 2, we will introduce the upper musculoskeletal body we designed and build for our investigations control approaches for musculoskeletal systems. In that chapter, we will show the physical details of our system. The robot was designed to recreate the structural properties of a human upper body closely. This was achieved by using

pneumatic artificial muscles in combination with a skeletal system adopted from the human skeleton. Most joints were trivial to recreate using combinations of hinge and ball joints; however, the creation of a functional shoulder was posed a more complex problem. Contrary to other robots recreating the human anatomy, we decided not to simplify the shoulder through the usage of a regular ball joint. The human shoulder does not represent a ball joint that is statically connected to the torso. The Scapula, Humerus, and Clavicle enable the shoulder also shift on the torso while also providing the three degrees of freedom of the ball joint formed by the head of the Humerus and the socket formed by the Scapula. The whole robot was actuated by 27 McKibben pneumatic artificial muscles. Each actuator was further equipped with an artificial interpretation of a Golgi Tendon Organ so the strain on each muscle can be measured. This system was used for several collaborative research works intending to create a control model that allows the robot to perform tasks like reaching or the actuation of mechanisms like a crank. We then showed that our system could replay trajectories using sequences of keyframe poses and the advantages of its compliance for the actuation of a crank.

In chapter 3, we will present our initial design for an artificial muscle spindle. This design was based on the implantation of two pieces of conductive fabrics in between the inner rubber tube and the outer braided sleeve, a McKibben pneumatic artificial muscle. These two fabrics had different electromechanical properties. One was piezo-resistive, while the other varied its resistance when stretched. With this design, we aimed to reproduce usable inflation feedback from variants of the Ia and II afferent neurons of biological muscle spindles through the positioning and the actuator. Through our experiments, we could show that this bio-inspired design is capable of creating feedback regarding the current inflation state of the actuator. This design of two sensors per actuator further allowed the detection of strain on a deflated actuator through the piezo-resistive sensor. However, this design was highly prone to fatigue breakage. It, therefore, required improvements in its durability to be considered a practical solution that can be deployed into complex, long-running musculoskeletal systems.

In chapter 4, we will introduce our improved design of an inflation sensor for pneumatic artificial muscles. The main focus of this work was the drastic improvement of the sensor's longevity. As our earlier design was highly integrated into the actuator, we further aimed for a negligible increase in size as well as a flexible structure. We achieved this through the usage of only one type of conductive fabric, which is wrapped externally around a pneumatic artificial muscle. This design achieved several goals. It was still flexible, could be deployed and transferred between existing actuators, and the production process was drastically simplified. In our publication, we further deeply investigated the characteristics of strain-based sensors made from conductive fabrics. Through our experiments, we could show that the two fabrics used were capable of creating usable feedback of the current inflation state of a pneumatic artificial muscle. Besides being able to note that the fatigue breakage issue of the former design was resolved, we further investigated the long-term change of the fabrics' electrical characteristics.

Chapter 5 will introduce our control architecture to achieve compliance for an antagonistic muscle pair actuating a joint. Our approach is based on a reflex-based model using the feedback of tensile force sensors. We chose this type of architecture based on our assumption that compliance in muscular systems does not necessitate complex controllers but that the physical system itself provides enough inherent intelligence that the continuous routing of feedback for the purpose of behavior inhibition is sufficient.

Chapter 6 will summarize the results of the individual publications and discuss future studies to further the findings of this work.

1.1 Related Works

As a significant part of this work is concerned with the development of sensors for musculoskelatal systems we would like to introduce related approaches and explain how over design is differing from those.

Resistance

In 2005, *Wakimoto et al.* [66] published a method to attain feedback of the PAM's inflation. They achieved this by applying a conductive resin ink with a thickness of around $100\mu m$ to the muscle's inner rubber tube. This ink consisted of carbon particles in a toluene solution. In their experiments, they could control a revolute joint using a PI controller and referencing the result to an integrated potentiometer. Antagonistic control of two opposing muscles was also experimented with. Their sensor's feedback evaluated its static and dynamic characteristics. This design integrated the feedback into the actuator and would work in a complex system of adjacent muscles.

Hamamoto et al. [19] presented a stretch sensor that can be longitudinally attached to a PAM in 2006. Their sensor was made of a carbon-coated nylon string, which sleds through an additional electrode. Therefore, this setup could be used as a linear potentiometer when the string and the electrode were fixed on the outside of the PAM. In their paper, they evaluated the static characteristics of their sensor.

Kuriyama et al. [35] designed an external sensor that can be wrapped around a PAM to measure its inflation in 2009. They built a soft stretch sensor formed as a ring by layering electro-conductive rubber. Based on the inflation at one location of the muscle, they could estimate the respective length. They evaluated the static and dynamic characteristics based on the feedback of a linear potentiometer. They also showed the viability of their sensor by deploying it to a 2-link-manipulator.

Park et al. [57] proposed a custom design for a PAM that implemented eGaln filled microchannels to sense the deformation of their actuator in 2013. Their design differed from the widely used McKibben design, which uses an inner elastic tube and an outer constraining braid. The design they proposed embedded kevlar strings into a multi-layered elastomer tube. The inner layer contained the constraining kevlar strings, and the outer layer contained a helical microchannel filled with eGaln.

Besides the description of their design, they also presented its static characteristics.

Hirai et al. [22] proposed a sensor that consisted of an electro-conductive yarn woven into the PAM's outer braided sleeve in 2015. Measuring the change in resistance due to the inflation of the actuator allowed them to estimate its length. They verified their model for this sensor for its static and dynamic characteristics.

A previous embedded version of the sensor we propose in this paper was presented by us in 2019 [23]. The design of that sensor consisted of conductive fabrics, which were place in-between the inner rubber tube of a McKibben muscle and its outer braided sleeve. This sensor showed good performance regarding its feedback but was prone to fatigue breaking of its wires due to shearing forces.

Sakurai et al. [63] investigated the suitability of reservoir computing based neural networks to model the displacement of a McKibben muscle. To generate feedback, they blended the inner rubber tube with carbon particles to increase its conductivity. The resistance over the length of the actuator changed due to the deformation. This feedback was used to fit their echo state network to estimate the length of the actuator based on its resistance. They statically presented the relationship between resistance and actuator length, as well as evaluating the dynamic estimation performance of their model using a saw-tooth like waveform for the pressure inside of the actuator.

Capacitance

Goulbourne et al. [18] proposed a method to generate feedback for McKibben muscles in 2007. Their design is based on the usage of dielectric elastomers, due to the fact that typical elastomers are acrylic and silicone rubber, where the latter is a popular choice to build McKibben muscles. They tested several materials for the electrode, such as carbon and silver grease, as well as graphite powder and spray. The evaluation of the individual properties was performed on a diaphragm. Based on those results, the performance inside a McKibben muscle was modeled afterwards. Just like the design of *Wakimoto et al.*, a design like this could be seamlessly integrated into a PAM.

Nakamoto et al. [44] presented a design of a stretch sensor made from three layers of polyurethane and two electrodes made from carbon nanotubes in 2014. They evaluated the performance of their sensor by attaching it to a PAM using a jig. Using this setup, they provided the static characteristics of the design. Measuring the capacitance, they were able to estimate the sensor's current length and, therefore, the PAM's.

Yuen et al. [72] proposed a new design for a PAM with two integrated stretch sensors in 2018. A distinguishing feature of this design was its capability of sensing inflation and bending of the actuator. They measured the change in capacitance to estimate the deformation of the stretch sensors. Their evaluation of the sensor was done for its static characteristics.

Inductance

Felt et al. [15] published a design for a McKibben PAM, on which they replaced the outer braided sleeve with a mesh of insulated wires in 2015. This structure allowed them to measure differences

in its inductance, which they modeled using the Neumann formula to predict changes in inductance based on the deformation. They evaluated their sensor design under load for its static and dynamic characteristics.

Erin et al. [12] presented a design using a braid of insulated wires wrapped around a McKibben muscle in 2016. This design allowed them to measure a change in inductance due to the deformation of the PAM. Their evaluation illustrated the static relationship between inductance and force, inductance and displacement, and displacement and force.

Voltage

Akagi et al. [2] proposed a design using photoreflective sensors to measure the inflation of a PAM in 2012. They built a two-sided circuit board with a photoreflective sensor on each side, which they insert into the inner tube of their PAMs. The wires needed for the power supply and the data is passed through an airtight coupling they designed. In their paper, they also provide a transfer function to estimate the length of the PAM. A load was also used when they evaluated the static and dynamic properties of their sensor.

Yano et al. [70] presented a sensor, which got inserted into the inner rubber tube of a McKibben muscle in 2020. They measured the inflation using two hall effect sensors on a double-sided circuit board. This design is similar to the design of *Akagi et al.* from 2012. To measure the inflation, the feedback voltages of the hall effect sensors were used. The viability of this approach was shown through the evaluation of the sensor's static and dynamic properties.

Pressure

Yokoyama et al. [71] published a completely sensor-less approach to determine the length of a McKibben muscle in 2018. They achieved their goal using an unscented Kalman filter. The viability of their model was evaluated for its static and dynamic characteristics.

By studying the valuable preceding designs published approaching to generate feedback for PAMs, we can observe repeating patterns of design choices. In Table 1.1 we compiled the key aspects of each former study regarding their applicability in experiments conducted with PAMs. In this table, we compared the size, placement, longevity, cost, complexity, and measured property in relation to each other. The size considered the ratio of sensor and actuator. The placement is viewed as internal if the sensor is part of the actuator's structure and external if it could theoretically be removed from the actuator. The longevity could only be roughly estimated but represents a crucial aspect of a sensor design. We tried to guess the longevity based on the deformation and friction a sensor is exposed to. If a sensor was significantly deformed during operation and the sensor's material can be considered vulnerable to those, we estimated the longevity would be shorter than less deformation using a non-brittle material. The cost was estimated by the number of customized components and production steps. A sensor that can be produced in-house with off-the-shelf components is considered less expensive than a sensor using materials that have to be made just for this sensor. A sensor's complexity is assumed to be lower if it consists of fewer individual parts and needs a

Table 1.1: In this table, we compiled the previous research's key properties directed towards the generation of feedback from soft actuators. Size was interpreted in terms of the relation of the actuator to sensor dimensions. Placement describes a sensor as internal if it is part of the actuator's structure and external if placed onto and being theoretically removable from the actuator. The longevity was estimated by the exposure of the sensor to friction, deformation, and their presumed effect on the sensor's structure. Cost is treated relative to the availability of off-the-shelf components and materials, as well as the dependency on specialized production processes. Complexity describes the number of individual components, their assembly, and the means to generate feedback. Under measurements, we list the physical properties, which the generation of feedback is based on.

Article	**Size**	**Placement**	**Longevity**	**Cost**	**Complexity**	**Measurements**
[66]	small	internal	middle	middle	low	resistance
[19]	middle	external	middle	low	middle	resistance
[35]	small	external	long	low	low	resistance
[57]	small	internal	long	high	high	resistance
[22]	small	internal	middle	low	low	resistance
[23]	small	internal	short	low	low	resistance
[63]	small	internal	long	high	low	resistance
[18]	small	internal	long	low	low	capacitance
[44]	big	external	long	low	low	capacitance
[72]	small	internal	long	middle	high	capacitance
[15]	small	internal	long	low	middle	inductance
[12]	small	external	middle	low	low	inductance
[2]	middle	internal	long	high	middle	voltage
[70]	middle	internal	long	low	middle	voltage
[71]	middle	external	long	middle	low	pressure

smaller amount of production steps to be made. Lastly, we listed the physical property, which is measured to generate the feedback of the sensor. This information could be taken directly from the publications.

Our goal was it create a design for an inflation sensor for PAMs that can be simply and cheaply produced to enable its usage in more complex systems. Therefore, we aimed to allow generic PAMs to be equipped with our sensor while changing their shape and dimensions by the least possible amount. This is an inference from our aspiration to allow the usage in more complex and cramped systems, where a change in shape away from a smooth cylinder could dramatically increase the friction of adjacent muscles. Further, our design had to be simple regarding its number and availability of components, where all components should be flexible to be consistent with our first requirement. The last demand was that the production process should involve a small number of manual steps and no need for specials tools.

Considering these goals for our design to be a generic low-profile replacement, that can be simply produced, we can state that designs like [66, 18, 57, 15, 22, 12, 72, 63] would not satisfy our requirement for being used on existing PAMs as these designs are based on special materials the PAM itself is made of. In these cases also the production complexity, due to the special materials and

process is much higher. Further, as the sensor is part of the muscle, it will also break with the muscle and can not be reused on another existing PAM. When considering the low-profile requirement for the designs [19, 44], we can note that they would drastically change the actuator's shape and add friction points for adjacent muscles, which could potentially break them much faster.

The designs [2, 70] do not strictly need special production processes as the first group of designs, but they involve their insertion into the actuator. The nearest does the design of *Kuriyama et al.* [35] come to the goals we outlined as desirable for a sensor for PAMs. Regarding complexity, our design represents an improvement; as the amount of probe wires is smaller, and the production of one of our sensors consists of a few simple steps. As the most significant advantage, our actuator's change in shape is almost negligible in our design. Based on the desired features for a soft sensor we presented, we can show that the previous research originated numerous designs to sense the inflation of a PAM. But once it comes to simplicity, price, re-usability, and the possibility to retrofit a sensor to existing muscles on the design of *Kuriyama et al.* satisfy most of these demands. When comparing this design with ours, we further could show that the additional drastic reduction in size and slight improvements to the production process's complexity shows a novel way towards soft inflation sensors for PAMs.

Chapter 2

Anthropomorphic musculoskeletal 10 degrees-of-freedom robot arm driven by pneumatic artificial muscles

2.1 Introduction

Biologically inspired robotics have been gathering considerable attention both to understand living organisms and to exploit them in robotic designs. Musculoskeletal systems (MsS) are a key morphological feature of humans. Therefore, the development of musculoskeletal robots has been widely used as a method to understand the motoric capabilities of humans. So far many types of musculoskeletal robots have been developed [28, 43, 42, 46, 45, 3, 40, 31, 1] and their advantages and applications have been published in recent years. Generally speaking, imitation of the MsS in robot development is already challenging due to its complexity, and the limitations of current technologies. Therefore, when robots are used to investigate MsSs in humans, they face a trade-off between their biological plausibility and motor capabilities.

There are two main ways of actuate robots, electrical motors and pneumatic artificial muscles (PAM). Regardless of the kinds of actuators used the research shares the same motivation, to accurately recreate human motor function. The robot *Kenta* [28], which *Inaba et al.* introduced in 2003, is one of the most important works in the field of musculoskeletal robots. This research group has been continuously reporting developments of musculoskeletal humanoid robots [43, 42, 46, 45, 3]. The newest robot *Kengoro*, which has 114 tendon-driven degree of freedom (DoF), was designed to

be as close to the MsSs of humans as possible. In this case accurate control of the actuators is achieved through the use of electrical motors. Recently pneumatic artificial muscles consisting of bundles of pneumatic tubes have been developed by *Kuruyama et al.* [36]. These aim to realistically mimic the structure of biological muscle, without necessarily improving the functionality of the robot. The main applications of these robots are biomechanics and rehabilitation, and therefore the biological plausibility of their mechanical system and its accurate actuation are regarded as important. However, the systematic advantage provided by the MsS to robot control has not been investigated.

In order to focus on how musculoskeletal structures work in relation to motion control, they are modeled and implemented to emphasize the relationship between the actuation of muscles and the torque of joints. As such, fundamental research into the behavior and function of specific components that comprise musculoskeletal systems has been performed. For instance, the *HUMA* by *Okadome et al.* [53] and the robot arm by *Tondu et al.* [64] have simplified musculoskeletal structures which allow for more detailed study of the dynamics and mechanics of the key components, such as actuators. When considering more complex structures, such simplicity is insufficient for modeling and control. Therefore, although this approach would offer comprehensive models in terms of robotics, if the functioning of complex musculoskeletal structures of humans is not based on the framework of control theory, it is difficult to be able to compare them.

When considering a compound action like walking, such mechanically simplistic systems are insufficient. More complicated systems of actuators and skeletal structures are required. Furthermore, such systems often mimic human biological structures. *Niiyama et al.* achieved jumping and landing using simple rule-based control [50, 49, 51]. *Narioka et al.* developed a walking robot based on passive dynamic walking [47] and showed that it can achieve stable walking also by a simple rule-based control system [48]. Regarding robot arms, *Hosoda et al.* demonstrated a door-opening task, and *Ikemoto et al.* a ball throwing task [25, 27]. In these studies, we can find both simple and complex pneumatic MsSs, where the task evaluated are sufficiently broadly defined that the imprecise nature of the pneumatic muscles is not an issue. However, it is clear that making MsSs more complex leads to improved task performance, which would be hard to obtain by using other schemes. Furthermore, because these robots are typically difficult to model and control. Even for individual actuators the controller is inevitably specialized for a given task. In fact, in the above mentioned studies their controllers are completely different, making it difficult to discuss and compare their results on the same basis. As shown so far, the design principle of the robot greatly differs depending on the main purpose of the research. Figuring out an appropriate compromise between performance and structural similarity is crucially important.

In this study, we created a pneumatically actuated musculoskeletal robot arm for the purpose of performing complex compound actions.The features of the robot arm are

- A metal and carbon fiber skeleton developed from [26].

- Pneumatic muscles using the same implementation as [50, 49, 51, 47, 48, 25, 27].
- It has ten degrees of freedom of motion.
- The skeleton system is self supporting while retaining a human-like range of motion.
- The control system is designed to be easy to use and portable.

We demonstrate that our robot is suitable for performing specific motor skills, through a series of experiments and tests.

The rest of this document is structured as follows. Section 2.2 describes the hardware structure, muscle apparatus, and control system. Section 2.3 details the software structure and design. Section 2.4 presents the results of the task evaluations, crank rotation and trajectory following.

2.2 Hardware-Characteristics

In this section the robot's hardware design decisions are described and illustrated. As its objective is to closely mimic humanoid manipulatory behavior, the human body's structure was considered as the reference design. We produced a simple and reliable model of the human shoulder and arm, imitating the key mechanical components. This allowed for a manageable and reliable system while providing a similar range of motion to the real thing. A proposal published by *Hosoda et al.* [25] was examined and scaffolded this process. On this foundation further design iterations focusing on the optimization of the muscle routing were made to reduce the friction against each other and the skeletal structure. This step resulted in a longer life-cycle of the individual muscles as well as enhanced motor skills.

2.2.1 Skeleton

The skeleton as the supportive structure provides attachment points for the tendons and muscles, further does its linkage structure imposes mechanical constraints onto the body's range of motion. Also this structure offers stability that can be utilized when applying forces to its environment. In addition, they govern the work envelope of the limb and define the space of movement to operate in. Movements executed within this space can be considered human-like as they adhere the same underlaying physical limitations. Bones like the humerus, ulna, carpals, metacarpals, and phalanges are directly adopted including their spatial relation, proportions and mechanical properties. The shoulder mechanism was particularly difficult to implement in direct correspondence with nature. The design published by *Ikemoto et al.*[26], which is considered preliminary work of this robot, solves this problem by replicating the range of motion of the human shoulder, while being self supporting. This design proved viable and was therefore used in the final robot.

Fig. 2.1 shows a direct comparison of the human upper body skeletal structure and a CAD rendering of the robot. Regarding their proportions and composition, it is evident that they are nearly identical. The shoulder linkage mechanism offers very similar capabilities of the human shoulder apparatus. An earlier design was closer to the human linkage of clavicle and scapula, however its bones tend to separate unless held in place by a coupling muscle. The design of *Ikemoto et al.* solved this problem through a series of sliding joints in combination with four ball joints. We therefore adopted this design and altered it according to our needs for muscle connection points.

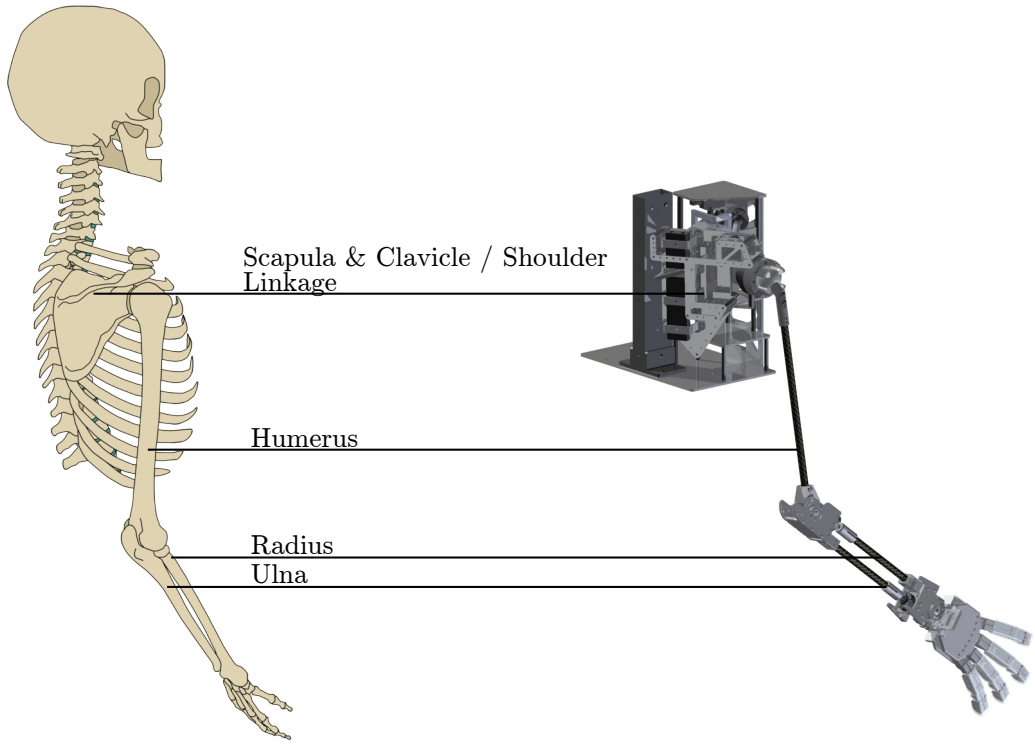

Figure 2.1: This side-by-side comparison illustrates the structural resemblance between the human anatomy of the upper body and the robot presented in this paper. The arm is construction-wise identical to a human arm. The shoulder joint made of clavicle and scapula is replaced with a shoulder linkage mechanism.

The close adoption of the human skeletal structure allows a similar muscle routing as the joints and attachment points have related dimensions and can be found in akin locations. Regarding its range of motion, this configuration enabled the robot to execute human-like movements with minimal control as its musculoskeletal system governs the movement according to its internal constraints. This allows the robot to utilize a human comparable set of manipulative capabilities.

2.2.2 Muscle Apparatus

Realistic anthropomorphism of the robot is one of its design goals. Therefore, a mechanically comparable alternative to biological muscles was needed to actuate the robot. Comparable characteristics of flexibility and compliance as well as strength were the main points of focus for the muscle selection. Using pneumatic artificial muscles was as a viable option as they are easy to produce and their characteristics in respect to compliance and strength are sufficiently similar to biological muscles. The actuation is realized with proportional valves which allows continuous contraction at varying speeds. Pressure control was implemented with pressure sensors located near to the individual muscles, which feed back information to *PID* controllers.

Biological muscles have different sensory receptors used for force control, sensing, and the triggering of reflexes. To integrate this additional source of feedback and thereby allow a more realistic representation human muscle control, a device was developed that senses the muscle's tension. It was inspired by *Golgi Tendon Organ* [61] which senses the force a muscle is exposed to. Further is it hypothesized that together the parameter sets of muscle pressures and tensions is sufficient for determining the spatial positioning of the hand and arm, allowing basic forward kinematics.

Fig. 2.2 shows a correspondence between the muscles of the human shoulder and arm with the robot's components. The image of the human includes only the muscles which were finally adopted on the robot. When selecting which muscles to adopt, often sets of adjacent muscles were combined into a single muscle, or single small muscles was omitted. This is due to the fact that a bundle of PAMs would not function in the same way as a bundle of real muscle and sufficiently small muscles cannot be accurately simulated by PAMs.

Pneumatic Artificial Muscle

The muscles used for this robot following the McKibben design [10] which offers an affordable approach to building individual muscles. As muscles are exposed to mechanical abrasion, due to their continuous actuation and reciprocal friction, they wear down over time, changing their properties and eventually breaking. This design has the benefit of being easy to build, cheap, fast to replace as they are built in-house.

The muscle itself, as seen in Fig. 2.3, has a simple construction. A rubber tube is plugged at one end and connected to the supply air line on the other. This assembly is put into a braided sleeve which limits and guides the inflation of the rubber tube, keeping it from rupturing when pressurized up to 0.87MPa. As the tube expands so does the braided sleeve. The braided sleeve's diameter is approximately inversely proportional to its length. Therefore, as the rubber tube expands, the muscle decreases in length.

Assuming no external forces, based on the sleeve's known contracting properties its precise length as a function of its current inflation can be calculated using the method described in [7]. However when friction between sleeve and tube is accounted for [10] and worsened by factors like wear or

the bended routing of the muscles the real values diverge from the theoretical predictions. These uncertainties make additional sensory feedback necessary for a reliable state model of the robot.

Controlling these muscles is trivial and can be accomplished by either a proportional or a solenoidal three-port valve. For this robot proportional valves are used to allow an easier flow control for pressurizing the muscles evenly at varying rates.

Further worth noting is their robustness to collisions with the environment or stretching by external interaction. In such situations the muscles benefit from their inherit compliant characteristic. Additional external force can be applied to the pressurized muscle, stretching it to some degree, without causing damage.

This feature can be exploited for slipping around obstacles in case of collision or passive retreat if a human applies a force opposing the robot's current trajectory.

In summary, pneumatic artificial muscles following the McKibben design provide inherit compliance, are affordable and due to their simple design are easy to build. These properties made them the most favorable choice for this robot.

Muscle sensory feedback

Prochazka et al. [60] showed that a key aspect of controlling a musculoskeletal system is sensory feedback from the muscles. For this robot an artificial Golgi tendon organ [61] is used as an additional sensory receptor. The actual organ is part of the junction between muscles and tendons, consisting of collagen and a single afferent nerve fiber. This kind of receptor reacts to the tension applied to a muscle.

Our artificial version of this organ is a linear strain gauge. With this feedback, forces applied to the robot can be can be detected and measured without involving tactile sensors. Due to the simplicity of its function and its small size it can be externally attached to the muscle.

Our current approach towards the development of motor skills is using the pressure sensors' feedback in combination with the artificial *Golgi Tendon Organ* and motion tracking to train a neural-network for forward/inverse kinematics.

Our design of an artificial Golgi tendon organ is illustrated in Fig.2.4 and consists of a single strain gauge on a mounting bracket. Given the number of muscles adjacent to each other the bracket's size needed to be minimized. Therefore, the Wheatstone bridge for each individual gauge is realized externally. This allowed a further reduction in size of the artificial Golgi tendon organ to a point where an additional saving in size would effect its stability when typical forces (up to 50 kg) are applied.

2.2.3 Control System

The robot was designed to be operated by a single control system providing low-level control of the air valves and the reading the pressure and tension sensors. In addition to this, the system should

use the Robot Operating System (ROS) to provide a well documented communication framework. This decision prevented the use of a powerful microcontroller in favor of a single-board-computer (SBC) which also already provides a network interface for connectivity. For electronic control, custom PCBs were designed and manufactured for the digital-analog (air valves) and analog-digital (pressure sensors) converters as well as the bridge transducer (tension sensors).

The requirement that the control system utilizes ROS for communication as well as controlling the hardware implied the use of a realtime enabled Linux kernel. This was achieved by using the RT-Preempt patch-set. This design decision influenced the interface type that was used for the communication between control system and the Converter-ICs. A communication type that is widely used is Ethercat which can be found in many industrial applications. This solution requires specialized ICs on the slave side and would have increased the complexity and cost of the controller design. Therefore it was replaced by an SPI bus, which is natively available on the Raspberry Pi 3B. The necessary determinism for accessing the bus on the Raspberry Pi 3B was achieved with a userspace driver. A drawback is the comparatively small main memory of 1GB. The planned software architecture utilizing dynamically loadable controllers for each muscle causes some overhead. As swapping is not an acceptable option due to its impact on the system's latency, the memory usage was optimized by creating a customized Linux system. The memory usage was drastically reduced by the creation of an optimized Gentoo based Linux system.

2.3 Software-Characteristics

In this chapter we will describe details of the software design decisions. The design of the driver and the architecture chosen for the ROS based parts used for communication and control will be discussed.

One early design decision was the use of ROS to support a fast and structured development of experimental applications. The main features justifying this decision are the networking capabilities and multiple communication patterns as well as the build system offered by ROS. These were desirable as the robot's architecture required individual development systems to able to be able to command the robot over a network. Separating control and command guarantees the integrity of the low-level driver as it can not be compromised by developers.

The robot presented in this paper is supposed to be a platform for several simultaneous experiments by different researchers. An easy-to-use communication interface is conducive to a fast development cycle. The provided dependency management is another advantage of ROS. Its build system allows dependency satisfaction and consistent builds for the individual developers who are writing software for the robot.

2.3.1 Driver design

The decision for the controller's hardware platform to be a Raspberry Pi 3B was made due to its of computational performance and I/O interfaces like SPI and numerous GPIOs.

The driver executes a realtime enabled context, which reads the sensor values and writes the actuator commands at a rate of 500Hz. As such, the individual muscle controllers are updated at the same rate. Furthermore, the driver instantiates the communication in a non-realtime interrupt driven context. Exchanging and accessing data between these two differently prioritized contexts is orchestrated to guarantee an interruption free main control loop.

A custom implementation of driver code for the converters was developed to achieve additional performance optimizations as the order in which the individual converters were read was sequenced to minimize the overall latency by efficiently using conversion times to issue the next command in the pipeline.

The main improvement to the system latency was the usage of a userspace I/O library, which allowed direct access to the SPI and GPIO controller. This bypasses the issuing of systemcalls by mapping the hardware into virtual memory so the hardware controllers can be instructed directly. Following this approach demonstrated the advantages of the determinism of the driver as the latency of a memory access can be considered as relatively small while a systemcall can have unknown latencies depending on the current state of the fully-preemptible kernel.

2.3.2 ROS architecture

ROS compatibility was one major design goal for the software stack of the robot. The complete IC based communication as well as the topic advertisement and subscription is implemented within the main driver.

The update of the muscle's PID controllers is handled by custom controllers which are spawned per muscle and load their configurations from the ROS parameter server. This design pattern is based on the ros_control [65] interface and provides realtime-safe multi-threading capabilities in combination with the realtime context of the main driver. To this point ROS only provided controller classes for revolute joints and offered control schemes for torque, velocity and position control as well as sensory controllers. Those couldn't be reused for a musculoskeletal robot therefore a new controller class resembling the muscle actuator was implemented. The new class provided control of the internal pressure of the individual muscles as one mode of operation and an activation control mode for controlling the airflow. In addition it applies a filter to the noisy data of the tension sensors.

The activation control allows it to control the intensity of the muscle's contraction directly. For the PAMs this was realized by a corresponding adjustment of the airflow through the proportional valve. These two control modes are analogous to the velocity and torque control of servo motors and therefore represent a musculoskeletal version of the same control ideas.

2.4 Experimental verification of the robot's motoric abilities

We set out to show that the human body structure gives advantages in control for the execution of motor skills by robots. This chapter will present evidence that the robot's mechanics allow smooth movement and precise repetition of trajectories which emphasizes that, despite its unconventional design, the robot's control system is capable of moving the arm in a dexterous and reliable way. We also demonstrate that the musculoskeletal structure combined with the PAMs allow the execution of difficult tasks with simple control input.

The first experiment evaluates if the robot can repeat trajectories with reasonable precision which would allow controlled interaction with its environment or humans. The second experiment illustrates the benefits of the human-like musculoskeletal design to perform constrained tasks with low control complexity.

2.4.1 Results and Discussion

These experiments were designed to show the viability of the robot to fulfil different tasks which typify human movement or human-robot-interaction. Therefore they should demonstrate that the robot is capable of following trajectories repeatedly to emphasize that the control is working and the mechanisms don't induce unstable or jerking behavior. The robot's human-like body structure in combination with the flexibility of its muscles provides an inherently compliant system that can exploits the mechanical constraints of its environment during interaction.

Experiment 1: Trajectory Repetition

Goal: Determine if the robot can repeat trajectories with reasonable precision.

Setup: For the purposes of this experiment it is convenient to provide an abstract model of the robot. The robot consists of a skeletal system with ten degrees of freedom of motion. Connected to this is a system of twenty eight pneumatic muscles. For this investigation we define the measured quantity as the position of the end-effector in space, $\vec{x} = (x_1, x_2, x_3)$. In general, the position of the end-effector is a non-linear function of the pressures of each of the muscles, $\vec{p} = (p_1, ..., p_{28})$, M physical parameters of each muscle, $\alpha_{i=1,...,28}^{k=1,...M}$,

$$\vec{x} = \vec{x}\left(\vec{p}, \alpha_i^k, \Lambda_L\right) = \left(x_1\left(\vec{p}, \alpha_i^k, \Lambda_L\right), x_2\left(\vec{p}, \alpha_i^k, \Lambda_L\right), x_3\left(\vec{p}, \alpha_i^k, \Lambda_L\right)\right) \tag{2.1}$$

and the L relative spatial configurations of the muscles and skeletal components, which we denote Λ_L, which determines the form of the functions x_j. The physical parameters of the muscles include quantities such as the elasticity and internal friction and are in general of the form $\alpha_i^k = \alpha_i^k\left(\vec{p}, \frac{d\vec{p}}{dt}\right)$. For the purposes of this experiment we do not know the form of the functions $\alpha_i^k\left(\vec{p}, \frac{d\vec{p}}{dt}\right)$, and by observation we know that the dependence of $\vec{x}$ on these quantities is weak. As such we treat them

as a source of random error. We are unable to construct a theoretical form of the functions x_j as their dependence on Λ is too complex. Indeed Λ is dependent on $\vec{p}$. Again, by observation we know that the dependence of Λ on $\vec{p}$ is weak for small variations in $\vec{p}$, and we treat it as source of random error. Taking these approximations into account, we find that

$$\vec{x} = \vec{x}\left(\vec{p}\right) = \left(x_1\left(\vec{p}\right), x_2\left(\vec{p}\right), x_3\left(\vec{p}\right)\right) \tag{2.2}$$

To generate a trajectory we define an initial point $\vec{p}_I(t_I)$ and final point $\vec{p}_F(t_F)$, in pressure space and vary each pressure $p_i = t(p_{i,F} - p_{i,I})/T$, where T is the total time taken to complete the movement. Given the approximations we have made each set of initial and final pressures correspond to a unique trajectory. In reality, a repetition movement from one set of pressures to another will result in different trajectories. These differences can be attributed to variations in Λ which cannot be accurately configured to be the same for different runs, and error in the measurement of $\vec{p}$. Another source of error could be the wear and tear of the components of the robot. However our measurements were taken over a short time period, making such problems negligible.

Command generation: We subdivided the change in pressure space from $\vec{p}_I$ to $\vec{p}_F$ into 600 intermediate pressure configurations. This number was derived from a pressure update rate of 100Hz over a total time $T = 6s$. This resolution was chosen to avoid covering possible jerky movements by a fast execution and to increase the tracking coverage. Further does this decision allow for continuous movement as the response time of the muscles was found to be longer than the update rate for small pressure changes. This is caused by the chosen PID parameters of the muscle controller. At the midpoint of the task the robot executes the trajectory in reverse to complete the movement, reaching its initial position. One closed movement is considered as one trial which was repeated thirteen times. As illustrated in 2.7 the velocity of the end-effector is 6-12 cm/s. Therefore these trajectories represent consistently smooth movement at a reasonable speed as this scenario was assumed to be representative of common behavior of a humanoid robot when executing dexterous tasks.

Measurement: For observing trajectories a common method is tracking the end-effector's position by continuously computing its forward kinematics. This is not possible for this experiment due to the robot's lack of positional sensors. Therefore a motion capture system was used to track the hand's position during trajectory execution. Each trajectory was repeated thirteen times and tracked at a rate of 55Hz. The standard deviation of the error in the measurement of the position of the end-effector was found to be 0.847cm on the x-axis, 0.142cm on the y-axis, and 0.241cm on the z-axis.

Results: The analysis of the tracking data can be seen in Fig. 2.7 and 2.8. One can see that the movements are executed consistently without outliers or major jerks. These figures indicate a consistent performance during the robot's trajectory execution. The visualization in Fig. 2.7 shows the standard deviation of the tracking during trajectory execution. The fact, that no larger

increase can be observed during movements allows for the assumption that our tracking method was sufficiently accurate and stable. The measured speed of the end-effector was measured at 6-12cm/s. Further does the scatter plots in Fig. 2.8 show evidence for our initial assumption that the final trajectory is dependent on $\vec{p}_I$ and $\vec{p}_F$. It is clear to see that the average trajectory (red) diverges in the middle of the trajectory. This could be caused by the different initial parameters like internal friction. This experiment evaluated that the standard deviation during trajectory repetition to be 8mm. We consider this degree of precision as sufficient for the experiments we are planning to conduct using this robot. For motor skills like grasping an object the inaccuracy shouldn't be bigger than the radius of the biggest cylinder graspable with a completely open hand. Providing this degree of accuracy allows objects to slide into the hand of the robot even when not perfectly approached. For our robot this requirement is met as the current hand can grasp cylindrical object up to 8cm in diameter. For experiments including human-robot interaction this level of precision is also sufficient for tasks link handshaking or passing over objects.

Experiment 2: Crank Rotation

Goal: To ascertain whether the robot can exploit external mechanical constraints to perform a task with a low complexity control scheme.

Setup: We decided to use the operation of a hand crank as the task in this experiment. Fig. 2.9 & 2.10 show the experimental setup during the experiment. The end-effector of the robot is loosely bound to the handle of the crank. The crank itself is free moving with negligible resistance to rotational movement. The crank shaft apparatus is attached to a table and the central axis is placed approximately 40cm to the right and 45cm in front of the center of the body of the robot. This placement offered the greatest freedom of movement to the robot. This ensures the outcome is not influenced by operating near the bounds of the work envelop, which might be influence by extremal values of the muscle tensions. The distance between the robot and the crank was two thirds of the maximum distance the robot can reach forwards.

Command generation: For the crank rotation experiment three poses were defined to turn the crank counterclockwise. Each pose is defined by a pressure configuration $\vec{p}_1$, $\vec{p}_2$, and $\vec{p}_3$. Spatially, the poses are defined at $\theta_1 \sim 10°$, $\theta_2 \sim 170°$, and $\theta_3 \sim 190°$, where all angles are measured in a anti-clockwise direction about the center of the crank. The zero position vector is anti-parallel to the normal vector to the face of the robot. After the third movement the arm was pulled back into the initial position. At the three stationary positions, the pressures of muscles were designated to be either at 90% or 20% of their maximum pressure. By trial and error, it was discovered which subset of pressures needed to be changed to achieve transition from one pose to the next. We note that the configuration of pressures to successfully complete the task is not unique. The minimum pressure value of 20% of the maximum value was chosen to provide stability.

Measurement: Tracking of the task was performed using a video recording.

Results: The execution of the task is illustrated in Fig. 2.9 & 2.10 where the muscles at 90% pressure are shown highlighted in red. The satisfactory execution of the task supports the hypothesis that the human body structure can be advantageous when operating on constraining mechanisms.

If the control commands are executed when the end-effector is not bound to the handle of the crank, its trajectory greatly diverges from the circular path taken during the experiment. A combination of compliance and internal constraints on the movement range of the musculoskeletal system allow the exploitation of the external constraints enforced by the crank to complete the movement. One can see in the sequence of the first three images in Fig. 2.9 that the shoulder linkage mechanism applies a force towards the center of the crank. This subsequently leads the shoulder mechanism to lift which causes a small rotation of the elbow and turns the hand outwards letting it rotate the crank for the first movement. Also worth noting is that the elasticity of the system is preventing it from inflicting damage on itself when applying a force against an external constraint. In the case of a mechanism like the crank, not only is the robot not damaging itself against the given external constraints but it uses them to guide itself only with a simple control scheme and the characteristics of its body.

2.5 Conclusion

In this paper we introduced a novel musculoskeletal robot actuated by pneumatic artificial muscles. The design is bioinspired, where the structure of the human body was approximated for mechanical simplicity and robustness instead of directly remodeled. Two experiments emphasizing the robot's motoric capabilities were conducted. Experiment 1 validated its dexterousness in slow and smoothly repeating trajectories. The second experiment illustrated how the human-like structural constraints of the robot in combination with the flexibility of its PAMs allowed the operation of a crank using a simple control scheme.

According to these results can it be concluded that the robot is capable of serving as a reliable platform for long-term experiments. Its design and choice of actuators allows for fast and dynamic as well as slow and steady movements, as was demonstrated by the two experiments.

This robot has been built for extensive experimental use, with its design allowing for fast and cheap replacement of broken actuators. This is a major advantage over the widely use method of tendons and motors as they have high maintenance cost both financially and time-wise.

A possible alternative actuation scheme is the use of virtual agonist-antagonist mechanisms, such as introduced by [69]. Their use could eradicate the current shortcomings of PAMs, as soon as complex high DoF systems using such devices can be developed.

2.6 Future Work

The robot platform presented in this paper proved its feasibility for experimentation in the domain of human-like manipulation by mimicking their motoric capabilities. Subsequent research will focus on possible control methods. For controlling musculoskeletal robots there exists a lot of preliminary work [59][67][41][30][33][32][54].

Future work will be focused on learning techniques using neural networks to train a model for forward and inverse dynamics. This aim will be pursued in parallel to experiments utilizing reinforcement learning to achieve various skills like mechanism operation such as doors. It is assumed that the anthropomorphic nature of this robot will scaffold the learning curve for mechanisms designed for human use as the robot can exploit the same traits of its morphology as a human. A third approach is the use off deep q-networks which show a high degree of potential in solving sensorimotoric tasks such as playing arcade games. We hypothesize that the combination of vision, pressure, and tension data will complement this method. We will investigate whether this method can be used to learn motor skills requiring eye-hand coordination such as playing basketball or darts.

Acknowledgements

We thank Mr. Takuya Urino, Mr. Hajime Saito, Mr. Kazuya Yura, and Mr. Satoshi Yamanishi who contributed to the implementation of the hardware.

Funding

This work was supported by JSPS KAKENHI Grant Numbers 16KT0015 and 17H05908.

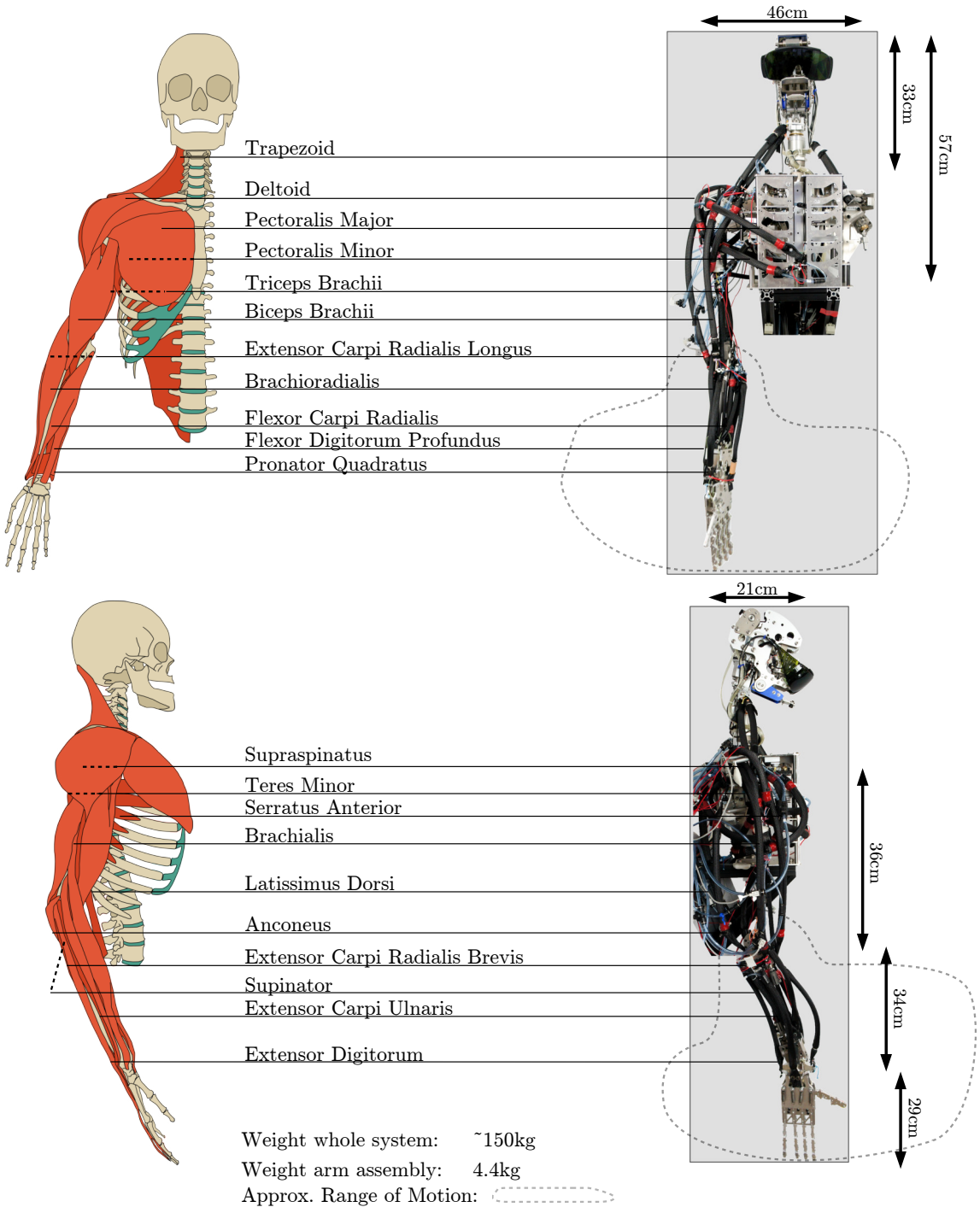

Figure 2.2: The comparing illustrations above should empathize the similarities between the musculoskeletal morphology of the human upper body and the robot presented in this paper. It is obvious that the dimensional relations between the individual body-parts are nearly identical. Further does it list all muscles that were adopted from the human anatomy.

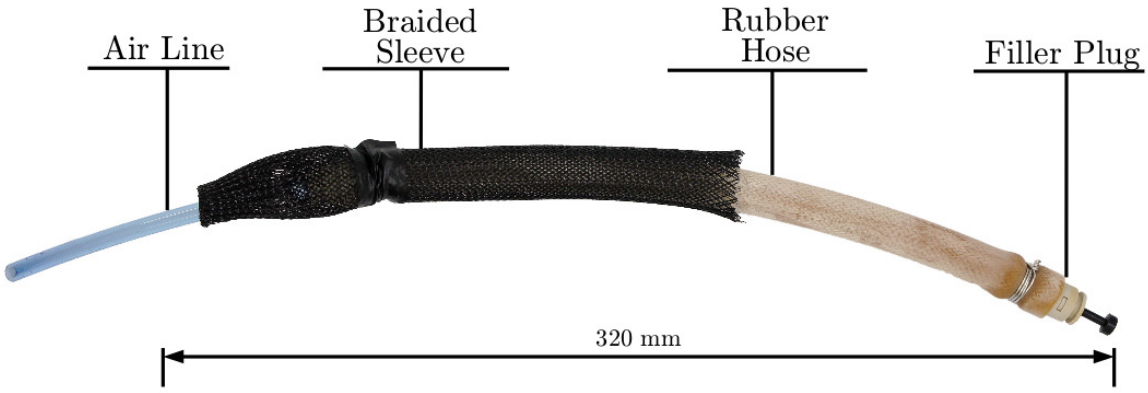

Figure 2.3: Cutaway model of a pneumatic artificial muscle used in this robot.

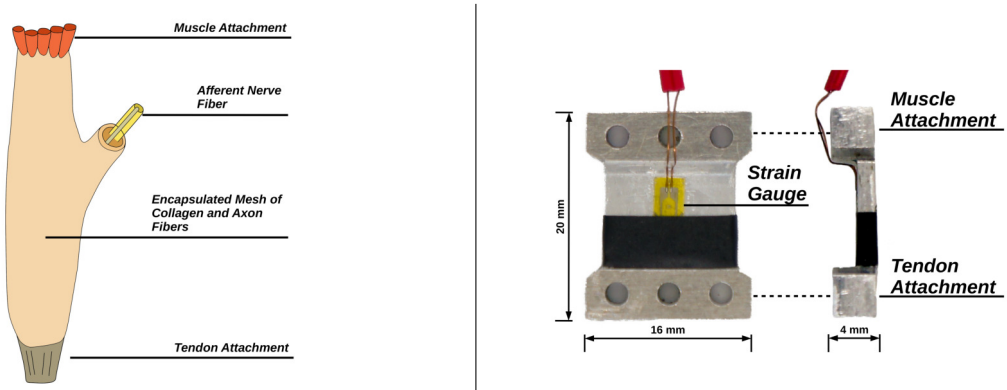

Golgi Tendon Organ | Artificial Golgi Tendon Organ

Figure 2.4: The left image shows a drawing of a human *Golgi Tendon Organ*. It is located in between the actual muscles an the tendons attaching the muscles to the bones. On the right is a photo of our design for an artificial *Golgi Tendon Organ*. It also is placed in between of the artificial muscles and the bones of the robot. Both fulfill the task of sensing the tension a muscle is exposed to.

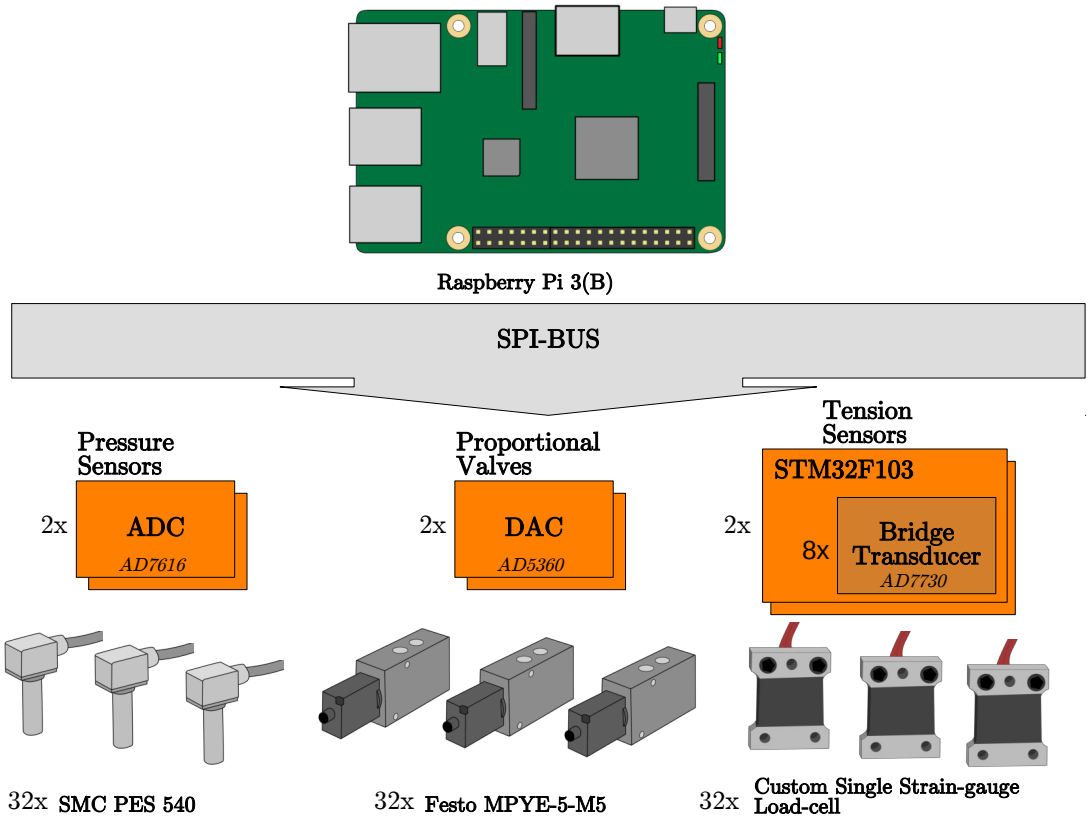

Figure 2.5: This image show the different components which needed to control the robot's muscles. The system at the moment provides a controlling capacity of 32 muscles and therefore the same amount of each sensor/actuator type and ADC, DAC and Bridge Transducer boards. Those controller boards (6 in total) are connected via one shared SPI-Bus.

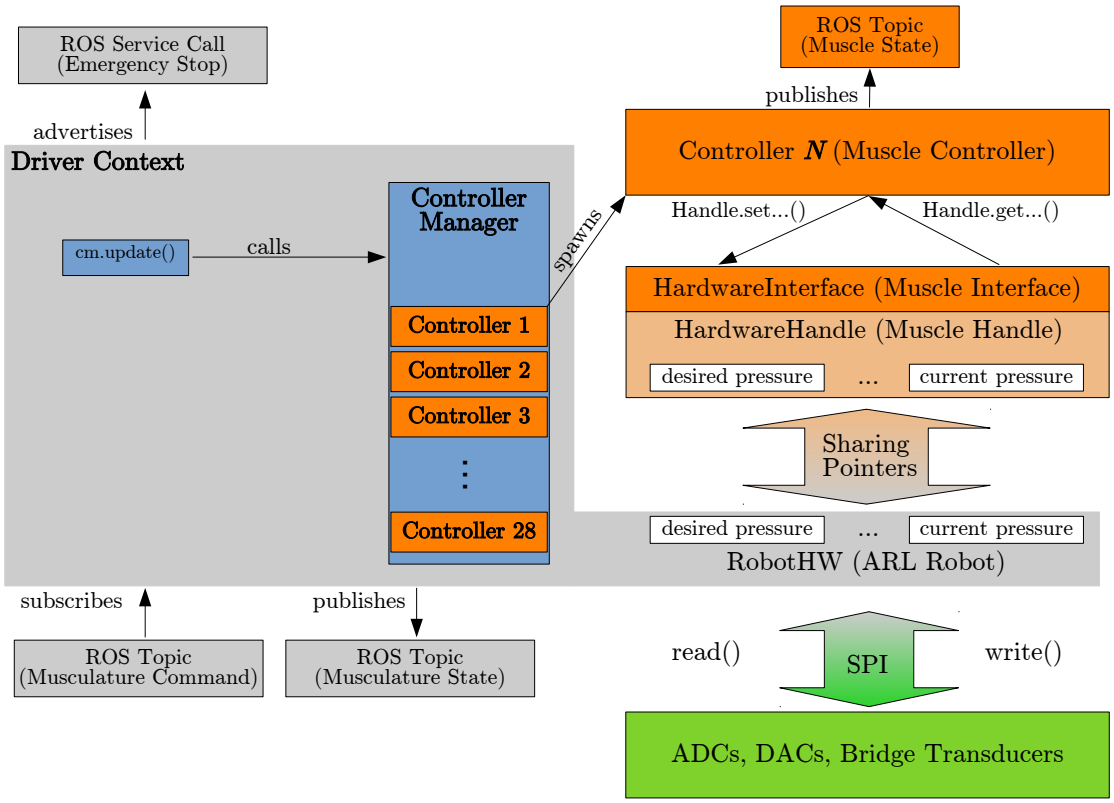

Figure 2.6: This block diagram visualizes the architecture of the software stack running on the robot. The main part is the driver which updates the data of the hardware controllers via SPI and stores them inside of the RobotHW interface. In addition controller manager spawns muscle controller threads which calculate the individual control parameters for each muscle.

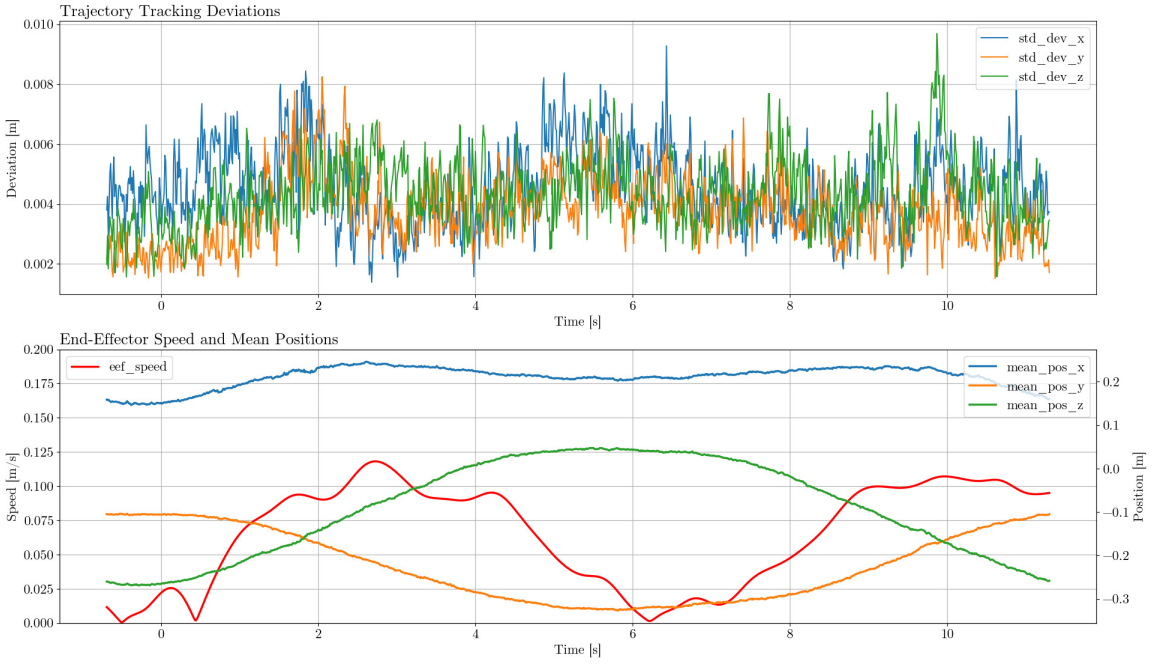

Trajectory (a)

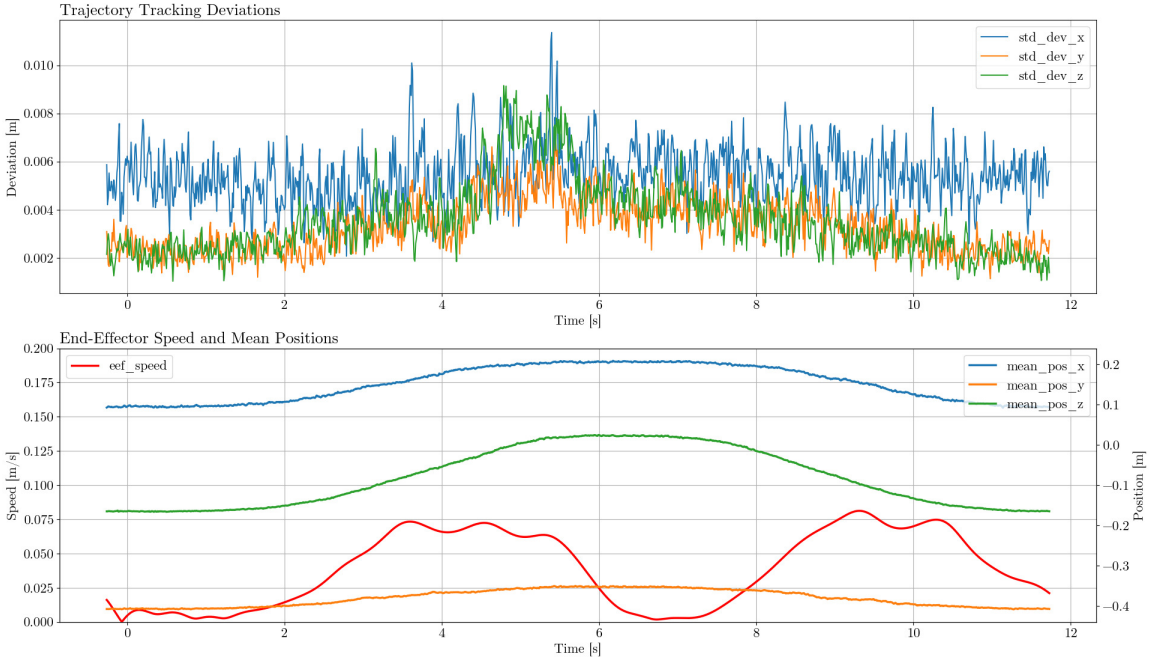

Trajectory (b)

Figure 2.7: The two plots above are visualizing the tracking results of individual trajectories over all 13 repetitions. It can be seen that the repetition is done by the robot with a standard deviation of 8mm. Further does it indicate that the spatial speed of the end-effector was 6-12cm/s.

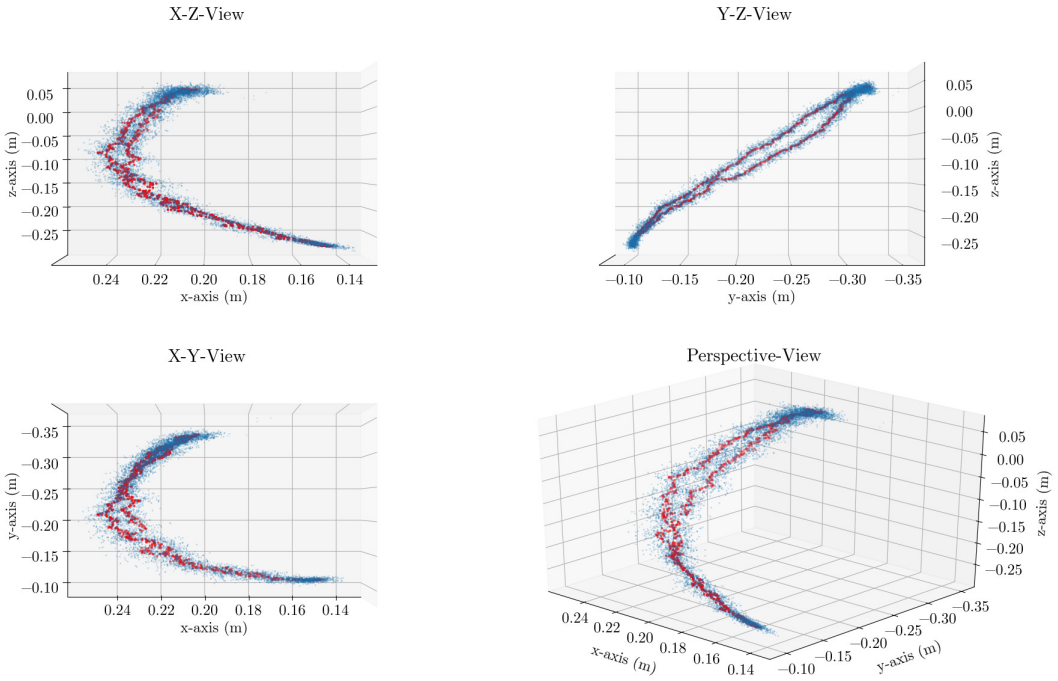

Trajectory (a)

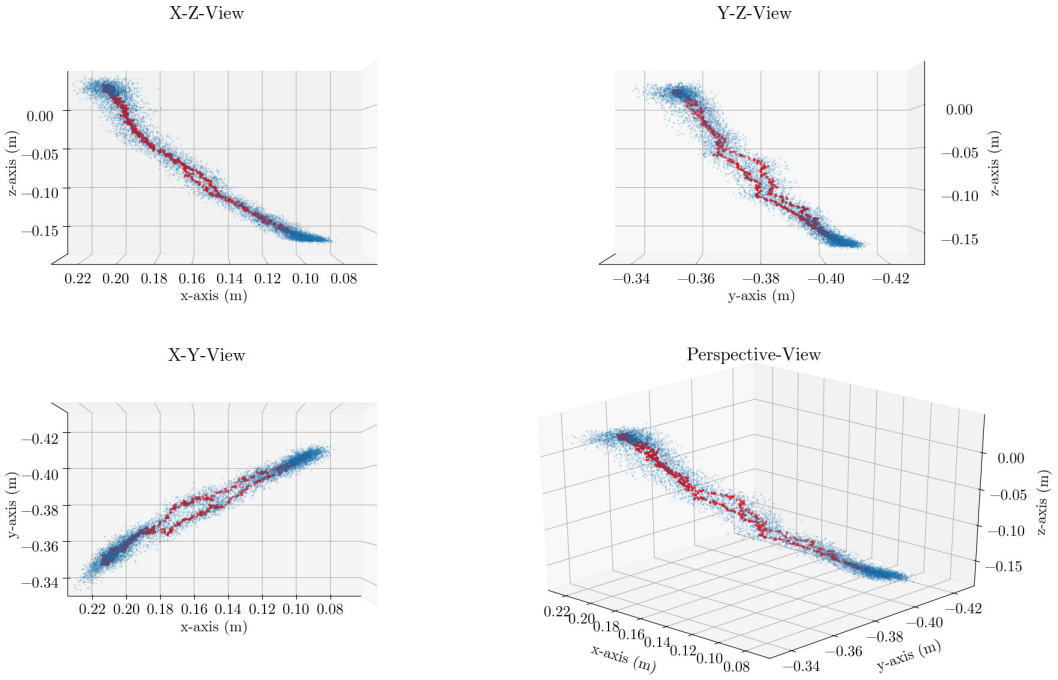

Trajectory (b)

Figure 2.8: The scatter plots show the tracking data during the repetitions of the trajectory (blue) and their mean values (red). The divergence of the average paths illustrates that the initial and final state of a trajectory influences its specific form by factors like flexibility and internal friction due to different initial pressures.

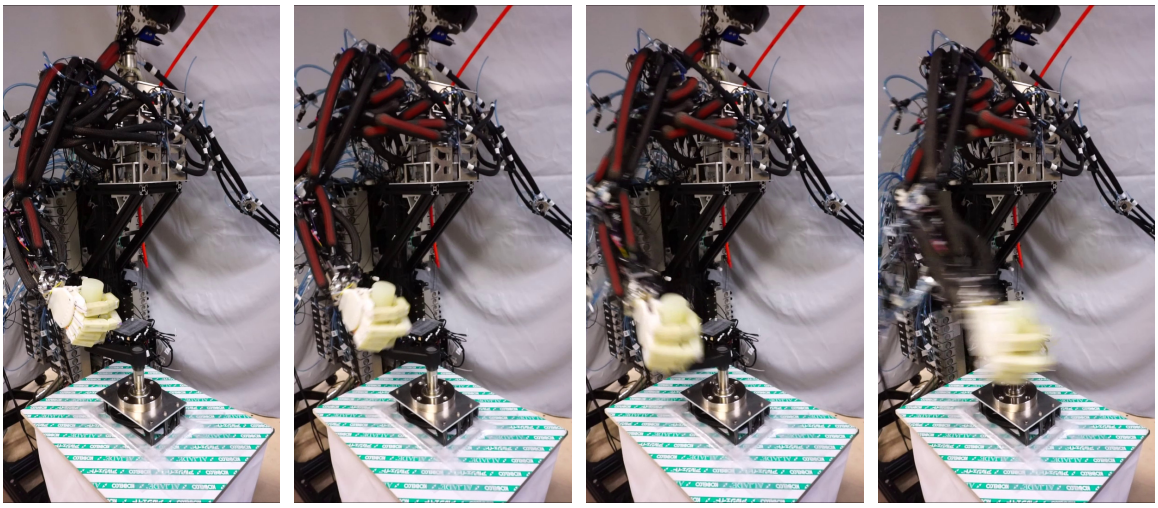

(1-1) (1-2) (1-3) (1-4)

Figure 2.9: The images above visualize the first half of the crank rotation experiment. In the beginning the robot is building up force and also lifts its should to allow an outwards rotation of the elbow by which the rotation starts. The activated muscles are marked red for illustrating the control pattern.

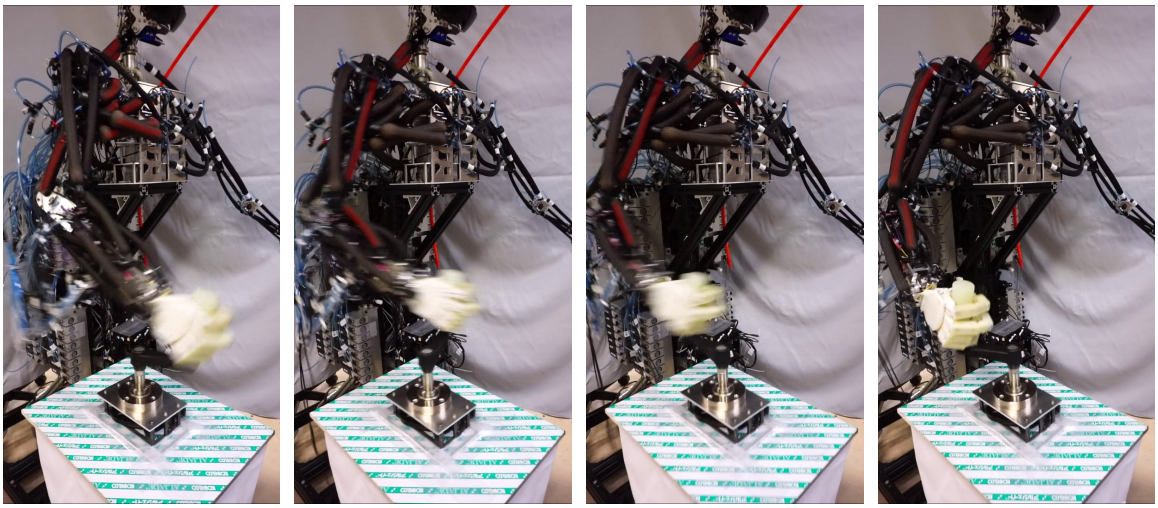

(2-1) (2-2) (2-3) (2-4)

Figure 2.10: In this sequence of images the robot is completing a rotation of the crank by contracting the red marked muscles.

Chapter 3

Highly-Integrated Muscle-Spindles for Pneumatic Artificial Muscles Made from Conductive Fabrics

3.1 Introduction

Research in bio-inspired humanoid robots and biomimetics is recently drawing an increasing amount of attention. One field beside the simple replication of the human morphology is its actuation using artificial muscles. The McKibben design of pneumatic artificial muscles (PAMs) is broadly used for this purpose.

They show properties like fast response and are flexible by design. Using them to actuate a human-inspired robot can help to increase the capabilities of bio-inspired robots, as well as the understanding of the human body. One downside of this type of actuator is its low control precision. A typical approach, therefore, is to estimate the current length of the actuator and to control it through the applied pressure. Unfortunately is the relationship between pressure and length non-linear and highly dependent on factors like externally applied lateral forces, and internal properties like friction.

This problem was approached by introducing a new version of an artificial muscle spindle, which can be embedded into the PAM. This was achieved by using conductive fabrics, which were applied directly to the inner tube of the PAM. Therefore a change in dynamic properties like stiffness and flexibility could be avoided.

3.1.1 Related Work

This work relates to previous efforts of researchers to increase the precision, and therefore, the usability of PAMs. This paper is introducing a hardware extension to traditional PAMs, which closely oriented on its biological counterpart. The following paragraph lists research, which relates to the aim of adapting muscle spindles to PAMs.

Hardware Jaax et al. [29] concentrated their efforts on creating a prototype of an artificial muscle spindle, without embedding it into a PAM. In their published design for an artificial muscle spindle, Erin et al. [13] proposed a PAM which is covered with a mesh of copper wire held in place by silicone. Their design allowed to estimate the muscle's displacement based on the inductance of the coil formed by the copper wire. A shape-memory alloy was used by Peng et al. [58] To measure the length of a PAM when it exerts a specific force. Hannaford et al. [20] published a platform to research human neural control. They described their setup to control PAMs by approaches inspired by motor units. However, it did not include the feedback of physically represented muscle spindles.

Contributions The results and methodology of this work can aid the research of human muscle control and coordination on the lowest level. A broader understanding in this area in combination with seamlessly embedded sensory-feedback can drastically increase in the motoric abilities of PAM-actuated robots.

3.2 Neurophysiological Background of Muscle Spindles

In the following section, the sensory-feedback system will be introduced, which is described in the literature as muscle spindles. This introduction will explain why this type of receptor should be considered to be of high potential to advance the capabilities of PAMs in musculoskeletal robots. Further, will this form the foundation of the reasoning regarding the physical properties the artificial muscle spindle was designed for.

The biological muscle spindle consists of two different kinds of sensing neurons. Fig. 3.1 visualizes the structure and the placement of the two neurons within the muscle.

The muscle spindle provides the input for the motor-units, which are essential for the muscles to maintain a specific length, as well as the cooperation of antagonistic muscles. To achieve this the two afferent neurons, which the muscle spindle consists of, modulate their firing rate based on two aspects of the muscle's state. The Ia afferent neuron is wrapped around the nuclear chain fiber and detects small changes of the muscle's inflation. Its firing rate hereby depends on the change rate of the muscle's inflation. The II afferent neuron, however, changes its firing rate regarding the sustained inflation of the muscle. Further, do the γ efferent neurons moderate the excitability of the Ia and the II afferent neurons.

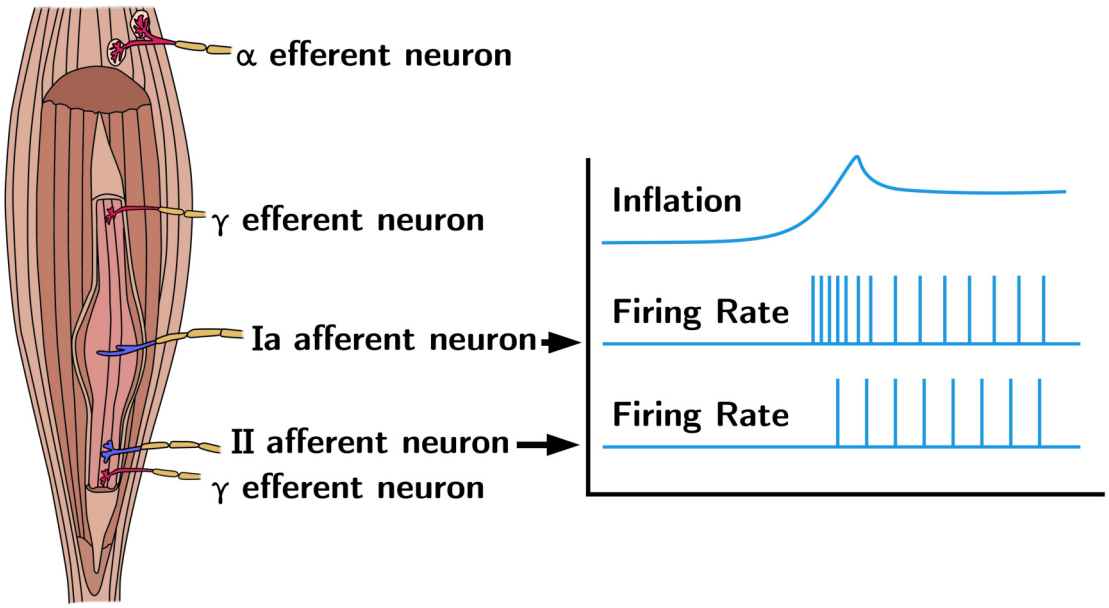

Figure 3.1: This image shows the representation of the biological muscle spindle (Inspired by Purves [62]). On the right side the response to inflation of the Ia and II afferent neurons is also visualized. This is the feedback that allows the motor-units to effectively control the and maintain the length of muscles.

3.3 Artificial Muscle Spindle

3.3.1 Concept

The vital information for the realization of a bio-inspired motor-unit is sensory-feedback of the muscles. In human anatomy, several receptors are responsible for this. Most notable are the muscle spindles and the Golgi tendon organs, whereby the latter is more involved in preventing over-stressing, and the first one supports the maintenance of the muscles' length. Therefore, the muscle spindles were chosen as the most desirable source of feedback to implement a more dexterous control scheme for PAMs. The biggest challenge was the choice of material for the artificial muscle spindle's Ia and II afferent neuron. The design described in this paper was defined after the following design requirements:

- can be embedded into the PAM
- fast response
- simplicity of measurements

- not causing the muscle to fail prematurely
- not changing the elasticity of the muscle

Other researchers already published several designs of artificial muscle spindles; however, they either could not be embedded, needed additional circuitry to be read or even reduced the durability of the PAMs. The design concept of this work's artificial muscle spindle is shown in Fig. 3.2.

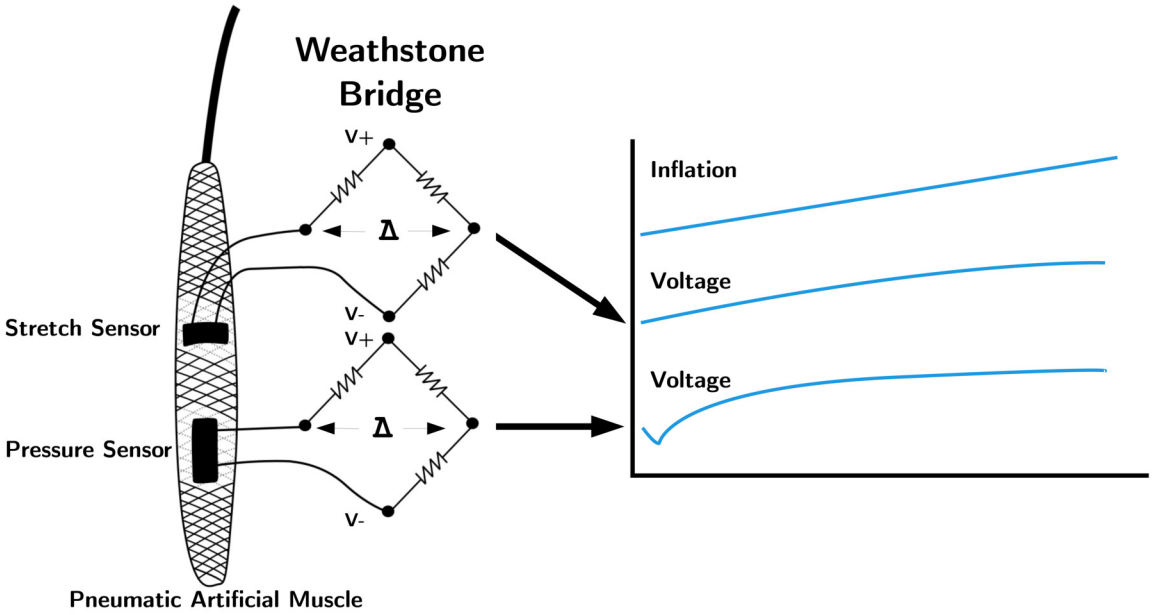

Figure 3.2: This image shows the functional concept of the design for an artificial muscle spindle. Two sensors made from conductive fabrics are placed in similar locations on the PAM as their biological counterparts are on a muscle fiber.

The design integrates the Ia and II afferent neuron by placing two different kinds of conductive fabrics in-between the inner rubber tube and the outer braided sleeve of the PAM. The type which represents the Ia afferent neuron changes its resistance when it is stretched. It is positioned in the middle of the muscle and is partially wrapped around it. The second sensor which represents the II afferent neuron, is made from a piezoresistive fabric and changes its resistance under pressure.

The choice of two different fabrics was made so the stretch of an unpressured PAM can be detected as well. The stretch sensor alone is not capable of measuring this reliable, as the diameter of the PAM decreases and no stretching takes place. The pressure sensor, on the other hand, can easily detect the change of pressure in-between the rubber tube and the braided sleeve when an external force stretches an empty muscle.

The design recreates the structure of the biological muscle spindle in regards to the measured

properties and the placement of the sensing elements within the muscle. However, the outputs of the afferent neurons in biological muscle spindles are signals in the form of spikes. The outputs of the artificial muscle spindle are continuous voltages. Further does the II afferent neuron represents the steadiness of the muscle's inflation. The artificial muscle spindle utilizes this element to measure the stretching of an unpressurized muscle.

With this setup, both outputs can be reproduced, which biological muscle spindles provide to the motor-units. Theoretically, only the version of the Ia afferent neuron would be sufficient. Because the sustained level of the stretch can be directly derived as the rate of change. The version of the II afferent neuron is therefore not needed for its biological purpose, but in an PAM it can provide data of an unpressurized muscle.

3.3.2 Components

To comply with the requirements which were defined in the concept section, the selection of materials were initially lead to a specific direction. External mechanisms were not feasible, due to their size and inevitable change of the muscles dimensions. Therefore a possibility was investigated to integrate the sensor in-between of the inner tube and the outer braided sleeve of the PAM. Using the work of Erin et al. [13] as a starting point, finding a way to preserve the original flexibility of PAM was focused on. It was found that the usage of conductive fabrics would allow this. The components, which were finally used for the artificial muscle spindle shown in Fig. 3.3.

Using two different types of conductive fabrics and directly attach them to the inner rubber tube of the PAMs, was found to be the most viable solution. The used fabrics change their resistance by stretch (EeonTex LTT-SLPA-20K) and pressure (EeonTex NW170-SLPA-2k). Small stripes of these materials are placed similar to their locations inside of real muscles. The stretch-sensitive fabric wraps around the middle part of the muscle and recreates the feedback of the Ia afferent neuron, while the pressure-sensitive material is placed longitudinally in the lower third of the muscle. Two magnet wires are glued to the fabric with conductive adhesive, which cures at room temperature (KAKEN TECH CN-7120). These wires are fed into a Wheatstone bridge to measure their resistance. The change in resistance causes a difference in measurements of up to 1.7 V using a 5 V reference voltage. Fig. 3.4 illustrates the response time and the slew rate of the artificial muscle spindle.

It can be noticed that the response to a change in pressure reaches the threshold of 50 mV distributed over the complete pressure range of the muscle within 10 ms. The underlying electronics of the system samples the air pressure and voltages of the artificial muscle spindle at 100 Hz. The threshold of 50 mV was selected by evaluating the signals' noise. During this process, the noise was measured for 50 intermediate pressures between 0.0 MPa and 0.85 MPa. The pressure sensitive fabric showed no significant change in resistance when low pressures were applied. This can be explained by the fact that the outer sleeve is about 4 mm wider in diameter, and some inflation of the rubber tube has to take place before the material makes contact with the sleeve to register

Figure 3.3: The images above display the materials, which were finally used for the artificial muscle spindle. Image *a* shows the conductive fabrics, and *b* the inner tube made of rubber as well as the outer braided sleeve. In image *c* magnet wire is shown and *d* shows the conductive adhesive that was used.

pressure. This property, however, was later found to be useful to detect external stretching of the relaxed muscle. In this case, the sleeve and the inner tube are pressed together by the external force and hereby can be measured.

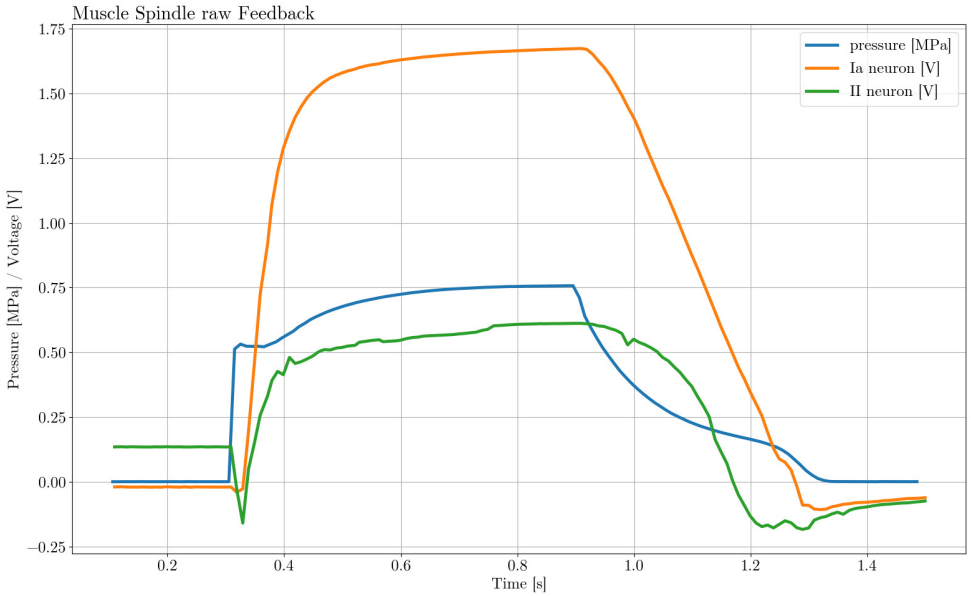

Figure 3.4: The diagram above visualizes the feedback of the artificial muscle spindle. It further shows the response to a change in pressure. For this sample the valve was opened without ramping, which resulted in a response within 10 ms.

3.3.3 Assembly

In this paragraph, the manufacturing process of the artificial muscle spindle will be described. Fig. 3.5 shows the four most important steps of the process.

Preparing the Fabrics: The first step includes the connection of the two different fabrics *EeonTex LTT-SLPA-20K* and *EeonTex NW170-SLPA-2k* with the magnet wires. Creating a conductive and robust connection between these two different materials was one of the most significant issues. For this work, a conductive adhesive is used, that cures at room temperature *KAKEN TECH CN-7120* and therefore does not damage the fabrics through typical curing temperatures around 70°C to 90°C. Using this adhesive, the magnet wires are first sew-in into the fabrics and then secured into place using the conductive compound. A finished sensor of the stretch-type can be seen in Fig. 3.5 on the upper left image (*a*).

Attaching the sensors: The second step is designated to fix the two individual sensors onto the rubber tube, so they stay in place during the assembly. After the assembly, the sensors stay in place due to the contact between the inner tube and the outer sleeve. However, having long wires attached to very light pieces of fabric exacerbate their handling. Therefore, the two sensors get fixed on one side before the insertion into the outer sleeve. For this step, *UHU Max Repair extreme* was

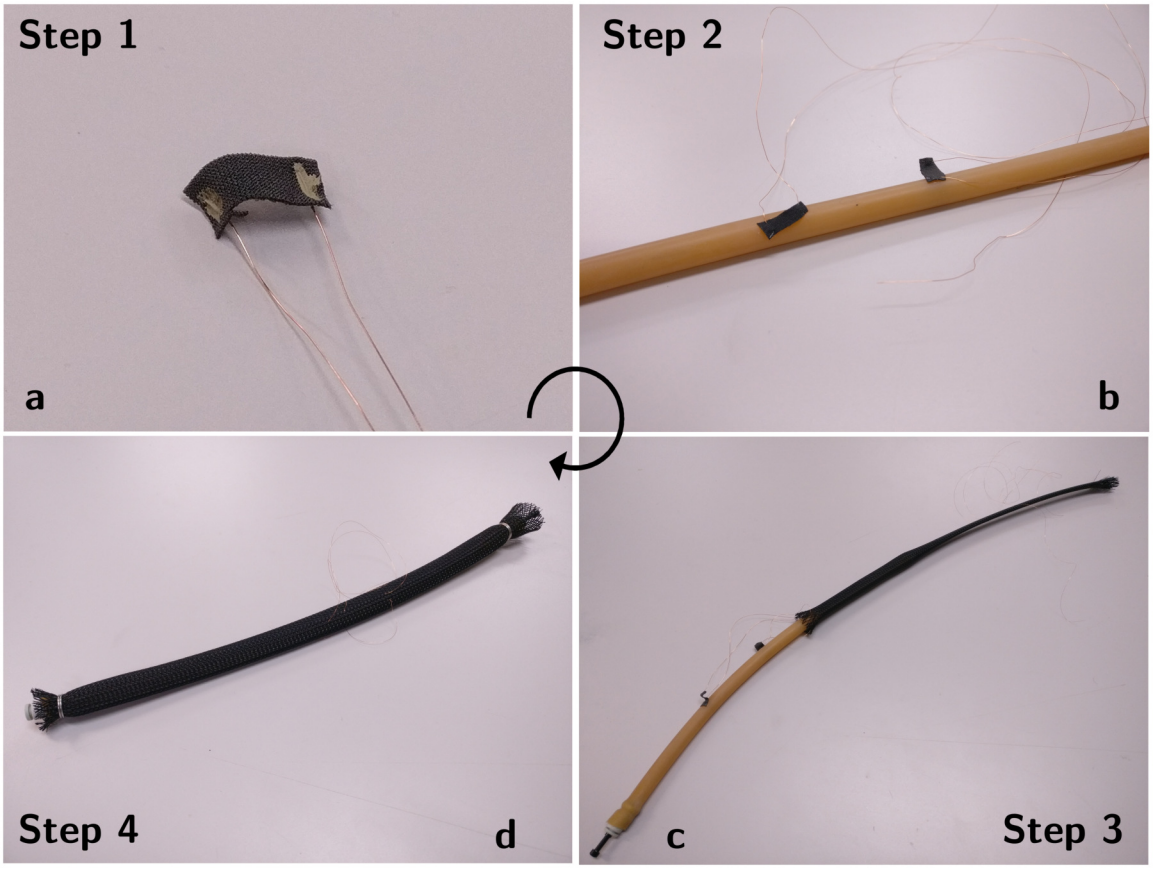

Figure 3.5: Image *a* shows the magnet wire sewn-in and fixed with conductive adhesive. Image *b* shows the fabrics and wires being fixed as lightly as possible on one side to the rubber tube. Image *c* shows the tube plugged both sides and the wires already threaded through the sleeve at their final position. Image *d* shows the finished assembly of the muscle.

used. Any adhesive, which does not degrade the rubber is usable for this purpose. The position of the sensors can be seen in Fig. 3.5 on the upper right image.

Preparing the insertion: To be able to insert the inner tube into the sleeve the wires need to be organized in advance. This step can be seen in Fig. 3.5 on the lower right image. During this step, the plugs at both ends of the tube are inserted as well. This step is essential to decrease the twisting of the wires in the finished muscle. Therefore, the wires are threaded through the outer sleeve before the insertion.

Finalizing the muscle: In the last step, the rubber tube is slide into the braided sleeve, while the wires need to be kept on minimal tension to avoid the creation of loops. The muscles are then finalized by sealing the ends using metal wires as it can be seen in the lower left image of Fig. 3.5.

3.4 Evaluation

In this section, two essential aspects of the design's properties will be emphasized. The first important trait is the longevity of the assembly. Therefore several muscles $N = 10$ were tested and repeatedly pressurized to estimate the average lifetime under full load. The second characteristic is the stability of the muscle spindle's output.

3.4.1 Longevity

A primary design goal was the preservation of the PAM's durability; therefore, multiple endurance tests with these actuators were conducted. The PAMs were repeatedly contracted using a pressure of 0.85 MPa, during these tests. Of specific interest was the PAM's tendency to rupture, as well as the possible breakage of the magnet wires, which connect the fabrics to the Wheatstone bridge. It was found that out of the sample group $N = 10$, no actuator ruptured during 300 individual contractions. This fact validated the choice of adhesives as they did not weaken the inner rubber tube of the PAM. The magnet wires (0.15 mm diameter) however, showed increased sensitivity to fatigue breakage. This issue needs to be addressed in future revisions of the design.

3.4.2 Stability of Measurements

The visualizations in this section will illustrate the margin of variance of the spindles' output when actuated repeatedly. This data was generated by continuously actuating the PAMs with a constant airflow and recording their feedback. The actuation was repeated 30 times. It could be observed that once a set of repetitions were started, it took around 3 activations for the feedback to settle in a closer margin of variance. This warm-up period contributes significantly to the extent of the minimum and maximum values, which are shown in Fig. 3.6 and Fig. 3.7.

The evaluation of the Ia neuron shows a non-linear relationship between the pressure and its feedback. However, the stretchable fabric is sufficient to cover the whole actuation range of the PAM.

Like the Ia neuron did the II neuron show a non-linear relationship to the pressure of the PAM it was embedded into, as well as being able to cover the PAM's whole actuation range. For the piezoresistive fabric, the change in pressure shows an initial reduction of its output before it starts raising in a similar way to the Ia neuron. This can be explained by the free travel the inner tube of the PAM experiences due to the slight difference in diameter compared to the outer sleeve. Through this data, two analogies to biological muscles and their sensory feedback can be made. First, the design has a warm-up period once the muscles are activated from a cold state, till their feedback settles. Second, for the II afferent neuron to show predictable feedback, minimal pressure is needed to maintain firm contact in-between of the outer sleeve and the inner rubber tube of the PAM. This property can be interpreted as an analogy to the muscle tone of musculoskeletal systems.

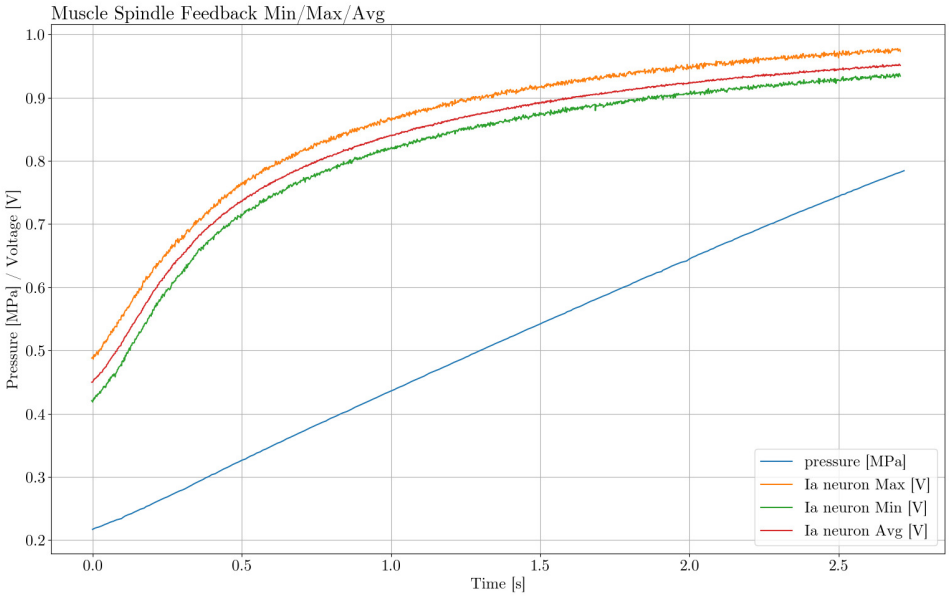

Figure 3.6: This illustration shows the stability of the feedback over 30 repetitions for the Ia afferent neuron from 0.22 MPa to 0.78 MPa.

3.5 Conclusion

3.5.1 Conclusion

In this paper, an augmented version of the McKibben design of PAMs was presented. By using conductive fabrics, a biomimetic approach to muscle spindles was created. The design allows for artificial sensory feedback of the Ia and II afferent neurons. The usage of fabrics and their positioning in-between of the braided sleeve and the PAM's inner tube caused no noticeable changes in the muscle's characteristics. This work demonstrated that the significant difference in resistance, and therefore, the output voltage of the spindle, renders this design robust to inductive interference. The combination of these traits makes this design very favorable for musculoskeletal setups with a focus on the realism of muscular sensory feedback.

3.5.2 Discussion

The artificial muscle spindle followed a biomimetic approach for its design. However, the output is not electronically converted into neuron-like firing patterns. This transform of the output needs to be done in software. The selection of materials was a result of the goal to embed the muscle

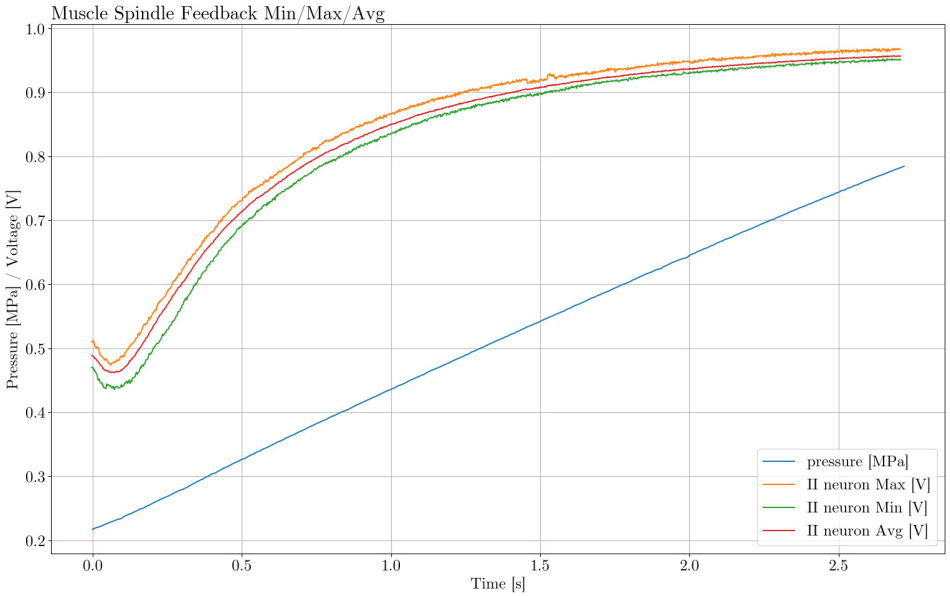

Figure 3.7: This illustration shows the stability of the feedback over 30 repetitions for the II afferent neuron from 0.22 MPa to 0.78 MPa.

spindle seamlessly into the PAM. Conductive fabrics allow the placement of the sensors directly in-between of the inner tube and the outer braided sleeve of the PAM. This does not only replicate their respective location in biological muscle spindles, but it is also favorable for not changing the PAM's flexibility as well as its dimensions.

Another important aspect is the correlation between the non-linear signal of the artificial muscle spindles and the change in length and diameter of the PAM. In Fig. 3.8 the change in length and diameter is visualized for an unloaded PAM from its unpressurized state up to 0.41 MPa. This data was collected by 40 intermediate measurements and the pressure was raised till the PAM stopped expanding.

It can be noted that the change in length and diameter is linear as soon as the inner rubber tube makes contact with the outer sleeve. This need for the inner tube's initial expansion explains the PAM's delayed response to pressurization. Based on this data we can assume that the non-linearity of the artificial muscle spindle's output is caused by the fabrics. However, it needs to be considered that all measurements were made with unloaded muscles.

The decision to integrate both afferent neurons (Ia and II) was based on this design's biomimetic approach. It was found, that the second sensor (II) is not necessary to produce a similar feedback to the biological muscle spindle. However, in this case the position, which was adopted from the II

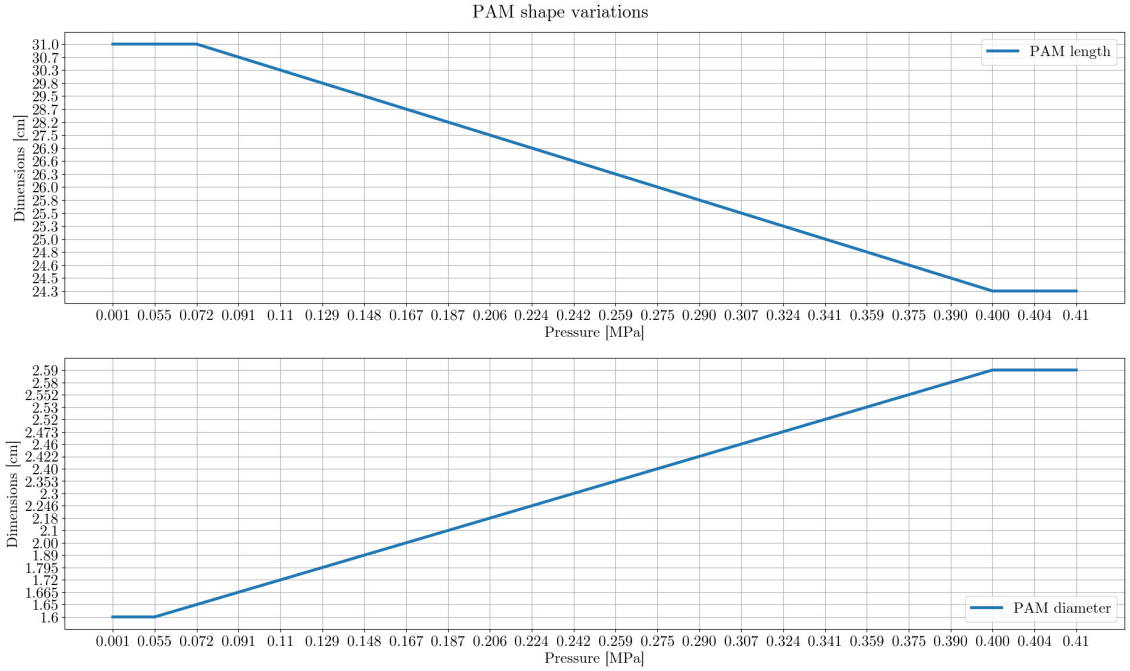

Figure 3.8: This diagram shows the change of a PAM's shape during pressurization. The diameter starts to increase faster than the length because the inner rubber tube first needs to expand to make firm contact with the outer sleeve.

afferent neuron, supported the measurement of an unpressurized PAM. This is possible due to the pressure between the inner tube and the outer braided sleeve when an external force stretches an unpressured PAM. This also justified the usage of a second type of conductive fabric. Positioning this sensor at the location of the II afferent neuron, further was tested to be highly effective.

3.5.3 Future Works

To allow a larger and more sophisticated robot, it would be advantageous to improve the embedding of the artificial muscle spindle further. The wiring of the current revision causes no problems in simple setups, but in a robot actuated with numerous PAMs, it will get convoluted quickly. Further development needs to be done to increase the longevity of the assembly. The current design focuses highly on its flexibility and the reduction of a mechanical impact to its hosting PAM. The adhesive connection between the wiring and the fabric was enhanced by choosing a conductive adhesive, which cures at low temperatures. However, the wires them-self, which are 0.15 mm in diameter, are exposed to strong forces in-between of the PAM's layers. This caused the current design to typically fail from fatigue breaks of the wires. Solving this issue, through adjustments in materials will be the primary focus of further improvements to the design. Once this issue is resolved, it is assumed

that the sensory-wise enhancement can provide a viable solution for complex musculoskeletal robotic systems.

Acknowledgment

This work was supported by JSPS KAKENHI Grant Numbers 16KT0015 and 17H05908.

Chapter 4

Using Conductive Fabrics as Inflation Sensors for Pneumatic Artificial Muscles

4.1 Introduction

Pneumatic artificial muscles (PAMs) utilizing the McKibben design have been widely used in soft robotics. Therefore, numerous previous approaches have been made to provide feedback for this non-linear type of actuator. Adding a sensory device to a flexible actuator presents many challenges, especially when considering the preservation of its distinguishing features, e.g. flexibility, compliance, and shape. In order to benefit from the potentials of PAMs, notably their compliance, relatively high dynamic, and force to size ratio [4], a variety of sensor designs were developed.

Considering the approach for measuring the actuator's deformation allows the previous research to be grouped into three types. Some designs used special materials for the PAM, which allowed for the measurement of deformation [66, 18, 57, 15, 22, 12, 72, 63]. Others attached components to the actuator, measuring the change externally [19, 35, 44]. The third type is inserting a sensor into the actuator to measure the increase of its diameter [2, 70].

It should be noted that previous sensors that preserve the flexibility and shape of PAMs are part of the actuator's structure, which prevents the usage with another actuator in case of its failure. However, the sensors that are transferable alter the dimensions and, to an extent, the flexibility of the actuator, which needs to be considered when routing the PAMs.

In this paper, we present the design of an external inflation sensor for PAMs that can be cost-efficiently produced and does not change the actuator's shape or flexibility due to the exclusive use of soft materials in the form of conductive fabrics. This allows for its usage in more complex and

dense systems, in which a deformation into a non-convex form or the addition of rigid components would significantly increase the friction with adjacent actuators. Our design addresses these issues, while also being easily transferable or replaceable in the event that either the actuator or sensor breaks.

Our application of the design presented in this paper is the usage in musculoskeletal systems with antagonistic muscle pairs like our upper ten degrees-of-freedom robot arm [24]. In such a setup, PAMs are in close proximity to each other and even in direct contact with adjacent PAMs, thereby generating constant friction. However, if the sensors of two adjacent muscles come into contact, their feedback would degrade due to the conductive nature of our sensors' surface. A system in which this problem would be likely to occur is a system like the UB Robot Hand [56] if its actuators would be switched from servomotors to PAMs. In such situations, additional precautions need to be taken. If the size constraints of the system do not allow for sufficient clearance in between sensors, the sensors themselves could be fitted with an additional insulating layer. Such a layer could be created using medical dressings as those are typically very flexible and therefore would only contribute to a small amount to the constraining of the actuator caused by the sensor. Having a small volumetric footprint and being flexible is highly important in such systems, so as to not introduce an additional friction hazard for the actuators. Therefore, producing the sensor separately so it can be transferred between various actuators of the same diameter is also highly desirable.

In section 4.3.2, we show our design's static response. The conductive fabrics we use have stretchable and less-stretchable directions, determined by the orientation of its weave. As both directions have different responses in regards to their electrical resistance, we evaluated the behavior of both orientations. Our evaluation of the hysteresis in section 4.3.4 further justifies our decision to make sensors with their fabric being oriented in the less-stretchable orientation. To evaluate our design's performance on a real PAM, we carried out a series of experiments in section 4.3.3 to show our sensor's feedback in different load-scenarios on PAMs of different diameters. To further reduce our sensor's production complexity, we compared the strength of two different adhesives to avoid sewing when creating the sensor. In section 4.2.3, we conducted breakage tests for seams formed from sewing to those created with adhesives.

4.2 Introduction of a Conductive Fabric Sensor

4.2.1 Sensor Design

Our design utilizes conductive fabric, which changes its resistance when stretched. The resistance of these fabrics is decreasing when stretched, which is contrary to a solid conductor. The resistance of a solid conductor equates to $R = p\frac{L}{A}$ where p is resistivity, L is the conductor's length, and A is the cross-sectional area. However, the situation of conductive knitted fabric is more complex. Li et al. [37] published a paper focused on the conductive characteristics of conductive yarn and fabrics

knitted from them. A solid conductor's resistance increases when elongated due to its increased length and simultaneous decrease of its cross-sectional area. Besides its length, the contact force of the fabric's loops and leads is a significant factor during the stretch. Therefore, when stretched, the yarn's contact force within the fabric increases, which results in an initial decrease in its resistance. Under larger tensile forces, the increasing length of the fabric will cause an increase in resistance before the material's breaking force is exceeded. However, besides this counterintuitive reaction to stretch, conductive fabrics' thin and flexible nature makes them very viable for our application. In our earlier paper [23], we presented an integrated design for such a sensor using conductive fabrics. As we concluded in that paper, the highest priority for an improved design was reducing the relatively high failure rate. Our new design addresses this issue, reduces the production complexity, and enables the simple replacement of the sensor.

Figure 4.1 illustrates an actuator equipped with our sensor.

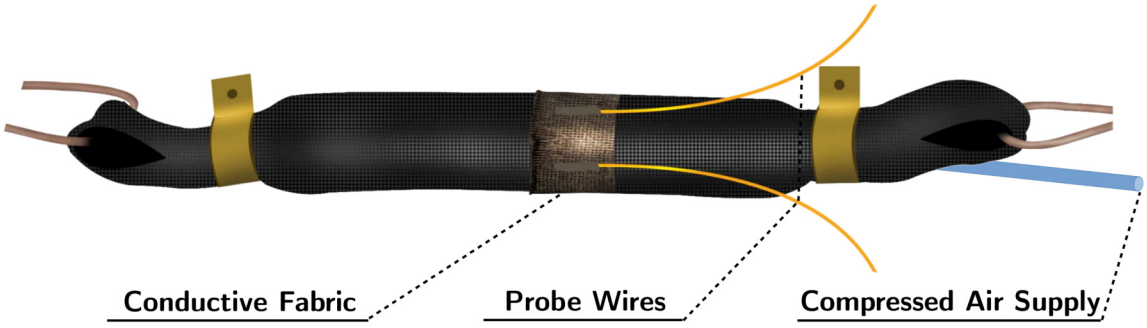

Figure 4.1: This illustration shows our inflation sensor attached to a pneumatic artificial muscle. The usage of conductive fabrics allow for no change in the actuator's shape or flexibility.

Instead of between the actuator's inner tube and outer sleeve, our design is wrapped around the PAM. This change heavily reduced the shearing stress in the wires and increased the sensor's longevity. Creating full sleeves instead of tying a small patch of fabric to the actuator further simplified the production process. Because the previous design's manufacturing process was laborious, the production and deployment was simplified. Another advantage that emerged was the possibility to retrofit our sensor to existing PAMs. Also, the weakest point in the earlier version is the magnet wire itself, which is now decoupled from the actuator's movements and is only subject to its external support's motions. Based on these changes, we can now present a sensor that requires no additional steps during the actuator's production and, therefore, can also be replaced if it is no longer required or needs maintenance.

In Figure 4.2, we show one of our actuators with a diameter of $10mm$ in its deflated and inflated state. When this actuator is pressurized with $0.7MPa$, it is reduced in length by $40mm$.

Figure 4.2: This image shows a pneumatic artificial muscle (PAM) in its deflated (a) and inflated (b) states. This actuator, with a diameter of $10mm$, shortens by $40mm$ when pressurized with $0.7MPa$.

4.2.2 Production Process

In this section, we will elaborate on the final production process of our design. Figure 4.3 illustrates the key steps during production. One of our sensors is created by the following steps. First, the conductive fabric is cut to the appropriate length for a given muscle circumference. Through empirical trials, we found that a well-performing length of *EeonTex LTT-SLPA-20K* is 5% shorter than the empty muscle's circumference plus $6mm$ for the bonding area. Next, an area of $3mm$ on one of the short edges is covered with adhesive before the fabric is folded, and the bonding area is clamped for curing. After the adhesive is cured, the now gauntlet-like sensor can be turned inside out, producing a smoother seam. In the next step, two magnet wires are prepared by removing the enamel with a soldering iron. This method leaves a rough surface on the wire, which makes the fixation in the next step easier than sanding off the enamel. The two wires are then stitched into the fabric, leaving a gap of $1cm$. While other gap sizes are possible, to allow for sensors with comparable feedback, the distance should be the same on all sensors. To secure the exposed ends of the magnet wires in the fabric, conductive adhesive that can cure at room temperature (*KAKEN TECH TK Paste CN-7120*) is then used to bond the magnet wires to the fabric. After the adhesive has cured, the sensor can be sheathed over the PAM. Due to being intentionally undersized, no additional measures are needed to secure the sensors on the PAM.

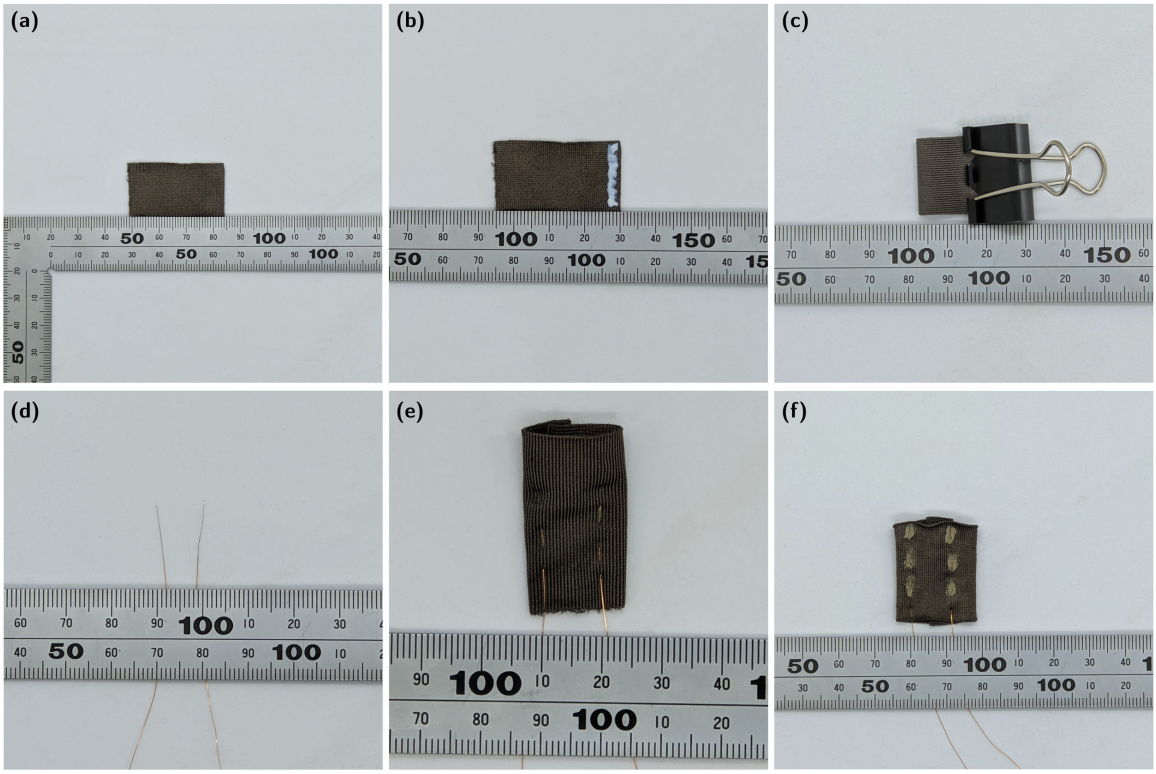

Figure 4.3: The selection of images above shows the most important steps of the production process. Image (a) shows the conductive fabric being cut to size, and with the appropriate amount of adhesive applied on image (b). The fabric is then clamped to produce a sleeve (c). The enamel of the magnet wire is removed, and solder is applied to its ending (d) before being sewn into the fabric (e). The final senor is shown in image (f) after the conductive adhesive was applied to secure the wires in place.

4.2.3 Material Selection

This section will introduce the individual characteristics of the two types of conductive fabric and adhesives we evaluated for our sensor design.

Conductive Fabrics

We selected two conductive fabrics that change their resistance when being stretched. The first one, *EeonTex LTT-SLPA-20K*, has a resistance around several $k\Omega$ over a distance of $1cm$. In contrast, the second fabric, *ElectroLycra*, has a resistance of less than 10Ω per centimeter. This fact required two different measurement approaches. The high resistance *EeonTex LTT-SLPA-20K* can be measured with a variable voltage divider, while *ElectroLycra* requires a constant current source to measure the voltage drop occurring based on its resistance. *EeonTex LTT-SLPA-20K* is a nylon/spandex

mixture coated with a proprietary conductive formula. *ElectroLycra* is a silver-plated mixture of nylon and other undisclosed elastic fibers.

Bonding Compound for Fabrics

As a minimal requirement of bonding strength for our seams, we considered an actuator's anticipated inflation under full pressure. The example of inflation shown in Figure 4.2 shows a PAM's inflation at $0.7MPa$. When our PAMs are pressurized, their diameter changes from $0.94cm$ to $1.90cm$, almost precisely an increase of 100%. Therefore, we know that our sensor is expected to stretch no more than double its length when using our actuators. Figure 4.4 illustrates the force a sensor experiences by stretching for a $1cm$ piece of fabric. Knowing that the test-stand moves with $0.8^{mm}/_{s}$, we expect the $1cm$ piece to be stretched by 100% within $12.5s$. The areas in Figure 4.4 highlight the stress the sensor experiences after $12.5s$. For *ElectroLycra* this is $15N$, and for *EeonTex LTT-SLPA-20K* this is $12.5N$. Based on this data, we determined that a bond must be able to withstand at least $15N$. Due to the materials' variance, the values are not absolute, but provide an appropriate reference point. However, as the break tests show, the adhesives satisfy this $15N$ requirement almost by a twofold. We also used break test data from tests with adhesives because the sewing of fabrics could possibly change the specimen's stretch characteristics. Therefore, we decided to use the data of tests with adhesives to ensure the stretch characteristics are comparable. In our experiments, we tested two adhesives against sewing for their interfabric bonding strength. We evaluated this by break testing all three bonding methods with both types of fabric. The test samples each consisted of two pieces of $1cm$ wide fabric, which were bonded over $5mm$ on each side. The specimen was then clamped into the motorized stand so that $1cm$ of fabric, including the seam, was between the clamps. In the next step, the stand separated the clamps at a speed of $0.8^{mm}/_{s}$ until the bond failed. The results are plotted in Figure 4.4.

From our evaluation, we concluded that, in general, for both fabrics, sewing will result in the strongest bond. Limited by our digital force gauge, we only measured the tensile force up to $50N$. However, during operation, the forces acting upon the bonds are expected to be considerably lower, as previously established. During our development of the production process, we identified that sewing together the sleeves is the most time-consuming, and, based on individual dexterity, variable part of the whole process. Therefore, we evaluated two adhesives designed for usage on fabrics. The first adhesive is *Loctite DNC-030* (*Adhesive I*), which consists of 50% urethane resin and water. The second adhesive is *Powerace A05* (*Adhesive II*), also using 50% urethane resin and 50% water. Even though both products use the same base component to create flexible bonds on fabrics, the different proprietary additives justified a comparison in our opinion.

Through our test, we found that both adhesives bond better with *EeonTex LTT-SLPA-20K* and that *Adhesive I* produces a stronger bond than *Adhesive II* with both fabrics. The best bond, following sewing, was achieved using *Adhesive I* on the *EeonTex LTT-SLPA-20K* fabric. For our

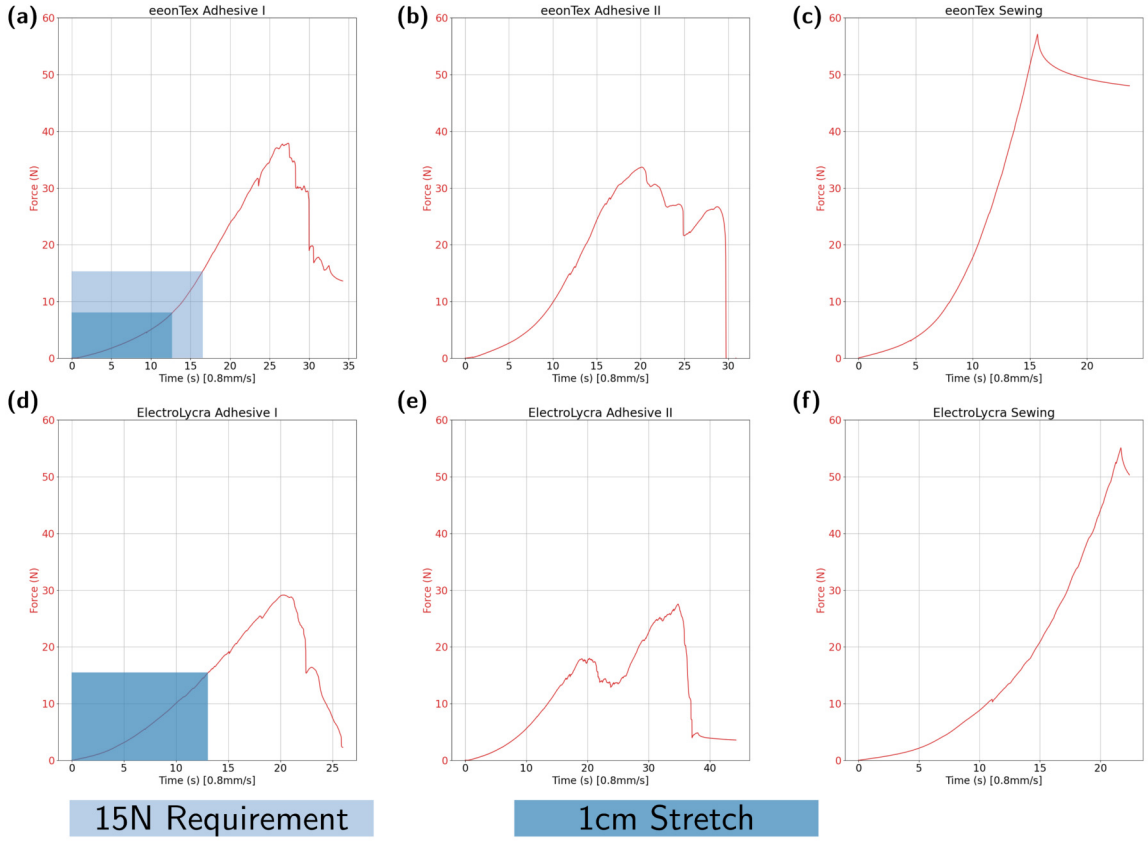

Figure 4.4: The plots above illustrate our evaluation of a suitable interfabric bonding solution. Two adhesives were tested against sewing the sleeves for both potential materials. The upper row, (a), (b), and (c), shows the tests on *eeonTex LTT-SLPA-20K*. The second row, (d), (e), and (f), shows the tests with *ElectroLycra*. They individually show the tensile force on the vertical axis and the time elapsed on the horizontal axis. For this experiment, the motorized stand was set to a speed of $0.8^{mm}/_{s}$. It can be observed that the adhesives generally bonded better with *eeonTex LTT-SLPA-20K*. Further, *Adhesive I* produced the best adhesive based bond with the eeonTex material. The significantly more labor-intensive production step of sewing, however, outperformed all adhesive/fabric combinations. We ended the sewing test at $50N$, due to the maximal load of our digital force gauge.

design, we decided to use *Adhesive I* over sewing due to its simple usability while meeting the demands in terms of tensile robustness. Throughout our later experiments, the seam formed by *Adhesive I* did not turn out to be a cause for the sensor to fail. This validated our decision to use *Adhesive I* to simplify the production process. Figure 4.5 (a & c) shows an opened sensor, so the seams created with the adhesive are visible. Evaluating the seams purely by the eye does not yield any remarkable difference. However, through our break tests, we could show that the bonds with the better performing adhesive are stronger on *EeonTex LTT-SLPA-20K*. Producing bonds

withstanding more than $25N$ with both fabrics validated the subsequent change of our production process from sewing to using an adhesive.

Bonding Compounds for Wires and Fabrics

Securing a conductive thread to a conductive fabric can be done in multiple ways. In the realm of wearables, a common method is sewing in a conductive thread made of stainless steel. These threads, however, lack an insulated coating, which makes them harder to handle. In a more complex system, several actuators will be placed in close proximity to each other. In such a scenario, the separation of conductive threads could be challenging. This situation could be mitigated by insulating the conductive threads in an additional production step. If this is done using a sleeve, the wires will become stiffer and heavier and potentially cause additional problems. If the thread is insulted with a non-conductive coating, it is important to make sure that this coating does not wear off due to the constant bending. Magnet wires are coated with a resistant enamel.

For our design, we chose magnet wire. Their enamel coating reduces the potential of short circuits. However, due to their tendency for fatigue breakage, sewing them into the fabrics was not a viable option. Due to this tendency of copper wires to fatigue break, specific care needs to be taken to reduce the bending. This is fortunately possible due to the low weight of $0.15mm$ magnet wire. Therefore, we use a conductive adhesive to establish a conductive connection between fabric and wire. Most conductive adhesives have a high curing temperature of around $100°C$ for an extended amount of time. For our design, we chose *KAKEN TECH TK Paste CN-7120*, as it has sufficient conductive properties and does not required heating to cure. The heating process would have degraded or destroyed our fabrics. Typically, we measured resistances of 1Ω between the fabric and the magnet wire's junction to the adhesive. Compared with the typical resistance of the *EeonTex LTT-SLPA-20K*, this increase is negligible, but compared to the resistance of *ElectroLycra*, it does contribute significantly to the total resistance of the sensor. Regarding the longevity of the bond formed by *KAKEN TECH TK Paste CN-7120* between the magnet wire and the two types of fabrics, we experienced no case in which the bond was the cause of a malfunction. When inspecting the bond after some time in a working system, it did not appear to have deteriorated or become brittle. However, it can be observed in Figure 4.5 (b & d) that the bond with *EeonTex LTT-SLPA-20K* appears to be more uniform, as this fabric has a smoother surface than *ElectroLycra*. In practice, however, no qualitative difference between the bonds to the two fabrics could be observed. We decided to do no additional testing on the adhesive's bond strength due to its good bonding qualities. This decision was based on preliminary manual strength tests of the bond between magnet wire and fabric. During these tests, we bonded different diameters of magnet wire ($0.1mm$, $0.15mm$, and $0.2mm$) to *EeonTex LTT-SLPA-20K* and *ElectroLycra* using *KAKEN TECH TK Paste CN-7120*. After the bond had cured, we attempted to forcefully separate the magnet wire from the fabric by hand. During this manual process, the bond between the magnet wire and fabric withstood the

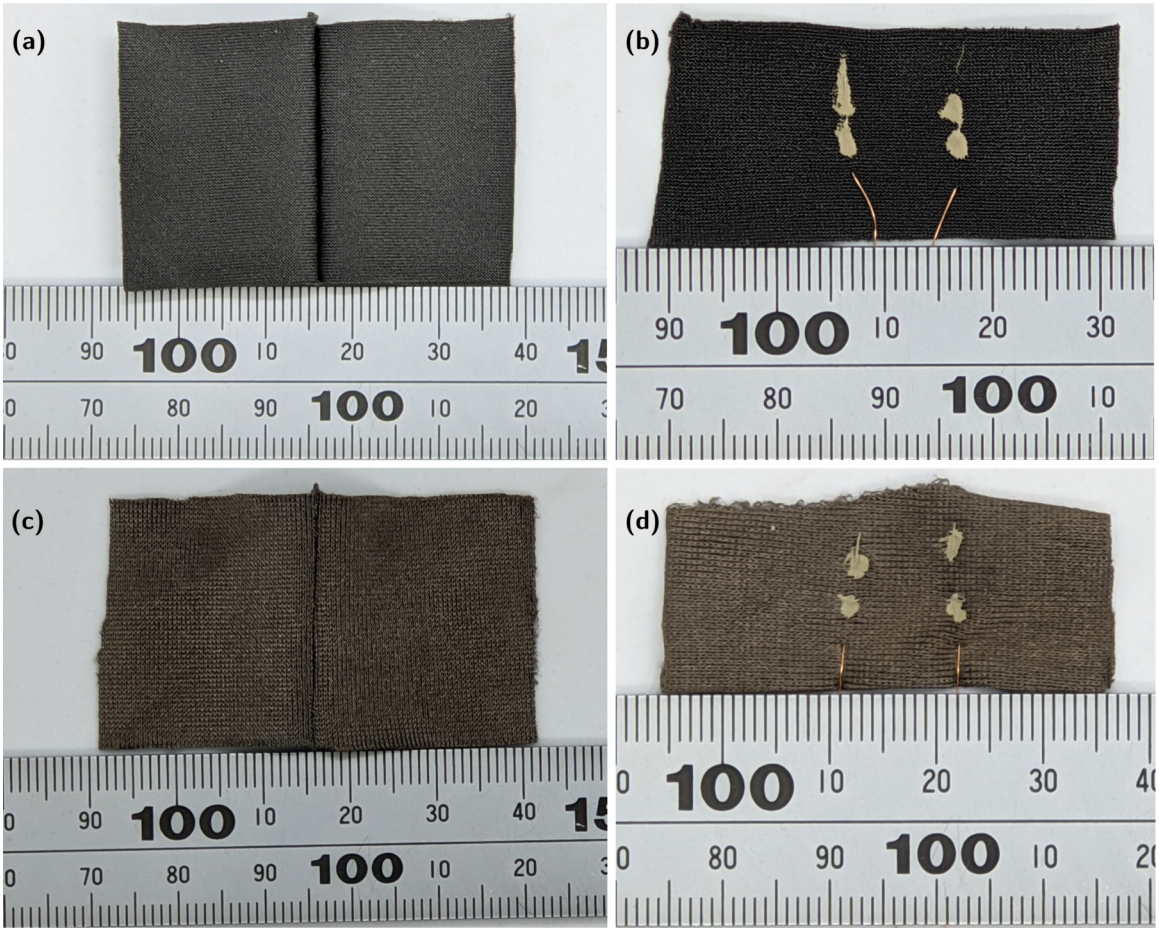

Figure 4.5: In this image, we present a detailed depiction of the quality of the adhesive seams for both fabrics and the wire to fabric bond for both materials. Images (a) and (b) show the bonds for *EeonTex LTT-SLPA-20K*, and images (c) and (d) show the bonds of *ElectroLycra*. It can be observed that the bonds of *EeonTex LTT-SLPA-20K* appear smoother, due to the denser weave of its fabric.

tensile force. The result was that the magnet wire itself broke before the adhesive failed. Based on these preliminary results, we concluded that the tensile strength of the wire we use is inferior to the bonds formed by using *KAKEN TECH TK Paste CN-7120*. Therefore, a break test of the bonds formed by the conductive adhesive is not needed, as it would only yield the tensile strength of generic magnet wires.

4.3 Experimentation and Evaluation

4.3.1 Experimental Setup

Our setup for *static testing* (Figure 4.6) is used to measure the change in resistance over displacement, as well as conducting the breaking test to evaluate the textile adhesives. We designed a dynamic testing rig for our experiments, which allows us to measure the length changes when variably loading the muscles. For our testing, we used the FGP-5 digital force gauge from Nidec Shimpo in combination with an FGS-50E-H motorized test stand from Shimpo and a DS-025 linear encoder from Mutoh. These components allowed us to precisely evaluate the change in resistance of the

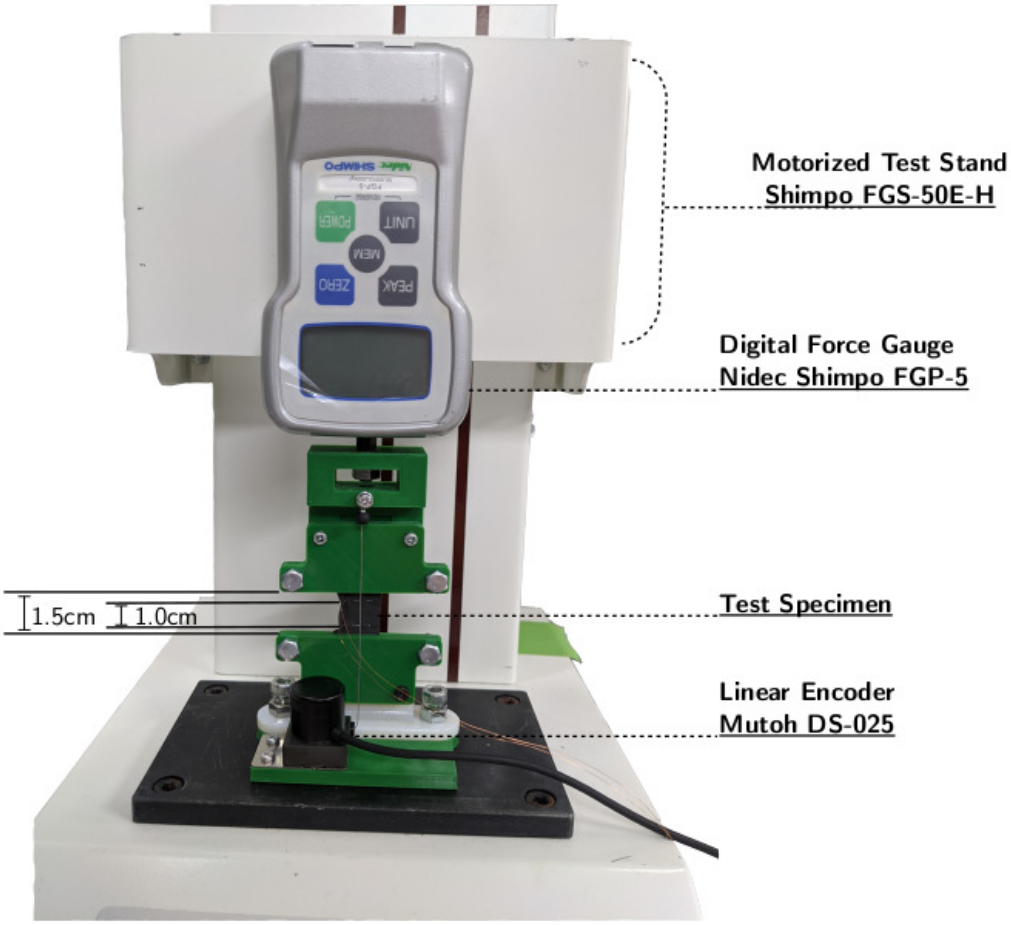

Figure 4.6: In the image above, we show the setup we used to measure the static behavior of our sensor. We used a motorized test stand, a force gauge, and a linear encoder to collect our data. This setup was later used for the break test in the course of the evaluation of bonding methods, as well as for the repeatability and stability tests of our design.

different materials as they are stretched. The motorized stand we used has no position encoder itself, therefore, we added a linear encoder externally. In addition, we designed custom brackets to fix the specimen in the test stand. Our design distributed the tensile force over a larger surface to avoid the tearing of individual fibers or an uneven application of the force.

In our *dynamic testing rig* (Figure 4.7), the PAM is placed on a stand, and a linear encoder with a guide roller allows the exact measurement of the change in length of the PAM. To evaluate the sensor's dynamic behavior, the rig also includes a deflection roller to load the muscle with varying weights. Experimenting with loaded muscles grants insight into the actuator's compliance.

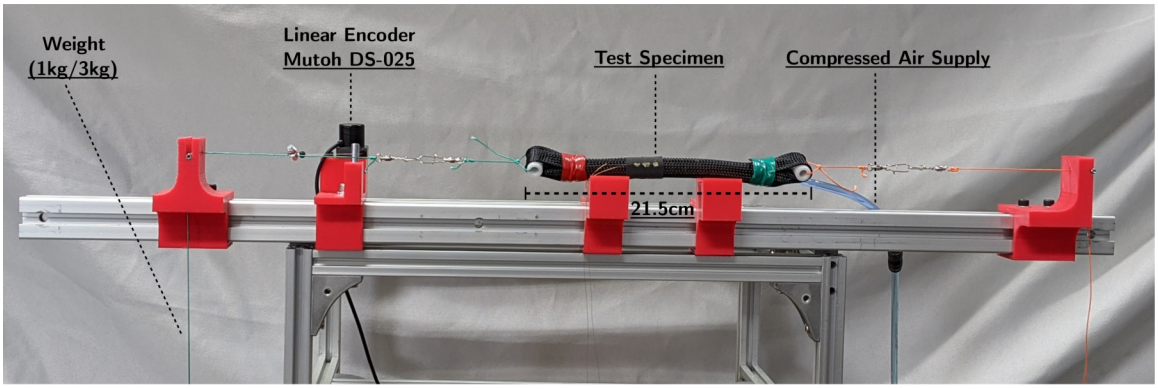

Figure 4.7: The image above shows our setup for the evaluation of the dynamic behavior of our sensor. All actuators used for our experiments had a length of 21.5cm. Once the specimen is connected to the system, the pressure and length are measured by a pressure sensor and a linear encoder.

Experimentation Protocol

We evaluated several different sets of muscles and sensors. Both materials were tested on two PAMs of varying diameters. This allowed us to infer that a constant performance on these diameters would indicate a general viability of this sensor type on PAMs of all sizes, as long as the inflation of the PAM does not exceed its stretch-capability. In detail, the data was collected in the following manner.

For measuring the static properties, a sample of fabric is fixed in the tensile tester. In a second step, the fabric was loaded with 0.1N of tensile force as a reference starting point. Then, the stretch was increased by 0.25mm and the resulting resistance was measured. The stretch then was increased by 0.25mm and the resistance was remeasured until 100% stretch was reached.

The dynamic properties are measured by first fixing the PAM (each of a length of 21.5cm) with the sensor in the testing rig. Then the pressure, length, and resistance feedback were measured for repetitive inflation in a sinusoidal waveform. The waveform was generated by the following

Table 4.1: This table lists the parameters we determined via polynomial regression, and the resulting functions are plotted in Figure 4.8. (1) are experiments conducted in the fabrics' less-stretchable direction, and (2) are those conducted in the fabrics' stretchable direction.

Setup	x^5	x^4	x^3	x^2	x	b
EeonTex (1)	8.534e-09	-1.421e-06	6.708e-05	0.0007744	-0.1557	13.39
EeonTex (2)	-8.203e-09	1.822e-06	-0.0001566	0.006596	-0.1293	8.189
ElectroLycra (1)	-2.367e-10	1.074e-07	-1.827e-05	0.001461	-0.06022	2.835
ElectroLycra (2)	5.275e-08	-8.868e-06	0.0005502	-0.01566	0.1941	3.598

expression, where t is the time in seconds and $pressure_{goal}(t)$ maps t to pressure in MPa:

$$\boldsymbol{pressure_{goal}(t) = \frac{\sin(2\pi \times (t-0.25))+1}{5}} \tag{4.1}$$

In this function, t is offset by -0.25 to center the pressure peaks within the three-peak plot. Lastly, we permute over all combinations of PAM diameters, sensor material, and loads.

4.3.2 Static Behavior

We evaluated the static characteristics of our two types of fabric to determine which would yield the best results for our application. The fabrics were tested using a $3cm$ by $1.5cm$ sample with a copper wire distance of $1.0cm$ and a clamp distance of $1.5cm$ (Figure 4.6). We further considered that the fabrics show different responses to stretch based on the direction of stretch in relation to its weave pattern. Therefore, we also sampled the fabrics in a 90° rotational offset. The results are plotted in Figure 4.8. During our tests, we pre-loaded the fabrics with $0.1N$ as a reference starting point. The $1.5cm$ portion of fabric was then stretched by $1.5cm$ to 100% stretching. Every $0.25mm$, the resistance was sampled.

In our evaluation, we found out that in the case of both fabrics, the less-stretchable direction produced a cleaner feedback (Figure 4.8). The more stretchable direction showed, in both cases, an initial indifference to stretch before the resistance starts changing significantly. *ElectroLycra* and *EeonTex LTT-SLPA-20K* showed a high sensitivity from the beginning of the stretch if it occurs perpendicular to its stretchable direction. We could also observe that even in the more favorable direction, the change in resistance due to stretch is non-linear. However, this was generally expected, even if less severe in the case of the *EeonTex LTT-SLPA-20K* fabric. Using MATLAB's system identification functionality, an order of five was estimated to be the most usable degree for modeling our sensor's feedback via polynomial regression. Based on the resulting polynomial regression, we modeled the response of the sensors during the experiments, which are shown along with the data points in Figure 4.8. The parameters of the resulting models are listed in Table 4.1. Due to the fabric's variance, the values will differ between individual sensors.

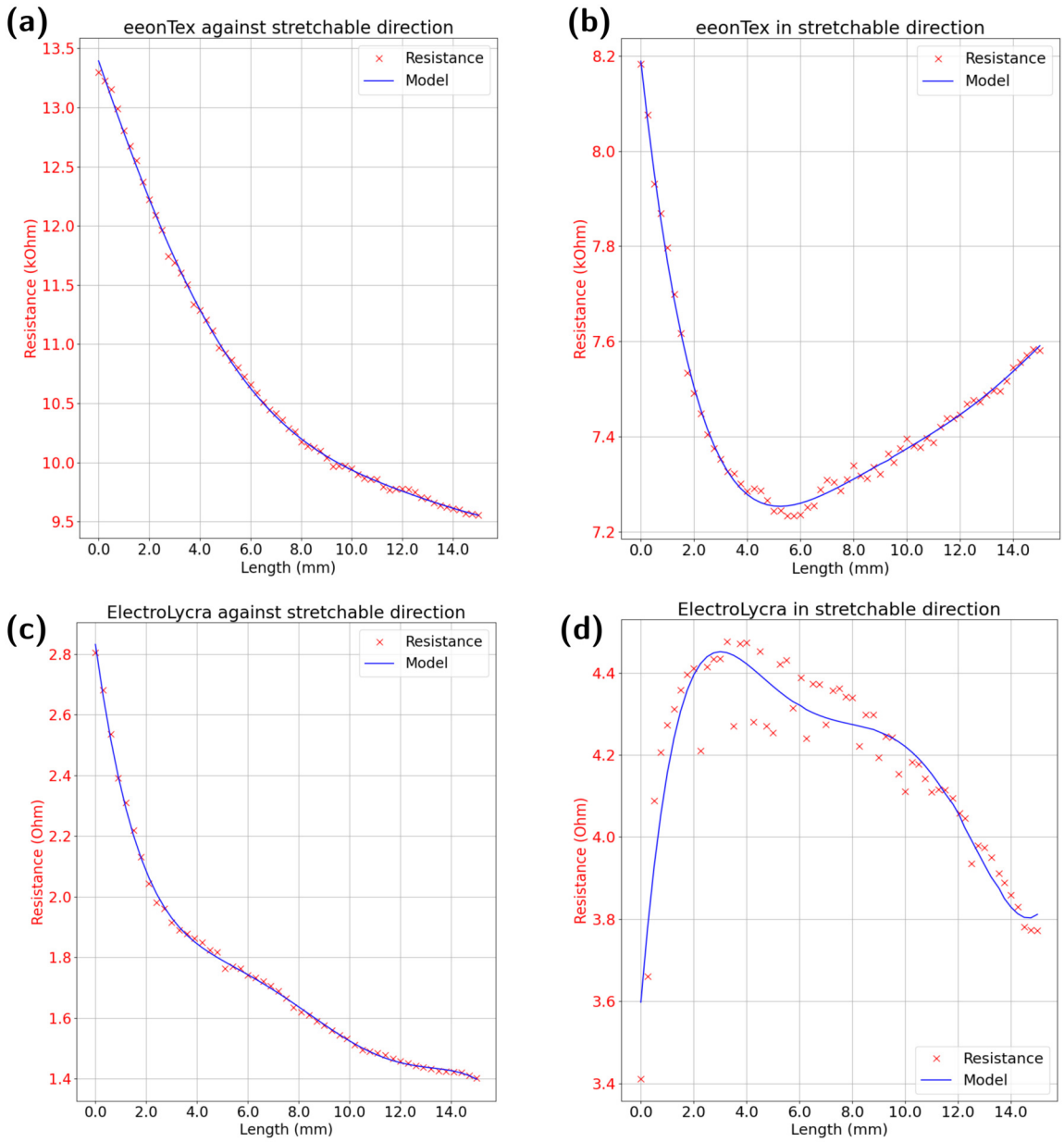

Figure 4.8: (a) shows the change of resistance of *eeonTex LTT-SLPA-20K* in the less-stretchable direction. (b) shows the change of resistance of *eeonTex LTT-SLPA-20K* in the stretchable direction of its weave. (c) shows the change of resistance of *ElectroLycra* in the less-stretchable direction. (d) shows the change of resistance of *ElectroLycra* in the stretchable direction of its weave. It can be noticed that for both fabrics the less-stretchable direction shows a cleaner, monotonic output.

4.3.3 Dynamic Behavior

Based on the evaluation of the static behavior, we decided that all sensors for the dynamic experiments will be manufactured so that the fabric is stretched in its less-stretchable direction. For better comparison, we grouped the results of our dynamic evaluation by the PAM's diameter. We used two different PAM sizes: $10mm$ and $15mm$. The data were filtered by a 2nd order low-pass Butterworth filter with a cutoff frequency of 30Hz. Those parameters rejected the switching noise of the supply voltage while conserving the imperfections of the feedback. The evaluation represents the change in resistance during the inflation of the actuator normalized by the lowest value measured during inflation. This is done to account for the potential variance in absolute values of individual sensors. In Figure 4.9, we compiled the results of the $15mm$ PAMs. Pressure and length are in an inverse relationship as the muscle shortens when pressurized. Comparing the two loads, we can observe that in the case of the *EeonTex LTT-SLPA-20K* based sensor, the lowest resistance, which is reached during full inflation, is reduced by $0.5k\Omega$, due to the stretching caused by the weight. This is similarly observable for the *ElectroLycra* based sensor, with a shift in resistance of 0.8Ω. To illustrate this shift, we prepared a comparison in Appendix 4.5.1 based on the individual tests' absolute feedback values. This illustration also shows through the shift that the absolute lengths for varying loads changes while the range of changes in length stays the same, as can be observed in Figure 4.9 & 4.10. Other than the shift in resistance, no further changes of the sensor's feedback, neither its response time nor its slew, can be assessed. Figure 4.10 shows our tests' results using a PAM of $10mm$ diameter. The first noticeable difference is the reduced peak-to-peak change in resistance due to the smaller absolute change in circumference and, therefore, the sensor's stretch. The second interesting difference is the lower impact of the load on the feedback. It might be deduced that a bigger PAM is easier to stretch by lateral force than a smaller PAM when exposed to the same internal pressure. The results also show that the length can not be precisely derived from the feedback due to slight variations in the sensor's positioning in combination with the high sensitivity of the sensor's material. Therefore, simply rotating the sensor on the muscle could cause a drift of its output. Another important finding from the dynamic experiments is the phenomenon which will from hereon be referred to as overstretch. In Figure 4.9 & 4.10, we marked the areas where this effect takes place, and we illustrate this in Appendix 4.5.2. By highlighting the figures of the dynamic experiments, we can define two states during the experiments. In the non-highlighted areas, our design presents a monotonic relation of the pressure and the length. In the highlighted areas, our sensor generates erratic non-monotonic feedback. This happens due to the actuator's overstretching caused by the load when the actuator gets completely deflated. In the description of the production process 4.2.2, we mentioned that the sensors' length was chosen to be 5% shorter than the deflated actuator's circumference. This allows the sensor to maintain its position and to have constant contact with the actuator. However, if the actuator gets loaded and deflated completely, the load's moment of inertia causes the actuator to stretch to a point where the sensor

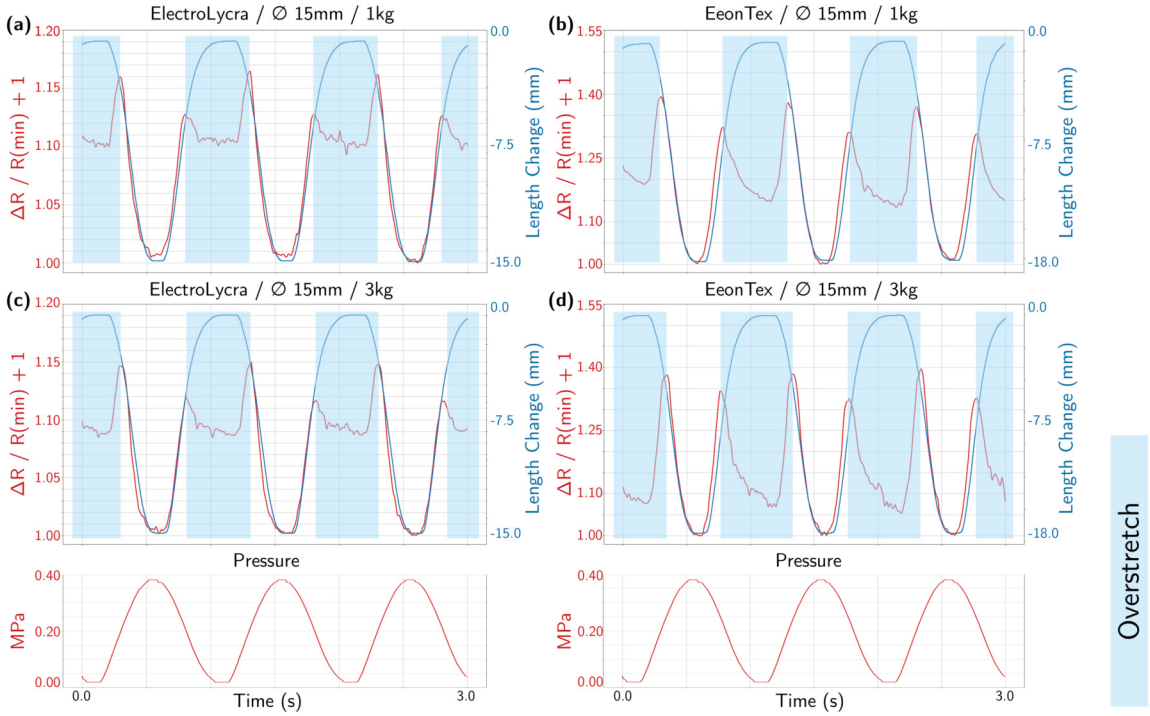

Figure 4.9: The plots above show the dynamic behavior of our sensors made from *eeonTex LTT-SLPA-20K* and *ElectroLycra*. The results were generated using PAMs with a diameter of 15*mm*, which were loaded with 1kg and 3kg. The transparent boxes mark the area in which the sensor loses contact with the actuator due to overstretching. This phenomenon is explained in Appendix 4.5.2.

loses contact with the actuator. When the sensor loses contact, its feedback becomes erratic and non-monotonic. This problem could be mitigated by further reducing the sensor's circumference in relation to the actuator's circumference. Another way to mitigate this effect would be the avoidance of total deflation of the muscle. As we stated in our introduction, we designed this sensor to be used in musculoskeletal systems with antagonistic muscle pairs. These systems require a minimal base pressure resulting in countering forces to stabilize their structure. This can be compared with the muscle tone of natural muscle systems. While the possibility of an actuator getting overstretched is a potential disadvantage, it can be mitigated.

4.3.4 Hysteresis

Hysteresis is a common phenomenon caused by the dependency of a sensor's current state based on its previous states. It is therefore important to measure this property for the materials of our sensor's design. To assess the extent of this, we used the motorized test stand for a continuous stretch and relax movement. The length was measured via a linear encoder in parallel to the sensor's resistance.

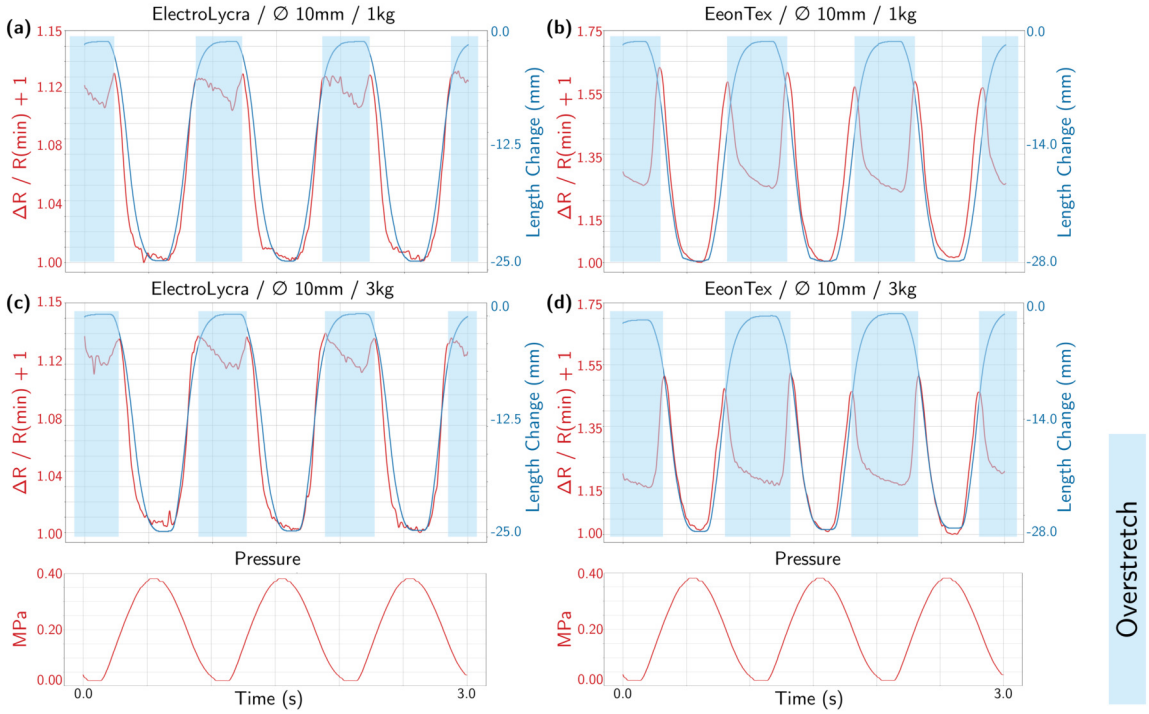

Figure 4.10: The plots above show the dynamic behavior of our sensors made from *eeonTex LTT-SLPA-20K* and *ElectroLycra*. This second set of trials used PAMs with a diameter of $10mm$ and the same two loads. The transparent boxes mark the area in which the sensor loses contact with the actuator due to overstretching. This phenomenon is explained in Appendix 4.5.2.

The data was collected at a rate of $950Hz$ and was not filtered. Based on the static results, we expected that both materials would perform better in their less-stretchable orientation. In Figure 4.11, we plotted the results of our tests. This illustration confirms our previous observations. It can be noted that (a) and (b), which show the results when the sensor is stretched against its stretchable direction, are also the most useful in regards to hysteresis. Contrary to this, we can see in (c) and (d) that the feedback follows a more non-linear trajectory.

4.4 Discussion and Conclusion

Our results show that our sensor's feedback in relation to the absolute length of the actuator does not perform as well as the linear encoder. This weak relationship could be explained by the combined non-linearity of the actuator itself and that of our sensor. The non-linear nature of PAMs represents a significant disadvantage of this type of actuation. Based on this, we can state that our sensor is less viable if the total length needs to be measured. However, if the application's goal is to maintain an arbitrary state of inflation and compensate for tensile forces, our sensor proved to be a viable

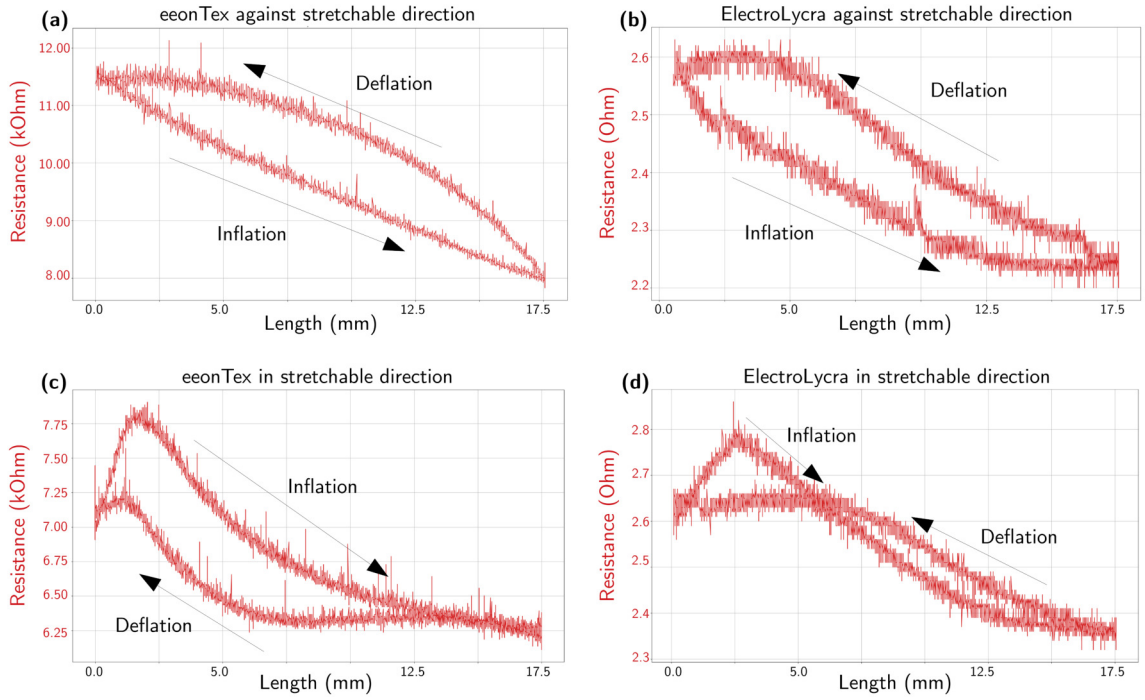

Figure 4.11: The image above shows the hysteresis we measured for the two materials. The plots (a) and (c) show the sensor's response for *eeonTex LTT-SLPA-20K* in its stretchable and less-stretchable orientations. In (b) and (d), the same experiments were conducted with sensors made from *ElectroLycra*.

solution.

We found that, when compared with the pressure feedback, the feedback of our sensor design is less expressive. Further, it could be assumed that our sensor's feedback might be redundant to the pressure feedback. However, as we could see in the dynamic testing results, a change in our sensor's feedback can be observed when the actuator is loaded with a different weight. In these situations, the pressure feedback remains constant, even when the change in length varies due to the load on the actuator. Having inflation feedback of each PAM can be used to group reciprocal muscles and create a control schema that compensates for external perturbations. Such a controller combined with an inverse kinematic could then execute loaded tasks in its environment. An example would be picking up a weight. In contrast, control schemes based on pressures can not detect and counteract forces that are exerted to the system externally. Interacting with the environment in an adaptable manner would be a great advancement for musculoskeletal systems using PAMs towards being practicable for broader usage in experiments where compliance and adaptability are desired. Further research on this design would include improving the production process in regards to tools and individual steps. Using adhesive already greatly reduced the build time per sensor, so we hope

to identify additional options to reduce the time required to build a sensor, as well as increasing their quality by reducing the influence of an individual's skill on the final sensor.

During the development of our sensor's final design, we also tested different locations for the sensor to be placed. However, we found that the most viable position is found in the middle of the actuator. This potentially is attributed to the way the actuator deforms when it is pressurized. In Figure 4.2, it can be noted that it creates a curvature towards the actuator's ends. Being placed over or near these areas would interfere with the uniformity of the sensor's deformation and could be detrimental to its performance. Therefore, we decided that in our design, the sensor should generally be placed in the middle of the actuator. Due to our sensor's work principle, which relies on the deformation through the actuator's inflation, it needs to be considered that the constraining force of the sensor reduces the actuator's peak tensile force. In practice this decrease is found to be 3.2% for *EeonTex LTT-SLPA-20K* and 3.6% for *ElectroLycra*. If this peak performance is critical in a system, then the dimensions of the actuators need to be adjusted when using our design.

An important aspect of stretchable fabrics is their loss of flexibility and, therefore, a change of their resistive characteristics. We, therefore, also evaluated the repeatability and stability of our sensor's feedback after 5000 stretching cycles. In Appendix 4.5.3 and 4.5.4, we included the results of our tests evaluating these properties. We found that sensors made from both materials generate repeatable feedback. In regards to their stability, however, the individual materials differ from each other. When assessing the hysteresis of *EeonTex LTT-SLPA-20K* after 1000 and 5000 cycles, the hysteresis stays stable in form and range. Therefore, a re-calibration is not expected to be necessary for sensors made from this material. Sensors made from *ElectroLycra*, however, show non-monotonic feedback between 1000 and 5000 cycles. The cause for this is expected to be a constant elongation of the material in the beginning of its usage. An option to mitigate this behavior could be to pre-stretch the material before assembling the sensor and thereby adjusting the size and guaranteeing the material's constant tension.

In this paper, we showed a novel design of an inflation sensor for PAMs. Throughout this paper, we showed that using off-the-shelf components can be used to create a responsive soft sensor. This soft nature is also its most significant disadvantage, as it is hard to generate absolute feedback for the current length of the actuator. As a result, we see the applications of this type of sensor in the area of soft robotics, where precision can be substituted by adaptability. In this area, musculoskeletal robots utilizing PAMs can benefit from our design. Firstly, it is easy to recreate and can also be retrofitted to existing PAMs, due to its external deployment. Secondly, its small size and low footprint on the PAM allow it to be placed in complex musculoskeletal systems, in which actuators can be routed in close proximity. Our evaluations demonstrate that our design provides repeatable results while being simple in design. Compared to earlier solutions, which we listed in the introduction, our design is smaller in dimension than previous external sensors. With this design, we hope to foster the research in musculoskeletal systems by offering an easy entry-point for non-pressure-based control attempts.

Acknowledgements

We thank Dr Shunsuke Shigaki and Mr Tsung-Yuan Chen for their valuable comments on visualizing our results.

Disclosure statement

No potential conflict of interest was reported by the authors.

4.5 Appendices

4.5.1 Output Shifting based on load

In the appendix, we will exemplify the shift in feedback our design generates when stressed with different loads. Figure 4.12 shows the plots of the absolute resistance values during the dynamic tests. Besides a noticeable increase in resistance between sensors for actuators of different circumferences, it can be observed that the resistance-range shifts when the actuator is loaded with different weights. Considering that the actuator's resistance is decreasing when stretched, the direction of the shift is expected. In the case of a higher load, the actuator will be stretched to a greater length during relaxation and will be prevented from entirely contracting when being pressurized. Compared to a more lightly loaded actuator, the feedback reaches a higher peak resistance due to the additional stretch and is restricted to a higher minimum value.

4.5.2 Overstretch

During our dynamic experiments, we noticed the phenomenon that the sensor generates non-monotonic feedback. We discovered that this was due to the actuator being stretched to a degree where the sensor loses contact. If this happens, the feedback becomes erratic and does not represent the actuator's current inflation state. A possibility of mitigation is to produce the sensor with a considerably smaller diameter than the deflated muscle or preventing the actuator from total deflation. Figure 4.13 illustrates this issue.

4.5.3 Repeatability of Hysteresis

In Figure 4.14, we show the hysteresis of our design when made from *EeonTex LTT-SLPA-20K* and *ElectroLycra* after 1000 and 5000 inflation cycles. This evaluation is meant to show the stability of our design. In both cases, the hysteresis does not change considerably in respect to its form and range. However, while the sensor made from *EeonTex LTT-SLPA-20K* retains its monotonic behavior, the sensor made from *ElectroLycra* starts to produce non-monotonic feedback. This is

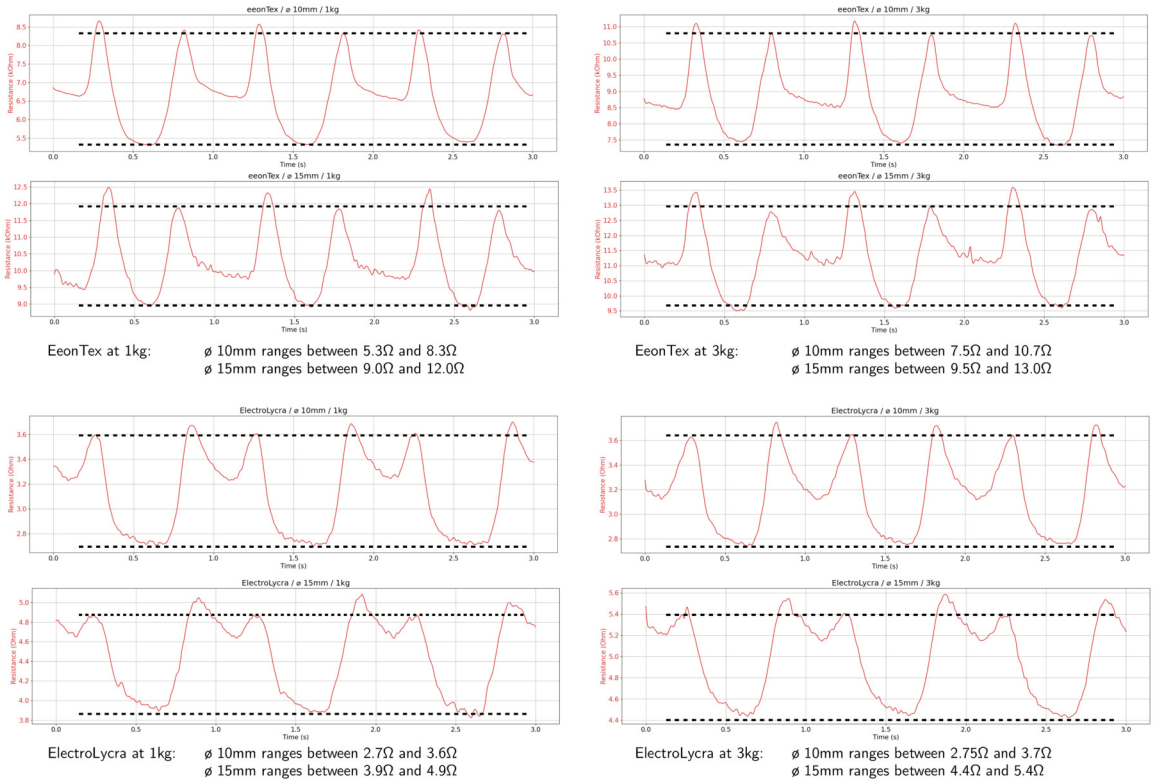

Figure 4.12: This figure shows the absolute resistance values during the dynamic tests. It can be noted that there is a consistent pattern of how resistance values change between tests. Firstly, the resistance increases for the thicker actuators due the greater length of fabric necessary to wrap around the actuator. Secondly, the range of resistance shifts when the system is exposed to an increased load.

suspected to be caused by the material being permanently stretched within the first 1000 cycles. Being elongated could cause the sensor to lose tension and therefore lead to a situation like over-stretching. Other than a re-calibration of the sensor, a possible mitigation approach is pre-stretching the material before using it to assemble the sensor.

4.5.4 Repeatability of Feedback

In Figure 4.15, we illustrate the repeatability of our design's feedback between 1000 and 5000 cycles. In these cycles, the sensors were inflated and deflated over a period of three seconds. This evaluation shows that both fabrics' responses do not deviate to a great degree within this usage window. The *ElectroLycra* sensor shows a greater standard deviation than that of the *EeonTex LTT-SLPA-20K*

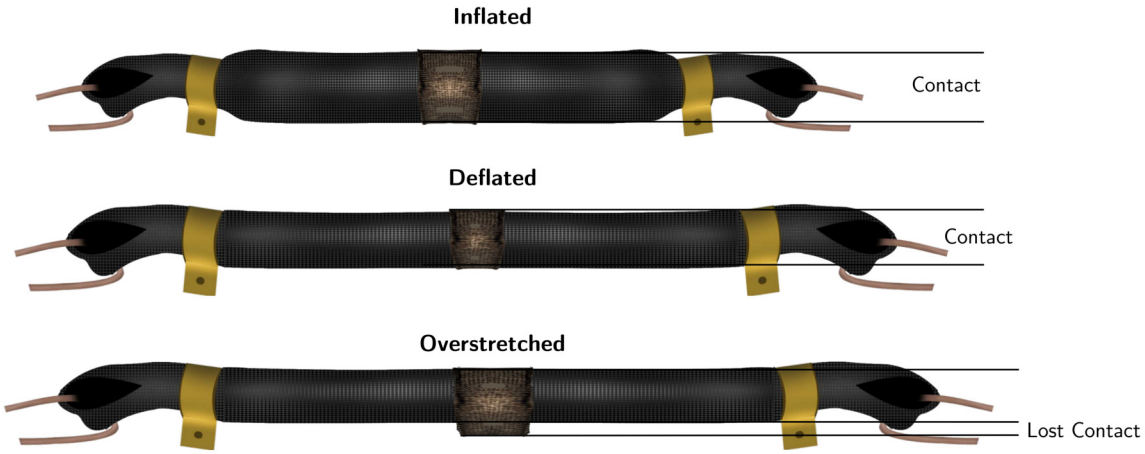

Figure 4.13: This figure illustrates the phenomenon of overstretching as it happens during the dynamic experiments. Due to a tensile force, the actuator gets stretched and, therefore, reduces its circumference to the extent that the sensor is unable to compensate for this deformation. In this situation, the sensor loses close contact with the actuator and produces non-monotonic feedback.

sensor, most notably during deflation.

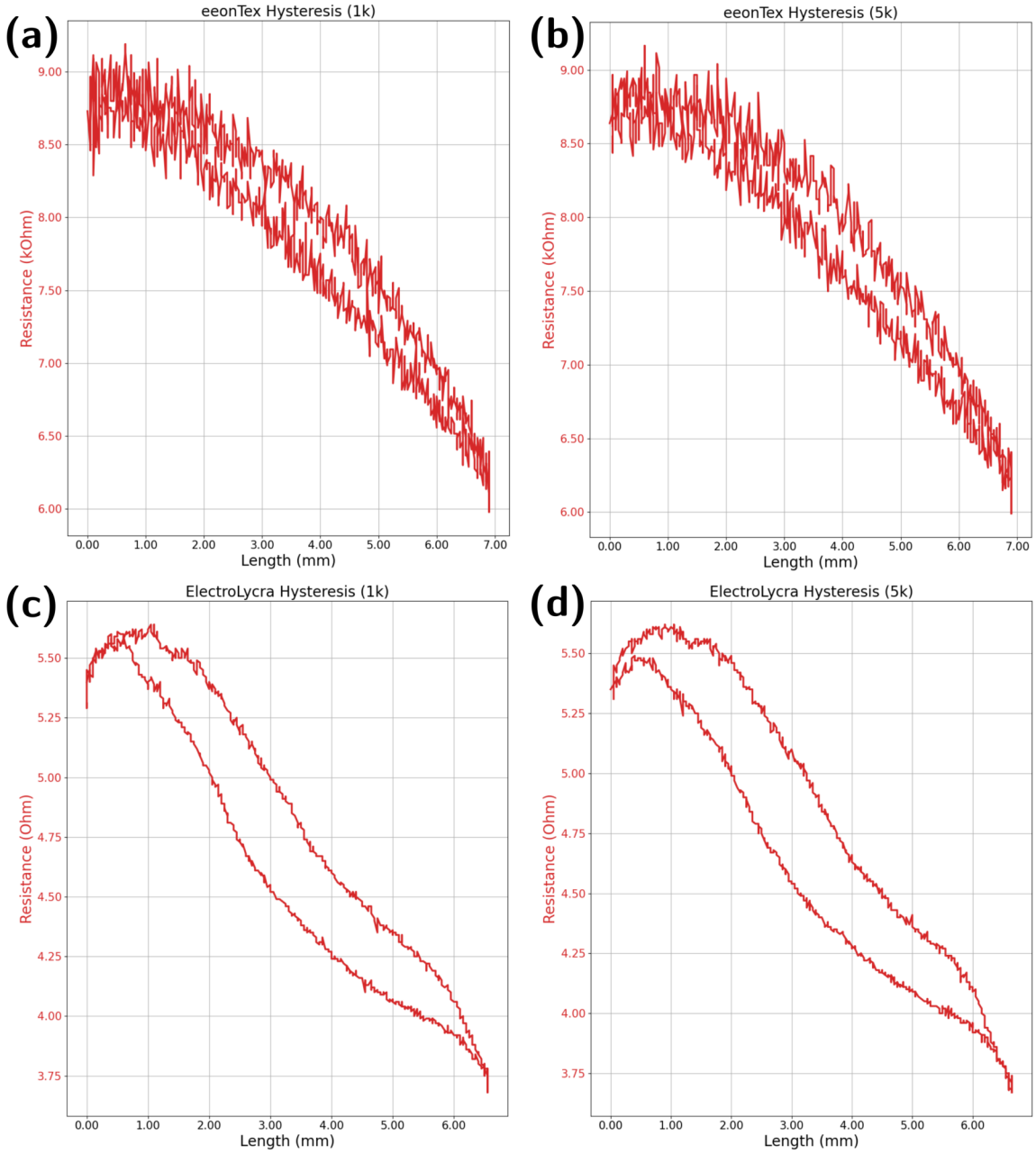

Figure 4.14: This illustration shows the hysteresis plots of sensors made from *EeonTex LTT-SLPA-20K* and *ElectroLycra* after 1000 and 5000 inflations. It can be noted that the shape and range of both hysteresis do not change considerably.

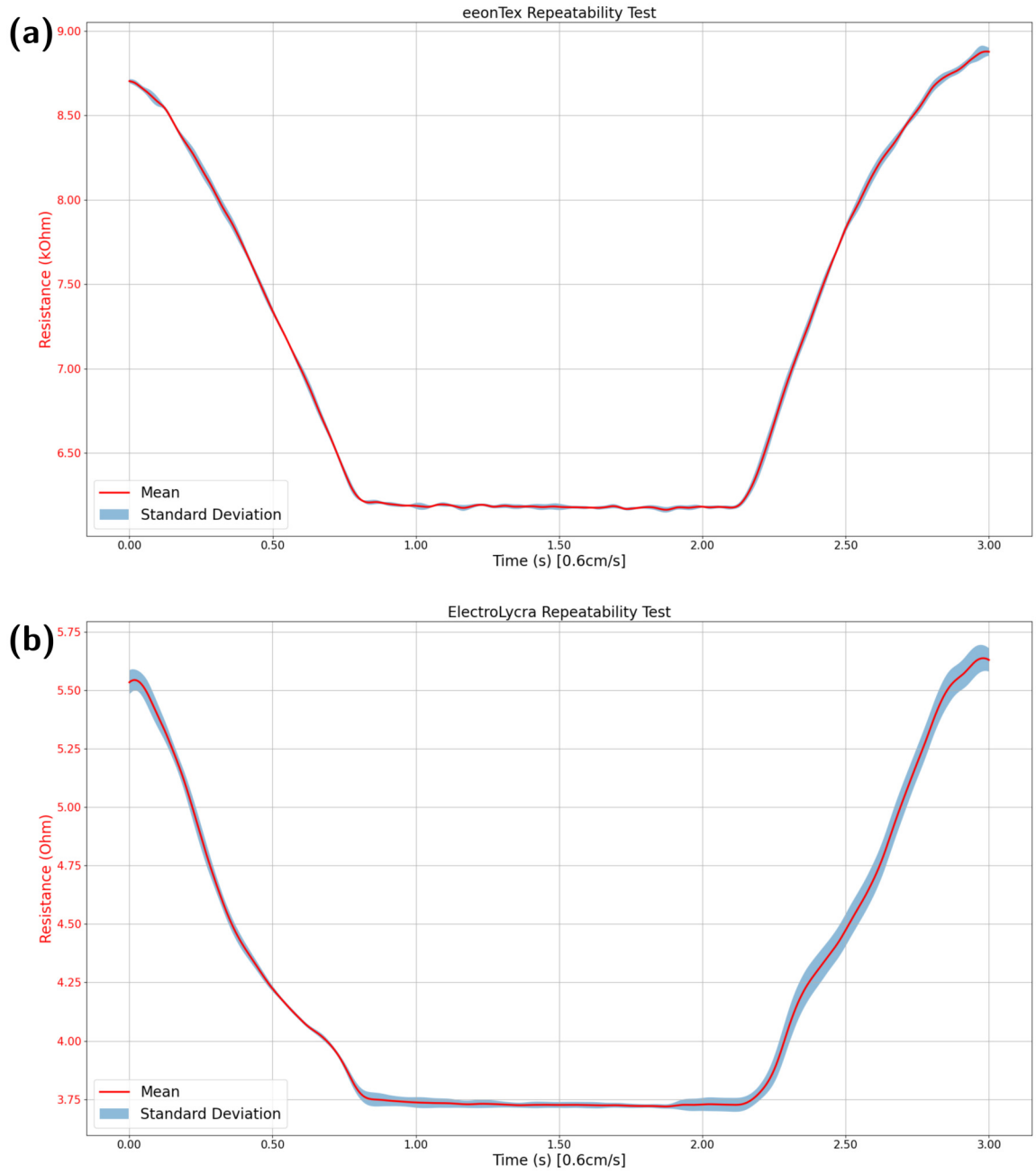

Figure 4.15: This illustration shows the sensors' feedback which were made from *EeonTex LTT-SLPA-20K* and *ElectroLycra* over 5000 inflations. It can be noted that for *EeonTex LTT-SLPA-20K*, the standard deviation is less pronounced than for *ElectroLycra*.

Chapter 5

Collision avoidance via reflex-based control in a musculoskeletal system

5.1 Introduction

Researchers in recent years made efforts to explore and increase the performance of humanoid robots utilizing their shapes to recreate behaviors easily achievable with a human body. It is a common practice to use McKibben pneumatic artificial muscles for musculoskeletal systems as they have comparable characteristics to biological muscles. This approach is expected to allow such robots to potentially solve tasks the same way as humans due to supposably similar motor skills, which could be facilitated to improve walking, running, jumping, grasping, or interacting with obstacles. These assumptions are based on the fact that McKibben pneumatic artificial muscles have several mechanical properties that are found significant to those in the human musculoskeletal system [9]. Therefore, if the human's control could be modeled over their motor skills and adapt such a model to humanoid robots, it should be possible to build a humanoid robot that shows highly improved motor skills comparable to those of humans. During the last decades, several designs of robotic arms were published which focused on showing the advantages of the application of neurobiological knowledge in control approaches for robotic arms. Further, experimentation with different control models derived from nature used with robots could also foster understanding of the human's central nervous system (CNS). Such an increase in understanding could further support the optimization of the control models of robots, as it was demonstrated by the robotic arm system developed by *Blake et al.* for their studies regarding spinal circuits [21]. Also, models based on the cerebellar pathway were used for the control of the movement of arm segments [14, 55]. Simulations were also used to recreate neural control systems to fulfill several tasks [17]. Other contributions like those of *Wu et al.* investigated practical use-cases for a control schema base on the muscle-reflex

mechanism to increase the compliance of a PUMA 560 [68]. However, none of these publications focused on utilizing reflex circuits to increase the capabilities of manipulators when interacting with their environment. Robots require a physical presence to interact with the real world, which is hard to recreate realistically through computer simulations. Further does the shape of a robot greatly influences its effectiveness of interaction with the environment. This needs to be taken into account when an environment manipulating agent is discussed. In humans, the continuous nature of reflex circuits affects voluntary movements and the unconscious processes, which are primarily aimed to protect the body from injury. So, a movement and posture control schema for robotic arms, inspired by the human's CNS, focusing on reflex-based control, was considered to have high merit. When used for a robotic arm, this type of control schema could generate movements and might deal with environmental uncertainties and intentional external disturbance from humans. The experiment in this work will describe the realization of compliant behavior for an antagonistic acting pair of pneumatic artificial muscles generated through continuous feedback from in series tensile force sensors.

5.1.1 Control Approaches

A typical approach to modify behavior is a *Subsumption Architecture*, which inhibits the motion-generating sections of the behavior in the case of a satisfied condition. However, in musculoskeletal systems, the systems are under constant dynamic adjustment based on the muscles' receptors' feedback. So in these low levels of control, no decision-making takes place. The adaptiveness of the system is based only on this continuous feedback loop but is able to generate behavior that subjectively could be perceived as intelligent, conscious behavior. Obviously, such feedback loop-based control would have lower complexity than a decision-based system. Based on this assumption, we investigated the applicability of this system to generate compliant behavior from continuous feedback. This paper will further compare the performance of our feedback-based approach to one that was realized using a subsumption architecture to create compliant and impact mitigating behavior for an oscillating inverted pendulum actuated by pneumatic artificial muscles equipped with tensile force and inflation sensors.

Subsumption Architectures

Subsumption Architectures where before described and used for the realisation of adaptive behaviors by *Brooks* [5], *Connell* [8] and *Ferrell* [16]. These publications used this architecture for mobile robots. However, we believed that this intriguingly intuitive way of creating increasingly complex behaviors would be a prime candidate to control musculoskeletal systems on their lowest level. Due to its low-level nature of intertwined sensory feedback and control signals to the actuator, a subsumption architecture should be viable for a comparison being decision-based while at the same time maintaining relatively low complexity. Our experiment shows that no complex model control schema

is needed where interconnected, parallel executed tasks can achieve such behavior with a low degree of complexity. Contrastingly to more traditional approaches, a subsumption architecture-based control model uses as a stack of incrementally more complex task-achieving behaviors to realize non-trivial behaviors while reducing the duplications of functionalities within its system. Individual implementations of behaviors are called layers. Lower-level behaviors provide the functional foundation for higher layers, which can influence the lower layer's outcome through the subsumption of inputs or the inhibition of outputs within the wiring of the layer's atomic functions. Higher-level layers, therefore, should not recreate functionalities of lower layers but augment their capabilities through subsumption and inhibition. Our middle layer - *Swing Arm* - oscillates the pendulum within its positional limits by feeding our lowest layer with the sole purpose of maintaining an angular position with a given stiffness. So there are multiple paths for a layer's information to flow, contrasting the typical - perception, modeling, action - approach. Therefore, it can be imagined as a concurrent system of behaviors working on the same shared resources utilizing path blocking mechanisms for communication. Each of these paths is concerned only with a small subtask of the system's overall task, such as controlling the actuator's stiffness, the joint's position, and the avoidance of collisions. Each of these layers is except the global in- and output functional independent but can have a path manipulating connection to the lower layer. Therefore each layer constantly produces those motor commands it deems appropriate for a given situation based on its sensor data. A layer is at no point in time unable to perform its task due to the lack of data from higher layers. Thus even if organized in layers of different priority, this architecture is not hierarchical in the typical interpretation. The most distinguishing aspect of the subsumption approach is the realization of direct coupling between sensors and actuators, encouraging the internal processing of each layer to be kept at a minimum. During the design for the subsumption-based control schema for our robot, we first had to decide which behavior is the lowest layer competence of our system. This layer typically represents the most basic skill of a system, which itself is not dependant on the results of higher layers. In our situation, this is the skill *Hold Position (& stiffness)* of our inverted pendulum. This layer only regulates the inflation of the two PAMs so that the position of the joint changes based on the ratio of the inverse divergence of the PAMs' inflation from a given minimal inflation of both actuators, which causes a central position of the joint. The second layer implements the sinusoidal oscillation of the system's arm from one side to another; it thereby uses the first layer and only forwards an updated position to the underlying layer. The highest priority layer is the detection of collisions and, in such a case, inhibiting the information flow from the middle to the lowest layer. The conceptual advantage of subsumption architectures is the individual simplicity of its layers. In Fig. 5.1 we show the overview of our architecture. For our system, we utilize three layers. The highest layer is the collision detection layer. This layer constantly monitors the feedback of the tensile force sensors of each actuator. Once the observed forces diverge from the predicted values, its output will inhibit the underlying layer, interrupting our inverted pendulum's oscillating motion without

asserting any additional force. The mid-layer generates the series of positions used to create the trajectory. Its output feeds into the lowest and behaviorally most trivial layer. The lowest layer's goal is to maintain an arbitrary position and stiffness of the inverted pendulum from its left to its right-most position through input values of -1 to 1.

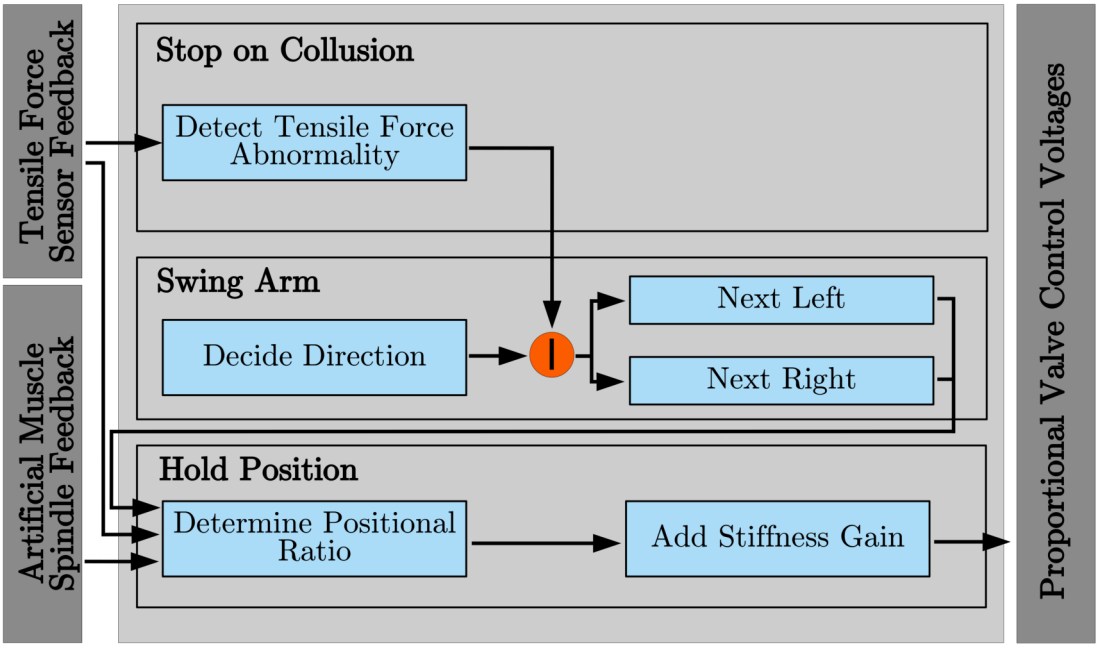

Figure 5.1: This illustration shows the subsumption architecture used during the experiments.

Feedback-based Approach

Our feedback-based approach only utilized mapping and transfer functions, which were fed with the sensor readings of every control cycle. Equation 5.1 shows the both functions used to generate the oscillating pattern of the inverted pendulum by applying 180° phase shifted sinusoidal waveformes.

$$\begin{aligned} pressure_1(t) &= \sin\left(t \bmod 2\pi\right) \\ pressure_2(t) &= -\sin\left(t \bmod 2\pi\right) \end{aligned} \tag{5.1}$$

These functions naturally alternate between -1 to 1, which can be adjusted through Eq. 5.2, so we can use it to generate waveformes oscillating around values that can be directly used as goal

pressure inputs for our control system.

$$\begin{aligned} sine\_transform(value, range_{min}, range_{max}) = \\ \left(\frac{\sqrt{(range_{min} - range_{max})^2}}{2} \times value\right) + \\ \left(\frac{range_{min} + range_{max}}{2}\right) \end{aligned} \tag{5.2}$$

The sample and update rate of our control loop can be chosen. We used a stable update rate of $100HZ$ and a cycle time of $3sec$. Equation 5.3 allows for a dynamic selection and yields the correct iteration size over 2π for a given update rate and cycle length.

$$step\_size = \frac{\frac{2\pi}{update\_rate}}{sec\_per\_cycle} \tag{5.3}$$

Our control is based on the dynamic gain-based adjustment of the iteration size based on the perturbations measured through the tensile force sensors. Equation 5.4 shows how we derive the change rate of the tensile force sensors based on a moving average and the current value. Throughout the systems movement, these values a constantly changing, but during a collusion we can detect a distinct spike in our mapping.

$$\begin{aligned} \Delta ten(t) = tensile\_force\_1_t - tensile\_force\_2_t \\ change\_rate(t) = \\ \begin{cases} \Delta ten(t) - \frac{\sum_{n=0}^{t-1} \Delta ten(n)}{t} & t < ws \\ \Delta ten(t) - \frac{\sum_{n=t-ws}^{t-1} \Delta ten(n)}{ws} & t \geq ws \end{cases} \end{aligned} \tag{5.4}$$

This change rate is then used to dynamically adjust the iteration size based on the change rate and a tuneable gain. The intention is to minimize the iteration size over several measurements based on the change rate, thereby effectively halting the execution of the oscillating motion. This application of the sensor feedback to the pattern generator is formalized in Eq. 5.5.

$$step\_size_{t+1} = \frac{step\_size_t}{1 + (change\_rate \times inhibition\_gain)} \tag{5.5}$$

The movement it based on a time dependant variable t that can be feed into the previous functions. Equation 5.6 describes how a succeeding element is calculated based on the aforementioned iteration size derived from an increasing counter value and mapped to a value range of $0\,to\,2\pi$.

$$t(t+1) = (t + step\_size) \bmod 2\pi \tag{5.6}$$

The whole feedback-based controller is based on these equations. It only utilizes value mappings based on the feedback data and no conventional logic. In the next section, we will show that the performance of this controller is comparable with such generated from a more conventional approach like the subsumption architecture.

Inflation Controller

The lowest layer, however, might have the most trivial behavior. Still, due to its role as the functional base and therefore nearest to the hardware, we illustrated its structure in Fig. 5.2. The block

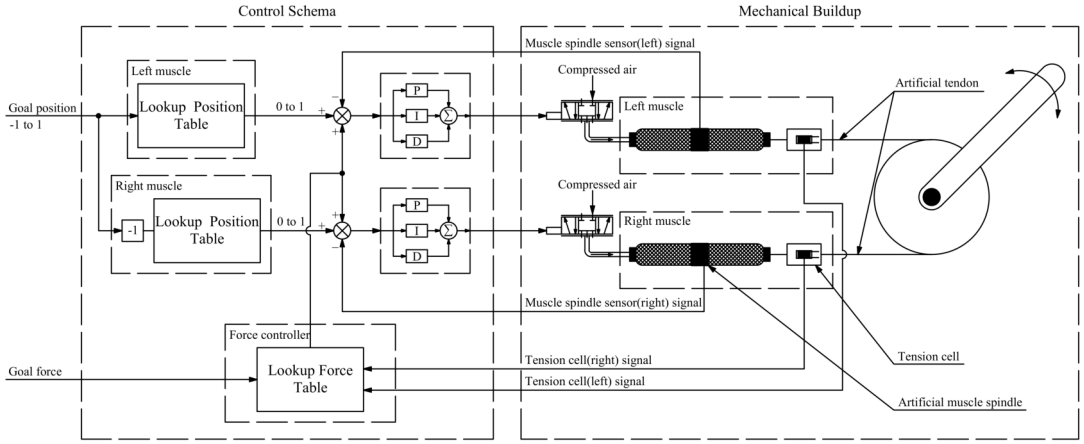

Figure 5.2: This illustration shows the information path in the lowest layer.

accepts two inputs, the already mentioned goal position, and the stiffness or holding force that should be applied to the system. During startup, the system initializes and gathers data points like the individual feedback of the inflation sensors in the actuators' deflated and inflated state and the baseline feedback from the tensile force sensors and their feedback when both actuators are fully inflated and therefore their maximal feedback. Based on this data, the lookup tables are created through linear interpolation. The pendulum's position control is based on the pressure difference of both actuators centered around an idle pressure that holds the pendulum in the middle and introduces a minimal level of antagonistic strain for stable positioning. The maintenance of the individual actuator's inflation is realized via a PID controller. This layer's second input controls the gain on the idle pressure to change the stiffness through uniform additional inflation of both actuators.

5.2 Experimental Setup

Our experimental setup is shown in Fig. 5.3. We use a framework that holds one PAM on each side of an inverted pendulum to create an antagonistic acting muscle pair that actuates one joint and, therefore, changes the pendulum's angle. As this experiment aims to evaluate the control approach, we attempted to increase the repeatability of our system by using linear rails holding the PAMs in place and constraining their movement to their tensile component. Through this, we could eliminate variances in our measurements that would result from the slippage of the actuators. Each actuator

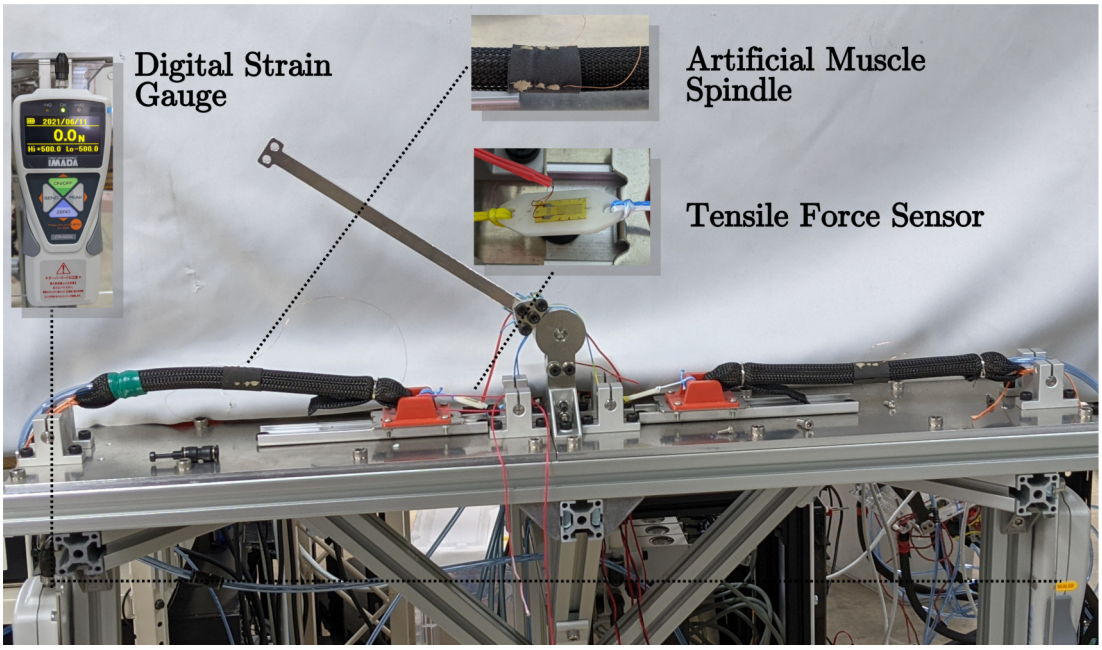

Figure 5.3: This image shows the experimental setup used for the experiments.

is equipped with an inflation sensor made from conductive fabric and custom tensile force sensors in series to the actuator. The fishing lines are used to connect the actuators with the framework. The framework further contains a fixture for a digital strain gauge, which can be positioned within the pendulum's trajectory so the extent of the impact force can be measured.

5.3 Methodology

In this section, the subsumption architecture and our feedback-based approach will be used to realize compliant behaviors in our system. The previously introduced architecture is utilized to generate interconnected two behaviors. The primary directive of the system is the performance of a side-to-side motion. However, an external perturbation should interrupt trajectory execution, which

would be detected via a divergence from the tensile forces expected through the artificial Golgi tendon organs. With our experiment, we will investigate this behavior. During our experiments, an inverted pendulum will move side-to-side controlled by the controller of least priority. In Fig. 5.3 the inverted pendulum used for this experiment is shown. It is actuated by two antagonistically acting pneumatic artificial muscles controlled by the low-level controllers based on a subsumption architecture and reflex-based. Attached to the structure holding the actuators and joints in place is a mount for a digital strain gauge, which can be placed within the trajectory of the oscillating inverted pendulum recreated by our setup. The maximum force was be measured at $\pm 0°$, while the stiffness set to 50% of the individual maximal holding force of an actuator pair. These numbers were derived from the system's work envelope of $+40°$ and $-35°$ based on its maximal range of motion. This discrepancy has to be explained by the variance of handcrafted pneumatic actuators. In such unbalanced situations, the use of inflation sensors combined with tensile force sensors allows actuators of different inherent properties to work in a cooperative setup due to the equalizing effect of their sensory feedback used in our control structure.

5.4 Experimental Results

The results achieved during our experiments allow us to suspect the principal applicability of the control architecture in the form we investigated it. Our testing series resulted in an average impact force when using the subsumption architecture at $3.31N$ at a cycle time of three seconds and an average of $3.48N$ at a five-second cycle time. The standard deviations were found to be 0.36 at a cycle time of three seconds and 0.3 at five seconds. Fig. 5.4 and 5.5 shows those results. The increase in peak impact force during slower oscillations seemed to be counter-intuitive. Still, it can be explained with the function used to detect collision in the subsumption architecture. The detection is based on the same change rate of the tensile force sensors as it is also used by the reflex-based model and shown in Eq. 5.4. The subsumption architecture used this function to change points. These change points are more significant if the rate changes rapidly, e.g., faster oscillations. When moving at a slower rate, the impact is less violent, and therefore, the change rate is less distinct what causes the collision detection to trigger with a slight delay when compared with the response during a faster movement. The results of our reflex-based controller shown in Fig. 5.6 and 5.7 show a comparable response to the collusion. For this controller, the average impact force at a cycle time of three seconds was found to be $4.66N$, and for collisions at a cycle of five seconds $3.68N$. However, the standard deviations were found to be 0.17 for a cycle time of three seconds and 0.23 for a cycle time of five seconds and are therefore noticeable lower than those produced via the controller based on a subsumption architecture. Nevertheless, the obvious assumption that a reflex-based controller might cause higher peak impact forces at higher movement speeds than the binary logic-based subsumption architecture could also be initially confirmed through our experiments. However, it is worth noticing

that the reflex-based controller produces lower impact forces in slower movements.

5.5 Conclusion

This paper investigated the practicability of a control schema base on a constant feedback loop compared to a controller based on a subsumption architecture to realize collision avoidance for a pair of antagonistic pneumatic artificial muscles. Based on the experiments presented in this paper, it could be inferred that such practicability is factual. We could show that our control schema allows for the emergence of stable compliant behavior purely by the inhibition based on feedback adopting the system's movement constantly. Due to the individual nature of hand-made pneumatic artificial muscles, every estimation of variance will inevitably contain this error of the actuators themselves. However, the lack of a clear trend in combination with a clear cluster suggests that our proposed control schema can compensate for these factors. An interesting insight of this experiment is that it shows the advantage of the sensory abundance of a musculoskeletal joint over a servo motor. The servo can precisely measure the current rotation of its shaft as well as inferring the effort for its movement based on the amperage. The musculoskeletal joint actuated by antagonistic muscles freely moved with a fixed stiffness can detect perturbation simply by comparing the tensile forces of the involved actuators. It isn't said that with the current mechanical possibilities that the musculoskeletal systems have a clear advantage over traditional actuators like servo motors, but their specific morphology allows for interesting low-complexity control schema, which possibly in the future could give these systems an operative edge over conventional actuators.

Future Work

Our results showed that in a single-joint antagonistic muscle setup, a controller utilizing a reflex-based model is a viable solution to implement the low-level behavior of such a muscle pair that can be performance-wise compared with well-known approaches like the subsumption architecture. The next step would be the transfer of these results to systems with a higher degree of freedom. We expect that following the idea of layered behaviors of increasing complexity through the utilization of the underlying behaviors, the extension of our controller should be transferable to such systems. In particular, it would be valuable to investigate maximal complexity through the number of layers in the field of manipulation. Considering the increase in complexity in relation to degrees of freedom, it could be beneficial to have individual controllers for individual joints or groups of PAMs being integrated into a controller which plans more complex tasks.

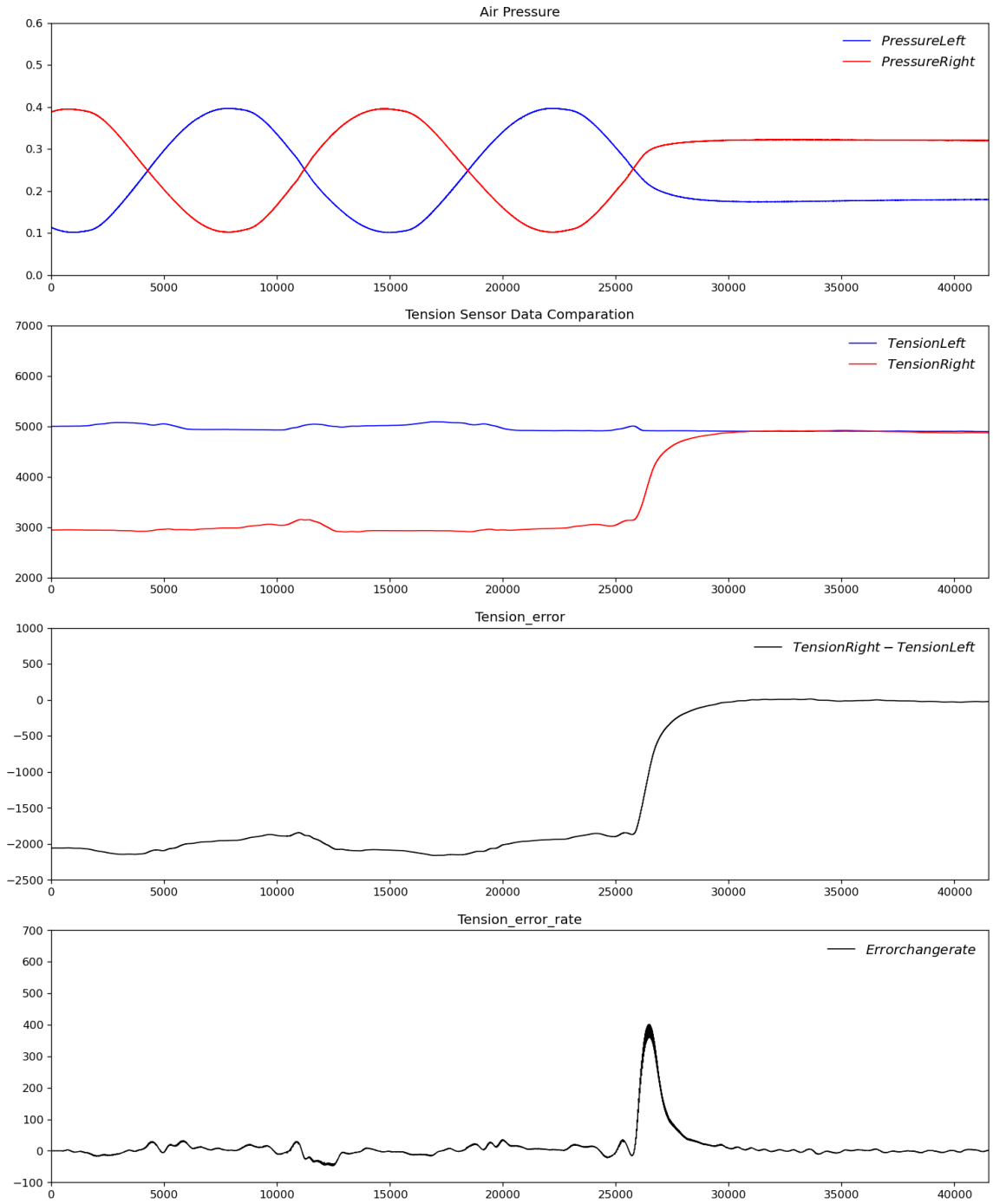

Figure 5.4: The graphs above show the response of the system using the subsumption architecture during collisions.

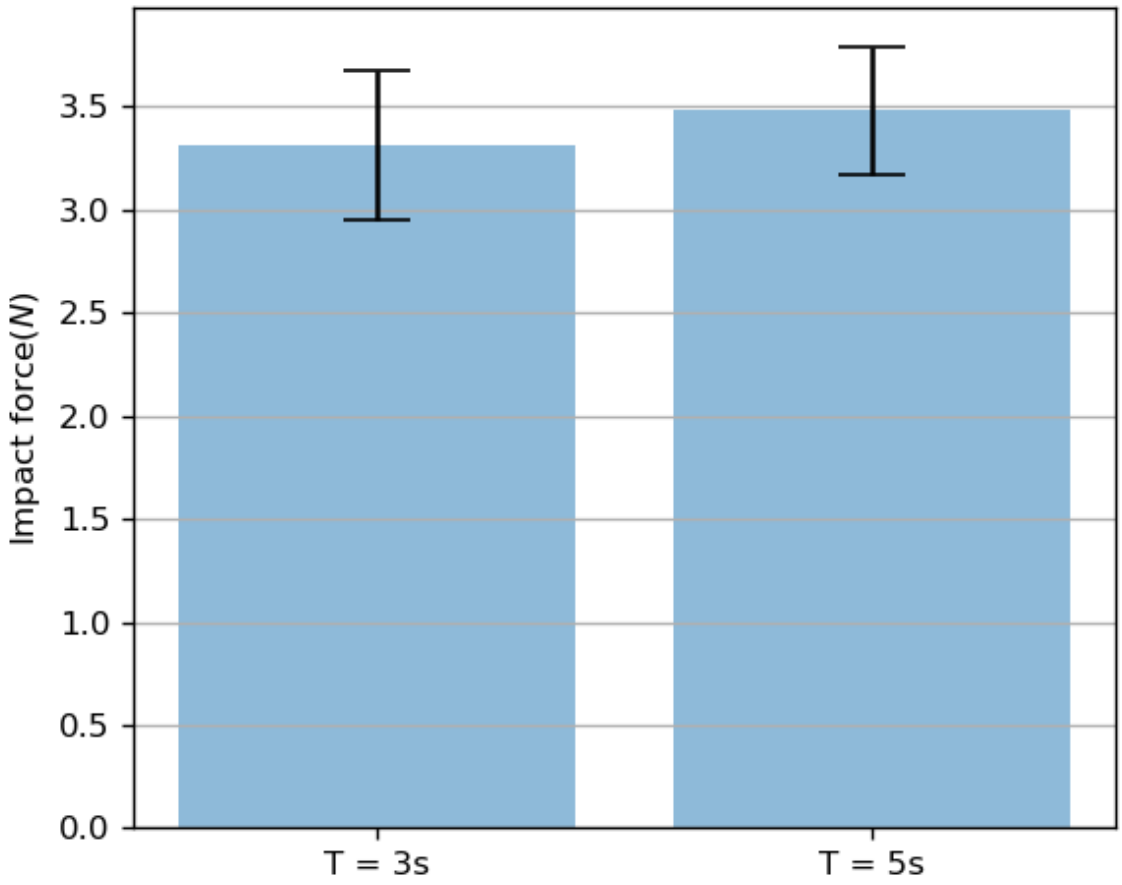

Figure 5.5: This illustration shows the peak impact force using a subsumption architecture at cycle times of three and five seconds.

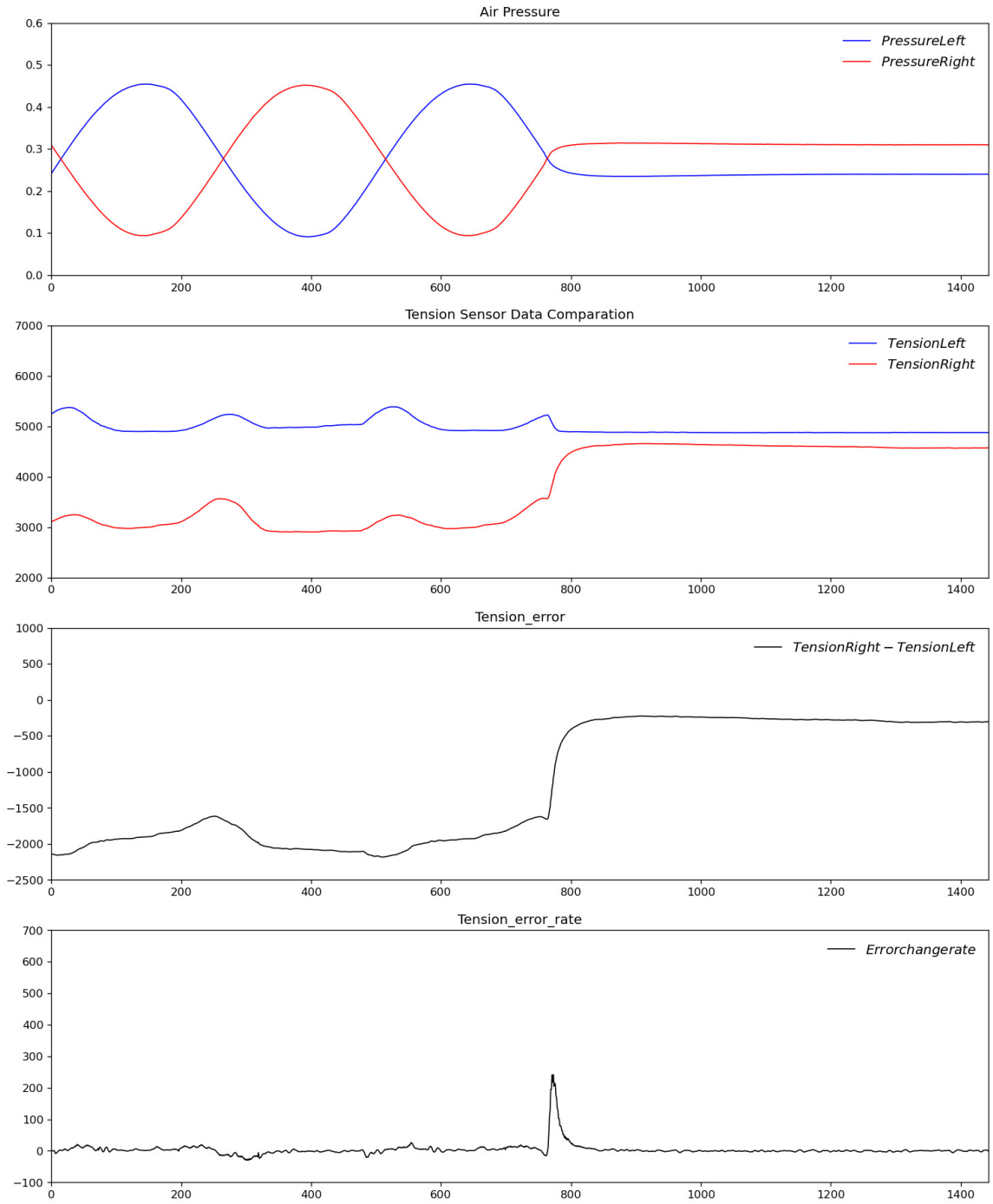

Figure 5.6: The graphs above show the response of the system using our reflex-based model during collisions.

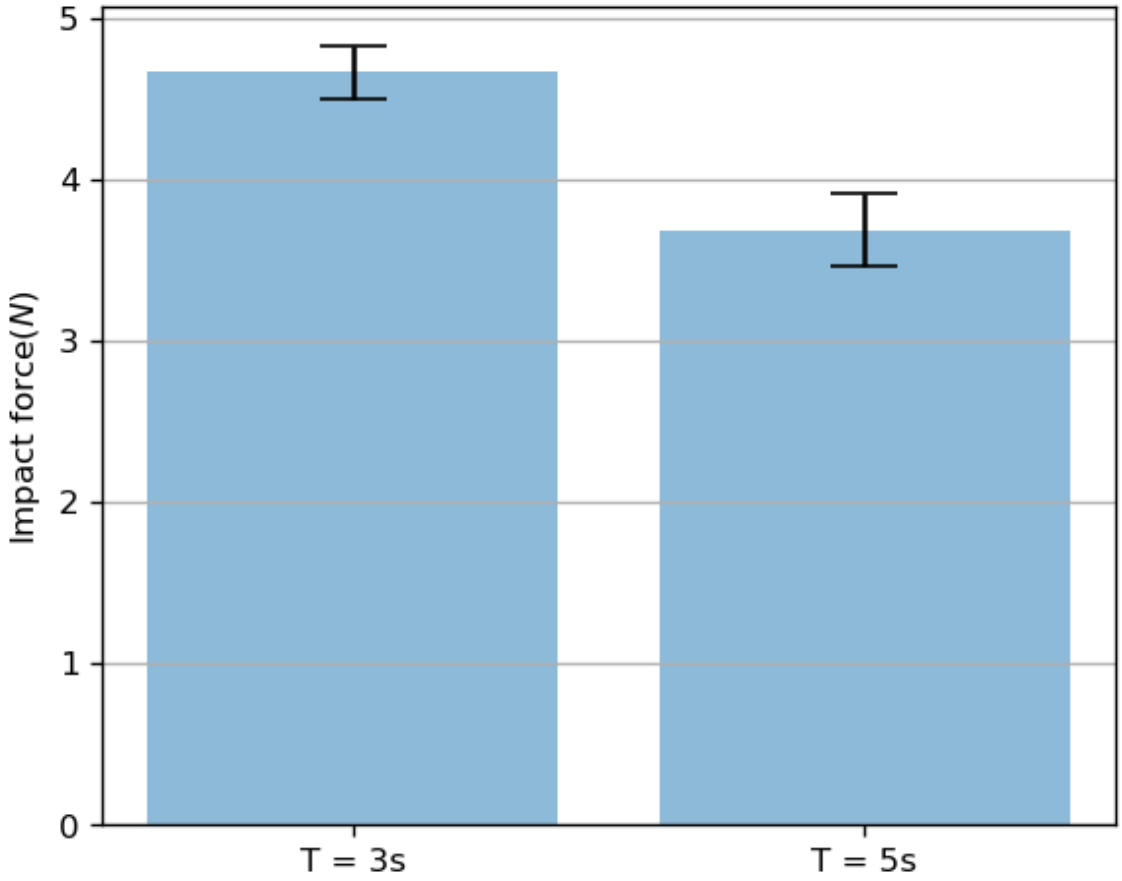

Figure 5.7: This illustration shows the peak impact force using our reflex-based model at cycle times of three and five seconds.

Chapter 6

Conclusion

This study focused on the development of a humanoid musculoskeletal robot to investigate control methods for the realization of reflex-based control. Chapter 2 presented our design for a humanoid upper body structure which morphology is closely oriented on the human upper body's musculoskeletal system. The skeleton was closely recreated with each joint, and a complex sliding and ball joint structure was used for the shoulder. This system's capabilities to replay trajectories in a repeatable manner were evaluated. We also showed that the inherent compliance of the structure allowed the operation of a crank using only key poses and exploiting the external constraints of the crank to allow for reliable rotations. This system was also used for extermination on several learning-based methods to create motor skills with this robot. Using a Kinect v2 *Campell et al.* [6] implemented an interactive handshaking behavior derived from the observation of handshaking approaches to the robot made by multiple subjects. *Liu et al.* [38] implemented a motor babbling approach for our system to generate an inverse kinematics model. Based on these results, we concluded that the system's lack of sensory feedback of the actuators limits its potential as it does not allow for the compensation of external perturbations. In the following, we focused on the creation of adequate sensory feedback for pneumatic artificial muscles, besides the tensile force sensors designed after the functional principle of the Golgi Tendon Organ. In biological muscles, its contraction is detected by the muscle spindles, which are also responsible for providing the motor units with feedback so that antagonistic muscles can be controlled effectively. We, therefore, investigated multiple designs, which would make the functional principle of muscle spindles available for our control method. In chapter 3, we proposed our first design for an artificial muscle spindle with the goal to embed it seamlessly into the actuator. We also followed the biological design by embedding two individual sensors into one actuator. Through our experiments, we could show that this design was capable of providing the expected feedback about the actuator's inflation. However, this design tended to fatigue breakages of the probe wires caused by the shearing forces it exposed to between the actuator's inner rubber tube and outer braided sleeve. We, therefore, improved our design in this aspect and

proposed our new design in chapter 4. The new design comprised only one stretch-sensitive sensor, which is wrapped around the actuator. This design had a highly improved longevity and made the production of the sensors themselves easier and allowed for the swapping between actuators in the case of a malfunction and the deployment to existing actuators. Chapter 4 described the characteristics of sensors made from conductive fabrics in great detail and proved through the conducted experiments that this design is a capable novel approach for generating inflation feedback from pneumatic artificial muscles. In chapter 5, we proposed a control method using the bio-inspired sensors we created in our earlier research. This research focused on the creation of reflex-like behaviors as they are found in biological muscles, where motor units control the contraction of antagonistic muscle pairs. We could show that no complex control strategy is necessary to achieve such behavior. Through the continuous feedback into multiple parallel low complexity behaviors, we could realize compliant behavior, where the system would interrupt its movement when an external perturbation is detected.

6.1 Future Work

Manipulation results from the intricate cooperation of the nervous system, the musculoskeletal system, and the environment. In our studies, we investigated how the control complexity for musculoskeletal systems can be reduced through the usage of bio-inspired feedback. Thus, the results showed that through the proper selection - based on what is found in nature - of feedback, the control complexity of musculoskeletal systems can be drastically reduced. As the work presented in this thesis investigated the feasibility of our control approach, more experiments on more complex systems need to be conducted in the future. A first step would be the deployment of our sensory system presented in chapters 3 and 4 to a robot with more degrees of freedom so that gravity can have a more significant effect on motor skills. A potential system would be made of three hinge joints, so while being exposed to the influence of gravity, the system is still constraint into a two-dimensional plane. With this system, the creation of models for inverse kinematics could be investigated to evaluate the influence of our control scheme's compliance to the system's capability of reaching a goal pose. This system can also further be used to evaluate the resilience to external perturbations and the stability of the goal reaching when payloads are attached to the robot's end-effector. The next stage would be deploying these sensors to a complex musculoskeletal robot like the upper body robot presented in chapter 2. This system would introduce interacting muscle groups of more than two individual actuators. The behavior of our control approach presented in chapter 5 and its potential to reduce the complexity to realize motor skills in such a system should be investigated. Especially how our control architecture scales with the complexity of a manipulator when used for its low-level control would need further research. Besides the domain of manipulators, our approach could also be investigated for musculoskeletal systems used for locomotion. As these systems naturally depend

on fast reactions to environmental changes, it could be assumed that a reflex-based control schema like ours could be beneficial for such systems. However, the results of our experiments do not provide a clear indication of the potential due to the vastly different nature of these behaviors. During locomotion, the lower extremities are under constant strain and, to some degree, act as a spring; that is why models like the SLIP model can be used to control locomotion.

Acknowledgements

This work was conducted under the supervision of Professor Koh Hosoda (Department of Systems Innovation, Graduate School of Engineering Science, Osaka University). I would like to express sincere gratitude to him for our numerous discussions, his suggestions, and continued encouragement. Further, I would like to express my deep gratitude to the former Assistant Professor and now Principal Investigator at the Kyushu Institute of Technology Dr. Shuhei Ikemoto for all of his support, ideas, guidance, and his constant willingness to engage in fruitful discussions. I also want to thank the Assistant Professors Takumi Kawasetsu and Shunsuke Shigaki for their helpful feedback and support of my work. This work would not have been possible without all the professional and personal resources they provided me with to allow for my constant academic improvement. I would also like to give my special thanks to Mr. Tsung-Yuan Chen, Dr. Hirofumi Shin, Dr. Liu Xiangxiao, Mr. Hiroaki Masuda, Ms. Yanlin Wang, Mr. Tyler Kessler, my family, and all the other students, staff members, and friends for their support of my studies and personal life.

Bibliography

[1] Festo AG. Airic's arm – robot arm with fluidic muscles, 2007.

[2] Tetsuya Akagi, Shujiro Dohta, Yuji Kenmotsu, Feifei Zhao, and Masataka Yoneda. Development of smart inner diameter sensor for position control of mckibben artificial muscle. *Procedia Engineering*, 41:105–112, 2012.

[3] Yuki Asano, Toyotaka Kozuki, Soichi Ookubo, Masaya Kawamura, Shinsuke Nakashima, Takeshi Katayama, Iori Yanokura, Toshinori Hirose, Kento Kawaharazuka, Shogo Makino, et al. Human mimetic musculoskeletal humanoid kengoro toward real world physically interactive actions. In *Humanoid Robots (Humanoids), 2016 IEEE-RAS 16th International Conference on*, pages 876–883. IEEE, 2016.

[4] Shantonu Biswas and Yon Visell. Emerging material technologies for haptics. *Advanced Materials Technologies*, 4(4):1900042, 2019.

[5] Rodney Brooks. A robust layered control system for a mobile robot. *IEEE journal on robotics and automation*, 2(1):14–23, 1986.

[6] Joseph Campbell, Arne Hitzmann, Simon Stepputtis, Shuhei Ikemoto, Koh Hosoda, and Heni Ben Amor. Learning interactive behaviors for musculoskeletal robots using bayesian interaction primitives. *arXiv preprint arXiv:1908.05552*, 2019.

[7] C. P. Chou and B. Hannaford. Static and dynamic characteristics of mckibben pneumatic artificial muscles. In *Proceedings of the 1994 IEEE International Conference on Robotics and Automation*, pages 281–286 vol.1, May 1994.

[8] Jonathan H Connell. *Minimalist mobile robotics*, volume 5. Elsevier, 2012.

[9] F. Daerden and D. Lefeber. Pneumatic artificial muscles: actuators for robotics and automation. *European journal of mechanical and environmental engineering*, 47(1):11–21, 2002.

[10] Frank Daerden and Dirk Lefeber. Pneumatic artificial muscles: actuators for robotics and automation. *European journal of mechanical and environmental engineering*, 47(1):11–21, 2002.

[11] Keith Davids, Chris Button, and Simon Bennett. *Dynamics of skill acquisition: A constraints-led approach.* Human Kinetics, 2008.

[12] Onder Erin, Nishant Pol, Luis Valle, and Yong-Lae Park. Design of a bio-inspired pneumatic artificial muscle with self-contained sensing. In *2016 38th Annual International Conference of the IEEE Engineering in Medicine and Biology Society (EMBC)*, pages 2115–2119. IEEE, 2016.

[13] Onder Erin, Nishant Pol, Luis Valle, and Yong-Lae Park. Design of a bio-inspired pneumatic artificial muscle with self-contained sensing. In *2016 38th Annual International Conference of the IEEE Engineering in Medicine and Biology Society (EMBC)*, pages 2115–2119. IEEE, 2016.

[14] Selim Eskiizmirliler, N Forestier, Bertrand Tondu, and Christian Darlot. A model of the cerebellar pathways applied to the control of a single-joint robot arm actuated by mckibben artificial muscles. *Biological cybernetics*, 86(5):379–394, 2002.

[15] Wyatt Felt, Khai Yi Chin, and C David Remy. Contraction sensing with smart braid mckibben muscles. *IEEE/ASME Transactions on Mechatronics*, 21(3):1201–1209, 2015.

[16] Cynthia Ferrell. Robust and adaptive locomotion of an autonomous hexapod. In *Proceedings of PerAc'94. From Perception to Action*, pages 66–77. IEEE, 1994.

[17] Michele Folgheraiter, Giuseppina C Gini, and Massimo Cavallari. A neural-control system for a humanoid artificial arm. In *ICINCO-ICSO*, pages 119–126, 2007.

[18] NC Goulbourne, S Son, and JW Fox. Self-sensing mckibben actuators using dielectric elastomer sensors. In *Electroactive Polymer Actuators and Devices (EAPAD) 2007*, volume 6524, page 652414. International Society for Optics and Photonics, 2007.

[19] Iku Hamamoto, Tetsuya Akagi, Shujiro Dohta, and Hisashi Matsushita. Development of a flexible displacement sensor using nylon string coated with carbon and its application for mckibben actuator. In *2006 SICE-ICASE International Joint Conference*, pages 1943–1946. IEEE, 2006.

[20] Blake Hannaford, Jack M Winters, Ching-Ping Chou, and Pierre-Henry Marbot. The anthroform biorobotic arm: a system for the study of spinal circuits. *Annals of biomedical engineering*, 23(4):399–408, 1995.

[21] Blake Hannaford, Jack M Winters, Ching-Ping Chou, and Pierre-Henry Marbot. The anthroform biorobotic arm: a system for the study of spinal circuits. *Annals of biomedical engineering*, 23(4):399–408, 1995.

[22] Shinichi Hirai et al. Measuring mckibben actuator shrinkage using fiber sensor. In *2015 24th IEEE International Symposium on Robot and Human Interactive Communication (RO-MAN)*, pages 628–633. IEEE, 2015.

[23] Arne Hitzmann, Shuhei Ikemoto, and Koh Hosoda. Highly-integrated muscle-spindles for pneumatic artificial muscles made from conductive fabrics. In Uriel Martinez-Hernandez, Vasiliki Vouloutsi, Anna Mura, Michael Mangan, Minoru Asada, Tony J. Prescott, and Paul F.M.J. Verschure, editors, *Biomimetic and Biohybrid Systems*, pages 171–182, Cham, 2019. Springer International Publishing.

[24] Arne Hitzmann, Hiroaki Masuda, Shuhei Ikemoto, and Koh Hosoda. Anthropomorphic musculoskeletal 10 degrees-of-freedom robot arm driven by pneumatic artificial muscles. *Advanced Robotics*, 32(15):865–878, 2018.

[25] K. Hosoda, H. Saito, and S. Ikemoto. Muscular-skeletal humanoid robot for body image construction. In *2016 International Symposium on Micro-NanoMechatronics and Human Science (MHS)*, pages 1–3, Nov 2016.

[26] S. Ikemoto, Y. Kimoto, and K. Hosoda. Shoulder complex linkage mechanism for humanlike musculoskeletal robot arms. *Bioinspiration & Biomimetics*, 10(6):066009, 2015.

[27] Shuhei Ikemoto, Fumiya Kannou, and Koh Hosoda. Humanlike shoulder complex for musculoskeletal robot arms. In *Intelligent Robots and Systems (IROS), 2012 IEEE/RSJ International Conference on*, pages 4892–4897. IEEE, 2012.

[28] Masayuki Inaba, Ikuo Mizuuchi, Ryosuke Tajima, Tomoaki Yoshikai, Daisuke Sato, Koichi Nagashima, and Hirochika Inoue. Building spined muscle-tendon humanoid. *Robotics Research*, pages 113–127, 2003.

[29] Kristen N Jaax and Blake Hannaford. A biorobotic structural model of the mammalian muscle spindle primary afferent response. *Annals of Biomedical Engineering*, 30(1):84–96, 2002.

[30] Michael Jäntsch, Steffen Wittmeier, Konstantinos Dalamagkidis, Guido Herrmann, and Alois Knoll. Adaptive neural network dynamic surface control: An evaluation on the musculoskeletal robot anthrob. In *Robotics and Automation (ICRA), 2015 IEEE International Conference on*, pages 4347–4352. IEEE, 2015.

[31] Michael Jäntsch, Steffen Wittmeier, Konstantinos Dalamagkidis, Alexander Panos, Fabian Volkart, and Alois Knoll. Anthrob-a printed anthropomimetic robot. In *Humanoid Robots (Humanoids), 2013 13th IEEE-RAS International Conference on*, pages 342–347. IEEE, 2013.

[32] Kento Kawaharazuka, Shogo Makino, Masaya Kawamura, Yuki Asano, Kei Okada, and Masayuki Inaba. Online learning of joint-muscle mapping using vision in tendon-driven musculoskeletal humanoids. *IEEE Robotics and Automation Letters*, 2018.

[33] Masaya Kawamura, Soichi Ookubo, Yuki Asano, Toyotaka Kozuki, Kei Okada, and Masayuki Inaba. A joint-space controller based on redundant muscle tension for multiple dof joints in musculoskeletal humanoids. In *Humanoid Robots (Humanoids), 2016 IEEE-RAS 16th International Conference on*, pages 814–819. IEEE, 2016.

[34] Sangbae Kim, Cecilia Laschi, and Barry Trimmer. Soft robotics: a bioinspired evolution in robotics. *Trends in biotechnology*, 31(5):287–294, 2013.

[35] Shinji Kuriyama, Ming Ding, Yuichiro Kurita, Tsukasa Ogasawara, and Jun Ueda. Flexible sensor for mckibben pneumatic actuator. In *SENSORS, 2009 IEEE*, pages 520–525. IEEE, 2009.

[36] Shunichi Kurumaya, Koichi Suzumori, Hiroyuki Nabae, and Shuichi Wakimoto. Musculoskeletal lower-limb robot driven by multifilament muscles. *Robomech Journal*, 3(1):18, 2016.

[37] Li Li, Song Liu, Feng Ding, Tao Hua, Wai Man Au, and Kwok-Shing Wong. Electromechanical analysis of length-related resistance and contact resistance of conductive knitted fabrics. *Textile research journal*, 82(20):2062–2070, 2012.

[38] Zinan Liu, Arne Hitzmann, Shuhei Ikemoto, Svenja Stark, Jan Peters, and Koh Hosoda. Local online motor babbling: Learning motor abundance of a musculoskeletal robot arm. *arXiv preprint arXiv:1906.09013*, 2019.

[39] S. Mack, E.R. Kandel, T.M. Jessell, J.H. Schwartz, S.A. Siegelbaum, and A.J. Hudspeth. *Principles of Neural Science*. Principles of Neural Science. McGraw-Hill Education, 2013.

[40] Hugo Gravato Marques, Michael Jäntsch, Steffen Wittmeier, Owen Holland, Cristiano Alessandro, Alan Diamond, Max Lungarella, and Rob Knight. Ecce1: The first of a series of anthropomimetic musculoskeletal upper torsos. In *Humanoid Robots (Humanoids), 2010 10th IEEE-RAS International Conference on*, pages 391–396. IEEE, 2010.

[41] Predrag Milosavljevic, Nenad Bascarevic, Kosta Jovanovic, and Goran Kvascev. Neural networks in feedforward control of a robot arm driven by antagonistically coupled drives. In *Neural Network Applications in Electrical Engineering (NEUREL), 2012 11th Symposium on*, pages 77–80. IEEE, 2012.

[42] Ikuo Mizuuchi, Yuto Nakanishi, Yoshinao Sodeyama, Yuta Namiki, Tamaki Nishino, Naoya Muramatsu, Junichi Urata, Kazuo Hongo, Tomoaki Yoshikai, and Masayuki Inaba. An advanced musculoskeletal humanoid kojiro. In *Humanoid Robots, 2007 7th IEEE-RAS International Conference on*, pages 294–299. IEEE, 2007.

[43] Ikuo Mizuuchi, Tomoaki Yoshikai, Yoshinao Sodeyama, Yuto Nakanishi, Akihiko Miyadera, Taichi Yamamoto, Tuomas Niemela, Marika Hayashi, Junichi Urata, Yuta Namiki, et al. Development of musculoskeletal humanoid kotaro. In *Robotics and Automation, 2006. ICRA 2006. Proceedings 2006 IEEE International Conference on*, pages 82–87. IEEE, 2006.

[44] Hiroyuki Nakamoto, Soushi Oida, Hideo Ootaka, Mitsunori Tada, Ichiro Hirata, Futoshi Kobayashi, and Fumio Kojima. Application of stretchable strain sensor for pneumatic artificial muscle. In *2014 IEEE Symposium on Robotic Intelligence in Informationally Structured Space (RiiSS)*, pages 1–5. IEEE, 2014.

[45] Yuto Nakanishi, Yuki Asano, Toyotaka Kozuki, Hironori Mizoguchi, Yotaro Motegi, Masahiko Osada, Takuma Shirai, Junichi Urata, Kei Okada, and Masayuki Inaba. Design concept of detail musculoskeletal humanoid kenshiro-toward a real human body musculoskeletal simulator. In *Humanoid Robots (Humanoids), 2012 12th IEEE-RAS International Conference on*, pages 1–6. IEEE, 2012.

[46] Yuto Nakanishi, Tamon Izawa, Masahiko Osada, Nobuyuki Ito, Shigeki Ohta, Junichi Urata, and Masayuki Inaba. Development of musculoskeletal humanoid kenzoh with mechanical compliance changeable tendons by nonlinear spring unit. In *Robotics and Biomimetics (ROBIO), 2011 IEEE International Conference on*, pages 2384–2389. IEEE, 2011.

[47] Kenichi Narioka and Koh Hosoda. Designing synergistic walking of a whole-body humanoid driven by pneumatic artificial muscles: An empirical study. *Advanced Robotics*, 22(10):1107–1123, 2008.

[48] Kenichi Narioka, Shinpei Tsugawa, and Koh Hosoda. 3d limit cycle walking of musculoskeletal humanoid robot with flat feet. In *Intelligent Robots and Systems, 2009. IROS 2009. IEEE/RSJ International Conference on*, pages 4676–4681. IEEE, 2009.

[49] Ryuma Niiyama, Kei Kakitani, and Yasuo Kuniyoshi. Learning to jump with a musculoskeletal robot using a sparse coding of activation. In *Proc. ICRA 2009 Workshop on Approaches to Sensorimotor Learning on Humanoid Robots*, pages 30–31, 2009.

[50] Ryuma Niiyama and Yasuo Kuniyoshi. Design principle based on maximum output force profile for a musculoskeletal robot. *Industrial Robot: An International Journal*, 37(3):250–255, 2010.

[51] Ryuma Niiyama, Satoshi Nishikawa, and Yasuo Kuniyoshi. Athlete robot with applied human muscle activation patterns for bipedal running. In *Humanoid Robots (Humanoids), 2010 10th IEEE-RAS International Conference on*, pages 498–503. IEEE, 2010.

[52] Shimon Y Nof. *Handbook of industrial robotics*. John Wiley & Sons, 1999.

[53] Yuya Okadome, Yutaka Nakamura, Kenji Urai, Yoshihiro Nakata, and Hiroshi Ishiguro. Huma: A human-like musculoskeletal robot platform for physical interaction studies. In *Humanoid Robots (Humanoids), 2015 IEEE-RAS 15th International Conference on*, pages 676–683. IEEE, 2015.

[54] Soichi Ookubo, Yuki Asano, Toyotaka Kozuki, Takuma Shirai, Kei Okada, and Masayuki Inaba. Learning nonlinear muscle-joint state mapping toward geometric model-free tendon driven musculoskeletal robots. In *Humanoid Robots (Humanoids), 2015 IEEE-RAS 15th International Conference on*, pages 765–770. IEEE, 2015.

[55] Sofiane Ouanezar, Frédéric Jean, Bertrand Tondu, Marc A Maier, Christian Darlot, and Selim Eskiizmirliler. Biologically inspired sensory motor control of a 2-link robotic arm actuated by mckibben muscles. In *2011 IEEE International Conference on Robotics and Automation*, pages 2785–2791. IEEE, 2011.

[56] Gianluca Palli, Umberto Scarcia, Claudio Melchiorri, and Gabriele Vassura. Development of robotic hands: The ub hand evolution. In *2012 IEEE/RSJ international conference on intelligent robots and systems*, pages 5456–5457. IEEE, 2012.

[57] Y. Park and R. J. Wood. Smart pneumatic artificial muscle actuator with embedded microfluidic sensing. In *SENSORS, 2013 IEEE*, pages 1–4, Nov 2013.

[58] Cheng Peng, Yue H Yin, Hai B Hong, Jian J Zhang, and Xing Chen. Bio-inspired design methodology of sensor-actuator-structure integrated system for artificial muscle using sma. *Procedia CIRP*, 65:299–303, 2017.

[59] Veljko Potkonjak, Kosta M Jovanovic, Predrag Milosavljevic, Nenad Bascarevic, and Owen Holland. The puller-follower control concept in the multi-jointed robot body with antagonistically coupled compliant drives. In *IASTED international conference on robotics*, pages 375–381, 2011.

[60] Arthur Prochazka and Peter Ellaway. Sensory systems in the control of movement. *Comprehensive Physiology*, 2012.

[61] Uwe Proske. The golgi tendon organ. *Trends in Neurosciences*, 2(Supplement C):7 – 8, 1979.

[62] Dale Purves. *Neuroscience*. Sinauer Associates Publishers, 2011.

[63] Ryo Sakurai, Mitsuhiro Nishida, Hideyuki Sakurai, Yasumichi Wakao, Nozomi Akashi, Yasuo Kuniyoshi, Yuna Minami, and Kohei Nakajima. Emulating a sensor using soft material dynamics: A reservoir computing approach to pneumatic artificial muscle. In *2020 3rd IEEE International Conference on Soft Robotics (RoboSoft)*, pages 710–717. IEEE, 2020.

[64] Bertrand Tondu, Serge Ippolito, Jérémie Guiochet, and Alain Daidie. A seven-degrees-of-freedom robot-arm driven by pneumatic artificial muscles for humanoid robots. *The International Journal of Robotics Research*, 24(4):257–274, 2005.

[65] A. R. Tsouroukdissian. ros_control: An overview. *ROSCon*, 2014.

[66] S. Wakimoto, K. Suzumori, and T. Kanda. Development of intelligent mckibben actuator with built-in soft conductive rubber sensor. In *The 13th International Conference on Solid-State Sensors, Actuators and Microsystems, 2005. Digest of Technical Papers. TRANSDUCERS '05.*, volume 1, pages 745–748, June 2005.

[67] Steffen Wittmeier, Michael Jäntsch, Konstantinos Dalamagkidis, and Alois Knoll. Physics-based modeling of an anthropomimetic robot. In *Intelligent Robots and Systems (IROS), 2011 IEEE/RSJ International Conference on*, pages 4148–4153. IEEE, 2011.

[68] Chi-haur Wu, Kao-Shing Hwang, and Shih-Lang Chang. Analysis and implementation of a neuromuscular-like control for robotic compliance. *IEEE Transactions on control systems technology*, 5(6):586–597, 1997.

[69] Xiaofeng Xiong, Florentin Wörgötter, and Poramate Manoonpong. Virtual agonist-antagonist mechanisms produce biological muscle-like functions: an application for robot joint control. *Industrial Robot: An International Journal*, 41(4):340–346, 2014.

[70] Takuya Yano, Shinsaku Fujimoto, Tetsuya Akagi, and Wataru Kobayashi. Development of outer diameter sensor for position control of mckibben artificial actuator using hall-effect sensor. *International Journal of Mechanical Engineering and Robotics Research*, 9(2), 2020.

[71] Koichiro Yokoyama and Kiminao Kogiso. Pid position control of mckibben pneumatic artificial muscle using only pressure feedback. In *2018 Annual American Control Conference (ACC)*, pages 3362–3367. IEEE, 2018.

[72] Michelle C. Yuen, Rebecca Kramer-Bottiglio, and Jamie Paik. Strain sensor-embedded soft pneumatic actuators for extension and bending feedback. In *2018 IEEE International Conference on Soft Robotics (RoboSoft)*, pages 202–207. IEEE, 2018.

Publications

Journal Papers

(1) Hitzmann, A., Masuda, H., Ikemoto, S. and Hosoda, K., 2018. Anthropomorphic musculoskeletal 10 degrees-of-freedom robot arm driven by pneumatic artificial muscles. Advanced Robotics, 32(15), pp.865-878.

(2) *Liu, X., Duan, Y., Hitzmann, A., Xu, Y., Chen, T., Ikemoto, S. and Hosoda, K., 2018. Using the foot windlass mechanism for jumping higher: a study on bipedal robot jumping. Robotics and Autonomous Systems, 110, pp.85-91.

(3) Hitzmann, A., Wang, Y., Kessler, T. and Hosoda, K., 2021. Using conductive fabrics as inflation sensors for pneumatic artificial muscles. Advanced Robotics, pp.1-17.

(4) Hitzmann, A, Wang, Y, Hosoda, K. Collision avoidance via reflex-based control in a musculoskeletal system. IEEE Robotics and Automation Letters. [submitted July 2021]

* This work does not have strong relations to the scope of this dissertation.

International Conference Papers

(1) Hitzmann, A., Ikemoto, S. and Hosoda, K., 2018, December. Towards the Exploitation of External Constraints with Robots Actuated by Pneumatic Artificial Muscles. In 2018 International Symposium on Micro-NanoMechatronics and Human Science (MHS) (pp. 1-4). IEEE.

(2) Hitzmann, A., Ikemoto, S. and Hosoda, K., 2019, July. Highly-Integrated Muscle-Spindles for Pneumatic Artificial Muscles Made from Conductive Fabrics. In Conference on Biomimetic and Biohybrid Systems (pp. 171-182). Springer, Cham.

(3) Campbell, J., Hitzmann, A., Stepputtis, S., Ikemoto, S., Hosoda, K. and Amor, H.B., 2019, November. Learning interactive behaviors for musculoskeletal robots using bayesian interaction primitives. In 2019 IEEE/RSJ International Conference on Intelligent Robots and Systems (IROS) (pp. 5071-5078). IEEE.

(4) Masuda, H., Hitzmann, A., Hosoda, K. and Ikemoto, S., 2019, November. Common Dimensional Autoencoder for Learning Redundant Muscle-Posture Mappings of Complex Musculoskeletal Robots. In 2019 IEEE/RSJ International Conference on Intelligent Robots and Systems (IROS) (pp. 2545-2550). IEEE.

(5) Liu, Z., Hitzmann, A., Ikemoto, S., Stark, S., Peters, J. and Hosoda, K., 2019, November. Local Online Motor Babbling: Learning Motor Abundance of a Musculoskeletal Robot Arm. In 2019 IEEE/RSJ International Conference on Intelligent Robots and Systems (IROS) (pp. 6594-6601). IEEE.